

1989

Gravitational and coupling effects in modeling of an elastic robot arm

Alan Matthew Hufnagel
Iowa State University

Follow this and additional works at: <https://lib.dr.iastate.edu/rtd>

 Part of the [Mechanical Engineering Commons](#)

Recommended Citation

Hufnagel, Alan Matthew, "Gravitational and coupling effects in modeling of an elastic robot arm " (1989). *Retrospective Theses and Dissertations*. 9196.
<https://lib.dr.iastate.edu/rtd/9196>

This Dissertation is brought to you for free and open access by the Iowa State University Capstones, Theses and Dissertations at Iowa State University Digital Repository. It has been accepted for inclusion in Retrospective Theses and Dissertations by an authorized administrator of Iowa State University Digital Repository. For more information, please contact digirep@iastate.edu.

INFORMATION TO USERS

The most advanced technology has been used to photograph and reproduce this manuscript from the microfilm master. UMI films the text directly from the original or copy submitted. Thus, some thesis and dissertation copies are in typewriter face, while others may be from any type of computer printer.

The quality of this reproduction is dependent upon the quality of the copy submitted. Broken or indistinct print, colored or poor quality illustrations and photographs, print bleedthrough, substandard margins, and improper alignment can adversely affect reproduction.

In the unlikely event that the author did not send UMI a complete manuscript and there are missing pages, these will be noted. Also, if unauthorized copyright material had to be removed, a note will indicate the deletion.

Oversize materials (e.g., maps, drawings, charts) are reproduced by sectioning the original, beginning at the upper left-hand corner and continuing from left to right in equal sections with small overlaps. Each original is also photographed in one exposure and is included in reduced form at the back of the book. These are also available as one exposure on a standard 35mm slide or as a 17" x 23" black and white photographic print for an additional charge.

Photographs included in the original manuscript have been reproduced xerographically in this copy. Higher quality 6" x 9" black and white photographic prints are available for any photographs or illustrations appearing in this copy for an additional charge. Contact UMI directly to order.

U·M·I

University Microfilms International
A Bell & Howell Information Company
300 North Zeeb Road, Ann Arbor, MI 48106-1346 USA
313/761-4700 800/521-0600

Order Number 8920141

**Gravitational and coupling effects in modeling of an elastic
robot arm**

Hufnagel, Alan Matthew, Ph.D.

Iowa State University, 1989

U·M·I
300 N. Zeeb Rd.
Ann Arbor, MI 48106

**Gravitational and coupling effects in modeling of an
elastic robot arm**

by

Alan Matthew Hufnagel

**A Dissertation Submitted to the
Graduate Faculty in Partial Fulfillment of the
Requirements for the Degree of
DOCTOR OF PHILOSOPHY**

Major: Mechanical Engineering

Approved:

Signature was redacted for privacy.

In Charge of Major Work

Signature was redacted for privacy.

For the Major Department

Signature was redacted for privacy.

For the Graduate College

**Iowa State University
Ames, Iowa
1989**

TABLE OF CONTENTS

ACKNOWLEDGEMENTS		xiii
DESCRIPTION OF NOMENCLATURE		xiv
LIST OF NOMENCLATURE		xv
1 INTRODUCTION		1
2 LITERATURE REVIEW		3
2.1 Modeling Techniques		3
2.1.1 Finite Element Method		4
2.1.2 Assumed Modes Method		6
2.2 Solution Techniques		9
2.2.1 Eigenanalysis		9
2.2.2 Numerical Integration		11
2.3 Experimental Studies		12
2.4 Elastic Arm Literature		14
3 ANALYTICAL MODEL OF AN ELASTIC ARM		17
3.1 Derivation of Exact Model		18
3.2 Derivation of Assumed Modes Model		27

3.2.1	Selection of Assumed Mode Shapes	31
3.3	Derivation of Rigid Model	33
4	COMPARISON OF MODELS	35
4.1	Experimental Apparatus and Procedure	35
4.2	Effect of Mode Shape Selection	39
4.2.1	Development of Alternative Assumed Mode Shapes	39
4.2.2	Results	43
4.3	Coupling of Elastic and Gross Motion	48
4.4	Effect of Gravity	51
4.4.1	Correction Term for Gravity	54
4.4.2	Effect of Gravity on Mode Shape Selection	62
4.5	Conclusions	65
5	EFFECT OF END MASS	68
5.1	Derivation of Exact Model	68
5.2	Derivation of Assumed Modes Model	75
5.3	Derivation of Rigid Model	78
5.4	Effect of Mode Shape Selection	79
5.4.1	Development of Alternative Assumed Mode Shapes	79
5.4.2	Results	83
5.5	Coupling of Elastic and Gross Motion	89
5.6	Effect of Gravity	93
5.6.1	Effect of Gravity on Mode Shape Selection	101
5.7	Conclusions	106

6	CONCLUSIONS	108
7	BIBLIOGRAPHY	110
8	APPENDIX A. EXPERIMENTAL PROCEDURE	115
	8.1 Measurement of Torsional Spring Constant	115
	8.2 Natural Frequency Measurement	117
9	APPENDIX B. COMPARISON POLYNOMIAL DEVELOPMENT	120
	9.1 Elastic Arm Without End Mass	120
	9.2 Elastic Arm With End Mass	121
10	APPENDIX C. CANTILEVER MODE SHAPE DEVELOPMENT	124
	10.1 Cantilever Beam	124
	10.2 Cantilever-Mass Loaded Beam	124

LIST OF TABLES

Table 4.1:	Case 1 parameters	43
Table 4.2:	Case 2 parameters	49
Table 4.3:	Case 3 parameters	50
Table 4.4:	Errors in first natural frequency of exact and coupled can- tilever models in presence of gravity; case 1	52
Table 4.5:	Effect of gravity on first natural frequency of cantilever beam	60
Table 4.6:	Effect of gravity on second natural frequency of cantilever beam	60
Table 5.1:	End mass parameters	83
Table 5.2:	Effect of gravity on experimentally measured first natural frequency of cantilever-mass loaded beam; $(m_a/m) = 1.0$.	94
Table 5.3:	Effect of gravity on experimentally measured second natural frequency of cantilever-mass loaded beam; $(m_a/m) = 1.0$.	97

LIST OF FIGURES

Figure 3.1:	Elastic arm system	19
Figure 3.2:	Free body diagram of rigid arm	34
Figure 4.1:	Experimental elastic arm apparatus	36
Figure 4.2:	Displacement measurement system	38
Figure 4.3:	Schematic of instrumentation	38
Figure 4.4:	Comparison of first natural frequencies from alternative assumed mode shapes; horizontal orientation; case 1	44
Figure 4.5:	Comparison of second natural frequencies from alternative assumed mode shapes; horizontal orientation; case 1	45
Figure 4.6:	Effective mode shape for first element of eigenvector	46
Figure 4.7:	Comparison of linear combinations of assumed mode shapes to first exact mode shape; horizontal orientation; $K_t = 200$ in-lb-rad ⁻¹ ; case 1	47
Figure 4.8:	Comparison of linear combinations of assumed mode shapes to second exact mode shape; horizontal orientation; $K_t = 200$ in-lb-rad ⁻¹ ; case 1	47

Figure 4.9: Comparison of first natural frequencies of coupled and uncoupled models; horizontal orientation; case 1	49
Figure 4.10: Frequency shift from rigid model as function of (f_r/f_c) . . .	50
Figure 4.11: First natural frequency of coupled models in presence of gravity; case 1	52
Figure 4.12: Second natural frequency of coupled model in presence of gravity; case 1	53
Figure 4.13: First natural frequency of the exact model in presence of gravity; case 2 (3/4 x 1/16 x 30 inch steel beam); case 3 (3/4 x 1/16 x 20 inch aluminum beam)	54
Figure 4.14: Cantilever beam model	55
Figure 4.15: Comparison of exact and approximate vertical displacements, $v_{\max} = 0.01$	57
Figure 4.16: Change in first natural frequency of cantilever beam due to gravity	60
Figure 4.17: First natural frequency of revised assumed modes model in presence of gravity; case 1	63
Figure 4.18: Second natural frequency of revised assumed modes model in presence of gravity; case 1	63
Figure 4.19: Comparison of first natural frequencies from alternative assumed mode shapes; vertical orientation; revised model; case 1	64

Figure 4.20: Comparison of second natural frequencies from alternative assumed mode shapes; vertical orientation; revised model; case 1	65
Figure 4.21: Comparison of linear combinations of assumed mode shapes to first exact mode shape; vertical orientation; $K_t = 200$ in-lb-rad ⁻¹ ; revised model; case 1	66
Figure 4.22: Comparison of linear combinations of assumed mode shapes to second exact mode shape; vertical orientation; $K_t = 200$ in-lb-rad ⁻¹ ; revised model; case 1	66
Figure 5.1: Elastic arm with end mass	69
Figure 5.2: Free body diagram of rigid arm	79
Figure 5.3: Comparison of first natural frequencies from alternative assumed mode shapes; horizontal orientation; case 1; $(m_a/m) = 0.25$	84
Figure 5.4: Comparison of first natural frequencies from alternative assumed mode shapes; horizontal orientation; case 1; $(m_a/m) = 1.0$	85
Figure 5.5: Comparison of linear combinations of assumed mode shapes to first exact mode shape; $K_t = 200$ in-lb-rad ⁻¹ ; horizontal orientation; case 1; $(m_a/m) = 0.25$	85
Figure 5.6: Comparison of linear combinations of assumed mode shapes to first exact mode shape; $K_t = 200$ in-lb-rad ⁻¹ ; horizontal orientation; case 1; $(m_a/m) = 1.0$	86

Figure 5.7:	Comparison of second natural frequencies from alternative assumed mode shapes; horizontal orientation; case 1; $(m_a/m) = 0.25$	87
Figure 5.8:	Comparison of second natural frequencies from alternative assumed mode shapes; horizontal orientation; case 1; $(m_a/m) = 1.0$	87
Figure 5.9:	Comparison of linear combinations of assumed mode shapes to second exact mode shape; $K_t = 200$ in-lb-rad ⁻¹ ; horizontal orientation; case 1; $(m_a/m) = 0.25$	88
Figure 5.10:	Comparison of linear combinations of assumed mode shapes to second exact mode shape; $K_t = 200$ in-lb-rad ⁻¹ ; horizontal orientation; case 1; $(m_a/m) = 1.0$	88
Figure 5.11:	Comparison of first natural frequencies of coupled and uncoupled models; horizontal orientation; case 1; $(m_a/m) = 0.25$	90
Figure 5.12:	Comparison of first natural frequencies of coupled and uncoupled models; horizontal orientation; case 1; $(m_a/m) = 1.0$	91
Figure 5.13:	Frequency shift from rigid model as function of (f_r/f_{cm})	91
Figure 5.14:	Error in rigid model as function of (f_r/f_c)	93
Figure 5.15:	First natural frequency of coupled models in presence of gravity; case 1; $(m_a/m) = 0.25$	94

Figure 5.16: First natural frequency of coupled models in presence of gravity; case 1; $(m_a/m) = 1.0$	95
Figure 5.17: Second natural frequency of coupled models in presence of gravity; case 1; $(m_a/m) = 0.25$	96
Figure 5.18: Second natural frequency of coupled models in presence of gravity; case 1; $(m_a/m) = 1.0$	96
Figure 5.19: Second natural frequency of coupled cantilever-mass loaded model; comparison of gravity correction; case 1; $(m_a/m) = 0.25$	99
Figure 5.20: Second natural frequency of coupled cantilever-mass loaded model; comparison of gravity correction; case 1; $(m_a/m) = 1.0$	99
Figure 5.21: First natural frequency of coupled cantilever-mass loaded model; comparison of gravity correction; case 1; $(m_a/m) = 0.25$	100
Figure 5.22: First natural frequency of coupled cantilever-mass loaded model; comparison of gravity correction; case 1; $(m_a/m) = 1.0$	100
Figure 5.23: Comparison of first natural frequencies from alternative assumed mode shapes; vertical orientation; case 1; $(m_a/m) = 0.25$	101

Figure 5.24: Comparison of first natural frequencies from alternative assumed mode shapes; vertical orientation; case 1; $(m_a/m) = 1.0$	102
Figure 5.25: Comparison of linear combinations of assumed mode shapes to first exact mode shape; $K_t = 200$ in-lb-rad ⁻¹ ; vertical orientation; case 1; $(m_a/m) = 0.25$	103
Figure 5.26: Comparison of linear combinations of assumed mode shapes to first exact mode shape; $K_t = 200$ in-lb-rad ⁻¹ ; vertical orientation; case 1; $(m_a/m) = 1.0$	103
Figure 5.27: Comparison of second natural frequencies from alternative assumed mode shapes; vertical orientation; case 1; $(m_a/m) = 0.25$	104
Figure 5.28: Comparison of second natural frequencies from alternative assumed mode shapes; vertical orientation; case 1; $(m_a/m) = 1.0$	105
Figure 5.29: Comparison of linear combinations of assumed mode shapes to second exact mode shape; $K_t = 200$ in-lb-rad ⁻¹ ; vertical orientation; case 1; $(m_a/m) = 0.25$	105
Figure 5.30: Comparison of linear combinations of assumed mode shapes to second exact mode shape; $K_t = 200$ in-lb-rad ⁻¹ ; vertical orientation; case 1; $(m_a/m) = 1.0$	106
Figure 8.1: Free body diagram of arm	116

Figure 8.2: Calibration graph for K_t 117

Figure 8.3: Typical displacement autospectrum 118

ACKNOWLEDGEMENTS

I would like to express my gratitude to Marty Vanderploeg, both advisor and friend, for his support and encouragement in my Ph.D. program. I am also grateful to Professors Bernard, Skaar, McConnell, and Huston for their input while serving on my doctoral committee. I am especially grateful to Dr. McConnell, who graciously allowed the use of the Vibrations Laboratory for my research and who was always generous with his wisdom and insight.

In addition, I would like to thank my colleagues in 0095E, Alan Lynch, Jeff Trom, Jay Shannan, and Chaeyoun Oh for their encouragement during my Ph.D. program.

Finally, I would like to thank my family for their love and support.

DESCRIPTION OF NOMENCLATURE

The mathematical symbols used in this thesis are either scalars, vectors, or matrices. Symbols without an arrow or tilde, such as D , are scalars. Those with an arrow over the symbol, such as \vec{D} , are vectors; while matrices are denoted by a tilde over the symbol, as in \tilde{D} . Transposes of vectors and matrices are denoted by a superscript "T", as in \vec{D}^T . Differentiation with respect to time is denoted by one or more dots, as in \ddot{D} ; while derivatives with respect to the space variable x are denoted by $'$, as in D' .

LIST OF NOMENCLATURE

A	cross sectional area of arm
B_{ij}	coefficient in characteristic equation
C_j	jth constant for exact mode shape
\bar{C}	damping matrix
c_i	ith polynomial coefficient
$D_i(t)$	ith deformation coordinate
\bar{D}	deformation coordinate vector
d_i	ith polynomial coefficient
E	modulus of elasticity
e_i	ith polynomial coefficient
\bar{F}	forcing function vector
f_c	first natural frequency of cantilever beam
f_{cm}	first natural frequency of cantilever-mass loaded beam
f_i	ith natural frequency
f_r	natural frequency of rigid model
g	gravitational acceleration
g_i	ith polynomial coefficient
h	vertical displacement of arm due to transverse deflection

I	moment of inertia of arm cross section
J_a	mass moment of inertia of end mass
J_l	mass moment of inertia of rigid hub
K_t	stiffness of torsional spring
\tilde{K}	stiffness matrix
l	length of arm
M	bending moment in beam
\tilde{M}	mass matrix
m	mass of arm
m_a	mass of end mass
n	number of assumed mode shapes
\tilde{P}	nonlinear term vector
\tilde{Q}	generalized force vector
\tilde{q}	generalized coordinate vector
\tilde{r}	position vector to point on arm
T	kinetic energy
t	time
u_{ji}	jth element of ith eigenvector
$v(x, t)$	elastic deformation of arm
W_{nc}	nonconservative work
$X_i(x)$	ith coupled mode shape
x	distance along axis of arm
$Y(x)$	space solution to boundary value problem

y	vertical location of point on arm, in $\bar{I}\bar{J}\bar{K}$ system
α	frequency parameter in boundary value problem
β	parameter for clamped-mass loaded beam
$\bar{\Gamma}$	assumed mode shape vector
$\tilde{\Gamma}$	modal matrix
$\gamma(x, t)$	elastic rotation of arm
δ	variational operator
ϵ	angle due to vertical displacement effect
η	parameter for clamped-mass loaded beam
θ	gross rotation coordinate of arm
$\bar{\mu}(x, t)$	angular velocity of arm
Π	potential energy
ρ	mass density
$\tilde{\Upsilon}$	modal matrix
$\Psi_i(x)$	i th assumed mode shape
$\bar{\Psi}$	vector of assumed mode shapes
$\tilde{\Psi}$	modal matrix
$\bar{\Omega}$	modal matrix
ω	circular natural frequency

1 INTRODUCTION

Traditional techniques for analysis and synthesis of mechanisms rely on the assumption that the links of the mechanism can be modeled as rigid bodies. Although all structural members display some elastic behavior, for many years the elastic displacements of a typical mechanism were so small that the rigid body assumption was valid. Even today, most mechanisms can be accurately modeled with rigid links. However, there is a new class of mechanisms which have significant elastic displacements.

Robots are one class of mechanisms in which elastic effects can be important. Robots require accurate, repeatable position control. Conventional robot control systems cannot provide this accuracy when the links are significantly elastic. Therefore, conventional robots achieve this accuracy by being extremely rigid. However, the material needed to insure their rigidity also makes them quite massive, and thus slow. Many researchers believe that a properly controlled elastic robot could be as accurate as a rigid robot and would be much lighter, faster, and less expensive than conventional designs. Because of these advantages, control of elastic robots is an active research area and has an extensive body of literature.

Many papers have studied the control problem of a single planar elastic robot arm. While these papers have presented a variety of control algorithms, few have

addressed the question of how to best model an elastic arm. As a result, there are few guidelines for developing an accurate dynamic model of an elastic robot arm. For example, the assumed modes method is commonly used to model elastic arms. However, few papers have studied the effect of assumed mode shape selection upon the accuracy of the model. In addition, few researchers have investigated the effect of a mass at the tip of the arm. However, robots typically carry a manipulator and payload at the tip of the arm. The goal of this thesis is to develop modeling guidelines for a planar elastic robot arm with an end mass. This thesis will address the selection of assumed mode shapes, coupling of elastic and rigid motion, and the effect of gravity upon the model.

This thesis develops both an assumed modes model and an exact model of an elastic robot arm to investigate these modeling questions. These models are used to study the effects of gravity, mode shape selection, coupling of elastic and rigid motions, and end mass. In addition, the validity of these models is determined by comparison of their natural frequencies to the frequencies of an experimentally tested elastic robot arm.

The next chapter of this thesis reviews the elastic mechanism literature. Chapter 3 presents models of an elastic robot arm without an end mass. Chapter 4 discusses the experimental verification of these models and addresses the effect of mode shape selection, elastic coupling, and gravity upon the elastic arm model. Chapter 5 then extends this work to an elastic arm with an end mass. Conclusions are presented in Chapter 6.

2 LITERATURE REVIEW

Four literature reviews have been published in the area of elastic mechanism analysis. In 1972, Erdman and Sandor [1] published the first literature review in this area. In the same year, Lowen and Jandrasits [2] published a review of the literature concerning mechanisms with distributed mass and elasticity. Their paper contained an extensive review of the earliest work, European literature from 1933 to the 1960s. Lowen and Chassapis's [3] paper presented an extensive review of the elastic mechanism literature from 1977 to 1983. In 1986, Thompson and Sung [4] presented a review of the literature applying finite element techniques to the analysis and synthesis of elastic mechanisms.

This literature review will first present a general review of the elastic mechanism literature. The literature is classified by modeling and solution techniques, and by the use of experimental verification. This classification is followed by a more detailed review of the literature directly related to the elastic robot arm studied in this thesis.

2.1 Modeling Techniques

Exact modeling of the elastic deflections of a mechanism requires a continuous model. However, a continuous model of a mechanism is governed by partial differential equations that rarely have analytical solutions. Due to the lack of solutions for

continuous models, investigators of elastic mechanisms use finite degree of freedom models to approximate the elastic deformations. For example, the finite element method uses nodal displacements and rotations as degrees of freedom. In contrast, the assumed modes method uses the deflections of a finite number of assumed mode shapes as the degrees of freedom. In both cases the continuous elasticity problem is discretized. Thus, both of these methods yield ordinary differential equations, which can be solved more easily than partial differential equations of a continuous model.

2.1.1 Finite Element Method

The finite element method uses a set of nodal coordinates to represent the motion of each link. The strain and kinetic energies are expressed in terms of these nodal coordinates through the use of local basis functions, known as shape functions. This process generates a set of ordinary differential equations of motion which determine the motion of the mechanism. Some formulations use the nodal coordinates to represent both the gross and elastic motions of the mechanism. For these formulations, solution of the differential equations of motion determines the gross and elastic motions simultaneously. In other formulations, the nodal coordinates represent only the elastic motion. These formulations superimpose the elastic deformations upon the rigid body motion to obtain the total motion of the mechanism. Several of the finite element approaches used for elastic mechanisms are discussed below.

Turcic and Midha [5,6] use three dimensional quadrilateral elements in their finite element formulation. They include all acceleration terms, coupling between

the elastic and gross motions, and viscous material damping. Furthermore, they include the dynamic stiffness effect in the element stiffness matrix.

Cleghorn, Fenton, and Tabarrok [7] develop a formulation using seven degree of freedom planar beam elements. Their model also incorporates the dynamic stiffness effect. They present an example to demonstrate the importance of this effect.

Song and Haug [8] use a six degree of freedom planar beam element. These six coordinates are used to represent only the elastic motion of the element. The gross motion of the element is represented by the three rigid body coordinates; x, y , and ϕ . While they do not include damping in their model, all acceleration terms are retained, as is coupling between elastic and rigid body motion. Introduction of kinematic constraints between the links yields a mixed set of differential and algebraic equations.

Shabana and Wehage [9,10] extend the work of Song and Haug [8] into three dimensional elements, using Euler parameters as the angular coordinates. A component mode reduction technique is used to reduce the number of degrees of freedom in the model.

Sandor and Zhuang [11] model the mechanism links as discrete masses and elastic elements rather than as continuous elements. Additionally, they include proportional viscous damping and rotational inertia in their model. The resulting ordinary differential equations are simplified by dropping all nonlinear terms.

In a series of papers, Thompson et al. [12,13,14] develop a finite element formulation using planar, six degree of freedom beam elements. Their formulation includes the dynamic stiffness effect, proportional viscous damping, and constitutive equations for composite materials.

Sunada and Dubowsky [15] use the finite element method to model elastic effects in an industrial robot. Component mode synthesis is used to reduce the number of degrees of freedom in the model.

Most researchers define the elastic deformation of each finite element with respect to its own rigid configuration. Géradin et al. [16] defines the deformation of each element with respect to the rigid configuration of the entire mechanism. They argue that this reference configuration simplifies numerical integration of the equations of motion.

This review of the application of the finite element method to elastic mechanism analysis is not exhaustive. However, these papers are typical of the research in the area.

2.1.2 Assumed Modes Method

The assumed modes method represents the elastic deformations of each link as a linear combination of assumed mode shapes and deformation coordinates. In equation 2.1, $\Psi_i(x)$ are the assumed mode shapes and $D_i(t)$ the modal deformation coordinates. This assumption reduces the continuous representation of the link deformation, $v(x, t)$, to a discrete problem in the n modal deformation coordinates, $D_i(t)$.

$$v(x, t) = \sum_{i=1}^n D_i(t)\Psi_i(x) \quad (2.1)$$

Applications of this method to elastic structures have been successful, providing good approximations to natural frequencies and mode shapes when the continuous elasticity problem cannot be solved. This success has led numerous investigators to apply the assumed modes method to elastic mechanisms. Several of these studies

are summarized below.

Viscomi and Ayre [17] consider a slider crank mechanism with an elastic connecting rod. Modeling the connecting rod using Euler-Bernoulli beam theory, they apply Hamilton's Principle to obtain the partial differential equation of motion. Using the first two mode shapes of a simply supported beam, the assumed modes method is used to transform the partial differential equation to two coupled, nonlinear, time dependent, ordinary differential equations.

Chu and Pan [18] consider the same problem, a slider crank mechanism with an elastic connecting rod. They use an Euler-Bernoulli beam model, include viscous material damping, and model both axial and transverse deformations of the connecting rod. They use the first transverse mode shape of a simply supported beam to represent both the axial and transverse deformations.

Jasiński, Lee, and Sandor [19] also examine a slider crank mechanism with an elastic connecting rod. Their modeling technique is similar to [18], but does not retain the nonlinear coupling terms between the axial and transverse deformations.

Sutherland [20] analyzes a four bar mechanism with elastic crank, coupler, and rocker links. The assumed mode shape for the crank is the first mode shape of a cantilever beam, while both the coupler and rocker are modeled by the first mode of a simply supported beam. Viscous damping terms are included in the resulting set of ordinary differential equations, but nonlinear terms are neglected.

Jandrasits and Lowen [21] consider a four bar mechanism with an elastic rocker link and overhanging masses. The assumed mode shapes for the rocker are the modes of a simply supported beam with the same dimensions and overhanging masses.

Garcia-Reynoso and Seering [22] also consider a four bar mechanism, but let the rocker link, input shaft, and output shaft be elastic. By considering the mechanism at a particular configuration, they are able to derive the exact mode shapes for the rocker link. In addition they consider a case in which the first mode shape of a simply supported beam is used for the rocker. Their work shows that both the assumed mode shape and the torsional stiffnesses of the input and output shafts affect the natural frequencies of the model.

Kohli, Hunter, and Sandor [23] analyze a slider crank mechanism; modeling the axial and transverse deformations of the crank and connecting rod, as well as the deformations of the crank supports and the torsional deformations of the input shaft. Both of the links are modeled by the first two mode shapes of a simply supported beam. The differential equations of motion are linearized and viscous damping terms introduced. Their work shows that crank support elasticity can significantly affect the dynamic response of the mechanism.

Badlani and Kleinhenz [24] consider a slider crank mechanism with an elastic connecting rod. They develop two models, one using Euler-Bernoulli beam theory and another using a Timoshenko beam model. The assumed mode shapes for the connecting rod are those of a simply supported beam.

Badlani and Midha [25] model a slider crank mechanism with an elastic connecting rod, to examine the effect of damping. The Kelvin-Voigt damping model is used to model the viscoelastic behavior of the link while the connecting rod deformations are represented by the first mode shape of a simply supported beam.

Wielenga [26] uses floating reference frames for each elastic body, instead of the body-fixed reference frames used by most investigators. Use of the Buckens floating

reference frame simplifies the differential equations of motion when compared to the equations obtained with body-fixed reference frames.

Ryan [27] develops a multibody formulation that incorporates a number of complicating effects. These effects include torsional elasticity of beams, nonsymmetric beam bending, shear deformation, rotary inertia, and dynamic stiffness. The assumed mode shapes are obtained from the eigenvectors of a finite element model. In addition, the effect of the number and type of assumed modes upon the solution is studied.

2.2 Solution Techniques

Regardless of the modeling technique used, all investigations of elastic mechanisms obtain sets of second order, ordinary differential equations of the form of equation 2.2. \tilde{M} , \tilde{C} , and \tilde{K} are mass, damping, and stiffness matrices, \bar{q} is a vector of generalized coordinates, \bar{P} is the nonlinear term vector and \bar{F} is the forcing function vector.

$$\tilde{M}(t)\ddot{\bar{q}} + \tilde{C}(t)\dot{\bar{q}} + \tilde{K}(t)\bar{q} + \bar{P}(\bar{q}, \dot{\bar{q}}, t) = \bar{F}(t) \quad (2.2)$$

The various modeling techniques discussed earlier affect the form of \tilde{M} , \tilde{C} , \tilde{K} , \bar{P} , and \bar{F} as well as the number of differential equations. The approaches to solving these differential equations can be divided into two types, eigenanalysis and numerical integration.

2.2.1 Eigenanalysis

The eigenanalysis approach divides time into discrete intervals. Within each time interval, the mechanism is treated as a structure. The forces applied to the

structure are the inertial forces from a rigid body kinematic analysis of the mechanism. Equation 2.2 then simplifies to a set of constant coefficient, differential equations for each structural configuration of the mechanism. At each configuration, the set of differential equations is reduced to an eigenvalue problem. The resulting eigenvectors are used to decouple the differential equations. Each decoupled differential equation is then in the form of a single degree of freedom oscillator, for which a closed form solution is known. Superposition of the small elastic motion from the structural analysis and the gross motion from a rigid body analysis yields the total motion of the mechanism.

This approach makes three assumptions. First, the nonlinear term, \bar{P} , can be neglected or linearized. Many finite element and assumed modes formulations are so highly nonlinear that this assumption may not be reasonable. Second, the eigenvectors will decouple the damping matrix. Most investigators have insured this assumption by using proportional damping models. Third, coupling between the elastic and gross motions is not significant. Since the forces applied to the mechanism are the inertial forces from a rigid body analysis, this solution technique does not account for the effect of the elastic motion upon the rigid body motion.

Winfrey [28] applies the repeated structures method to the differential equations of an elastic four bar mechanism. To insure the continuity of the solution across the time interval boundaries, the displacements and velocities at the end of one interval are used as the initial conditions of the next interval.

Iman, Sandor, and Kramer [29] incorporate eigenvector derivatives into the eigenanalysis approach. Instead of solving the eigenvalue problem at each interval, the derivatives of the eigenvalues and eigenvectors with respect to the mechanism

driving coordinate are used to predict the eigenvectors at subsequent intervals. This technique offers a significant reduction in computation time.

Turcic and Midha [5] develop a method of handling nonlinear coupling terms in equation 2.2. The coupling terms are neglected and a solution obtained by the technique of Midha et al. [30]. Using this solution, the coupling terms are added to the differential equations and a new solution obtained in the same manner. This process is continued iteratively until the solution converges. For the examples considered by the authors, the incorporation of the coupling terms does not significantly alter the solution.

2.2.2 Numerical Integration

The numerical integration approach uses finite difference algorithms to integrate equation 2.2. This approach has been used extensively [20,23,31-37] because it can easily handle the nonlinear and coupling terms in equation 2.2. Its principal drawback is the small time step size required to capture the high frequency solutions typical in elastic mechanism analysis. Therefore, the computation times can be extremely large. Since most investigators have used well known numerical integration algorithms, only a few papers will be reviewed.

Chu and Pan [18] compare the fourth order Runge-Kutta numerical integration algorithm to an alternative solution procedure, the piecewise polynomial approximation technique. Their work shows this approximation technique to be as accurate as the Runge-Kutta method but with a much larger time step size; thereby reducing the computation time.

One problem with numerical integration of nonlinear differential equations con-

taining high frequency components is solution jump; in which the numerical algorithm may jump between multiple solutions. Viscomi and Ayre [17] encountered this problem while using Hamming's predictor-corrector method. Wielenga [26] applies the Gear stiff integration algorithm to prevent the multiple solution problem. Song and Haug [8] also apply the Gear algorithm. In addition, they employ sparse matrix algebra to reduce the computation time.

Shabana and Wehage [9] use two techniques to reduce the number of variables for which they had to integrate. First, they eliminate insignificant flexural modes of the elastic links by use of a component mode reduction technique. Second, coordinate partitioning is used to eliminate dependent coordinates prior to numerical integration.

2.3 Experimental Studies

Several researchers have conducted experimental studies of elastic mechanisms, in order to test the validity of analytical models. Several of these studies are presented below.

Alexander and Lawrence [34,37] present an experimental study of a four bar mechanism with elastic coupler and output links. The experimental time response is compared to predictions from a finite element model solved by numerical integration. The analytical model is able to predict the peak bending strains of the two links quite well. However, the magnitude and phase of the analytical time response differ significantly from the experimental response.

Cleghorn, Fenton, and Tabarrok [38] compare Alexander and Lawrence's experimental data [34,37] to predictions from their finite element model. Their model

includes the dynamic stiffness effect and coupling between elastic and rigid body motions. The comparison shows good agreement in magnitude and phase for the coupler link, but poor agreement for the output link. The agreement is improved by adding lumped bearing masses at the end of the links.

Turcic, Midha, and Bosnik [39] present experimental studies for a four bar mechanism with elastic coupler and output links. Predictions from the finite element model developed in [6] are compared to the experimental data. The time response magnitude and phase agree well for the coupler link, provided the dynamic stiffness effect is included in the analytical model. The peak magnitudes predicted by the analytical model agree well with the experimental data. However, this agreement deteriorates rapidly at higher input crank speeds.

Jandrasits and Lowen [40] consider a four bar mechanism with an elastic output link. The experimental data are compared to predictions from an assumed modes model developed in [21]. At most of the operating speeds considered, the experimental data and the analytical predictions agree well. A significant difference between their mechanism and mechanisms used in other experimental studies is its high stiffness.

Furuhashi, Saito, and Morita [36] test a four bar mechanism with an elastic coupler link. Comparison of the experimental time response to the prediction from a lumped parameter, finite element model shows very good agreement, both in magnitude and phase. As with the mechanism considered in [40], their mechanism is much stiffer than those considered by other investigators.

Sung, Thompson, Xing, and Wang [41] present experimental results for both a four bar and a slider crank mechanism. The four bar mechanism has elastic coupler

and output links while the slider crank mechanism has an elastic connecting rod. The experimental time responses are compared to predictions from a finite element model solved by numerical integration. These comparisons show the agreement between the analytical and experimental data is highly dependent upon the input crank speed of the mechanism. Thompson et al. [12,14,33] extend this work to include mechanisms fabricated from composite materials.

Liao, Sung, Thompson, and Soong [42] present experimental data for a four bar mechanism with elastic coupler and output links. The experimental data show the time responses of the links can be divided into quasi-static and resonant classes.

2.4 Elastic Arm Literature

This thesis investigates the dynamics of a single planar elastic robot arm. Therefore, this section will review a number of papers which have studied planar elastic arms. The literature is divided into two groups. The papers in the first group study the modeling of an elastic robot arm, while those in the second group address control of the arm.

Several researchers have studied modeling techniques for an elastic arm. Yigit, Scott, and Ulsoy [43] model an elastic arm mounted in a rigid hub, with a point mass at its tip. The assumed modes method is used to model the system, using the normal modes of a cantilever beam as the assumed mode shapes. Their formulation includes the centrifugal stiffening effect, but neglects gravity. They show the centrifugal stiffening effect and the effect of elastic motion upon the gross motion of the arm can be significant. In addition they show the magnitude of these effects is dependent upon the ratio of the rigid hub's mass moment of inertia to the elastic arm's mass

moment of inertia.

Hoia [44] studies an elastic arm with a point mass at its tip. He also allows the arm to be inclined to the plane of rotation. His finite element model shows that addition of a tip mass decreases the natural frequencies of the system when the angular velocity of the arm is small, but increases them for large angular velocities. This behavior is explained by the centrifugal stiffening effect.

Simo and Vu-Quoc [45] develop models for an elastic beam, using both linear and nonlinear strain theories. Their work shows that use of linear strain theory without incorporation of the centrifugal stiffening effect introduces errors into the model. Nonlinear strain theory accounts for the centrifugal stiffening effect.

A number of papers in the literature concentrate on control of an elastic robot arm, instead of modeling techniques. Cannon and Schmitz [46] model and test an elastic robot arm in the horizontal plane. They develop a mathematical model by use of the assumed modes method, using the normal modes of a pinned-free beam as the assumed mode shapes. The parameters in the model are determined experimentally, instead of analytically. They develop a controller to control the position of the tip of the elastic arm, in which the tip position is optically measured. Rovner and Cannon [47] extend this work by using time domain methods to estimate the parameters of the model, instead of the frequency domain methods used by Cannon and Schmitz [46].

Sakawa, Matsuno, and Fukushima [48] develop a controller for an elastic arm with an end mass, operating in the horizontal plane. The control law is developed by deriving the system's partial differential equations and then applying the Riccati equation. Experimental testing of an elastic arm shows the controller significantly

moment of inertia.

Hoia [44] studies an elastic arm with a point mass at its tip. He also allows the arm to be inclined to the plane of rotation. His finite element model shows that addition of a tip mass decreases the natural frequencies of the system when the angular velocity of the arm is small, but increases them for large angular velocities. This behavior is explained by the centrifugal stiffening effect.

Simo and Vu-Quoc [45] develop models for an elastic beam, using both linear and nonlinear strain theories. Their work shows that use of linear strain theory without incorporation of the centrifugal stiffening effect introduces errors into the model. Nonlinear strain theory accounts for the centrifugal stiffening effect.

A number of papers in the literature concentrate on control of an elastic robot arm, instead of modeling techniques. Cannon and Schmitz [46] model and test an elastic robot arm in the horizontal plane. They develop a mathematical model by use of the assumed modes method, using the normal modes of a pinned-free beam as the assumed mode shapes. The parameters in the model are determined experimentally, instead of analytically. They develop a controller to control the position of the tip of the elastic arm, in which the tip position is optically measured. Rovner and Cannon [47] extend this work by using time domain methods to estimate the parameters of the model, instead of the frequency domain methods used by Cannon and Schmitz [46].

Sakawa, Matsuno, and Fukushima [48] develop a controller for an elastic arm with an end mass, operating in the horizontal plane. The control law is developed by deriving the system's partial differential equations and then applying the Riccati equation. Experimental testing of an elastic arm shows the controller significantly

reduces the vibrations of the arm.

Kotnik, Yurkovich, and Özgüner [49] compare two different controllers for an elastic arm in the horizontal plane. The first uses position feedback, optically measuring the position of the tip of the arm. The second uses acceleration and position feedback, measuring the acceleration of the tip and the angular position of the input shaft. Their experiments show the performance of the acceleration feedback controller is superior to the optical position feedback system.

Book, Maizza-Neto, and Whitney [50] consider a planar two-arm elastic robot in the vertical plane, that carries masses at the end of each arm. They develop and compare control algorithms based on both rigid and elastic arm models. Their work shows that control algorithms based on rigid arm models may be as accurate as those based on more complex elastic arm models.

3 ANALYTICAL MODEL OF AN ELASTIC ARM

The elastic arm studied in this thesis is shown in Figure 3.1. A uniform, homogeneous, slender beam is rigidly attached to a lumped inertia that may rotate with respect to ground. A linear torsional spring of negligible mass is connected between the lumped inertia and the ground. Gravity is constant and acts in the negative \bar{J} direction.

Modeling of the beam deformations are simplified by limiting them to the \bar{j} direction. Therefore, axial and out of plane deformations are assumed to be negligible. Shear deformations of the beam are also neglected, as is material damping. Based upon these assumptions, the Euler-Bernoulli beam model is used to model the elastic deformations.

In this chapter, exact, assumed modes, and rigid models of the elastic arm are derived. The nonlinear boundary value problem of the elastic is derived. The exact model is the solution to the linearized boundary value problem. The assumed modes model discretizes the nonlinear boundary value problem by use of assumed mode shapes, resulting in a set of nonlinear ordinary differential equations. These differential equations are then linearized. The rigid model neglects the elasticity of the arm. In later chapters, these models are used to determine the effect of mode shape selection, coupling between elastic and rigid motions, and gravity upon the

elastic arm.

3.1 Derivation of Exact Model

The exact model uses two independent coordinates; one rigid body coordinate, $\theta(t)$, and one continuous coordinate for the transverse deformation, $v(x, t)$. The kinetic and potential energies of the system are expressed in terms of these coordinates. Hamilton's Principle then yields the partial differential equations and boundary conditions of the problem.

Two coordinate systems are used in this model. As shown in Figure 3.1, the $\bar{I}\bar{J}\bar{K}$ coordinate system is attached to ground. The $\bar{i}\bar{j}\bar{k}$ coordinate system is attached to a hypothetical rigid arm. The deformations of the arm are measured with respect to the later coordinate system.

The kinetic energy expression for the system is divided into two parts, the kinetic energy of the lumped inertia and of the elastic arm. The former is described in terms of θ , the rigid body coordinate.

$$T = \frac{1}{2} J_I \dot{\theta}^2 \quad (3.1)$$

To obtain the kinetic energy of the elastic arm, consider an infinitesimal element of the arm at point P. Then the kinetic energy of the arm is expressed by equation 3.2, in which \bar{r}_P denotes the position of the infinitesimal element.

$$T = \int \frac{1}{2} \dot{\bar{r}}_P \cdot \dot{\bar{r}}_P dm \quad (3.2)$$

The position vector \bar{r}_P is expressed as the sum of $x\bar{i}$, the distance along the axis of the rigid arm, and $v\bar{j}$, the elastic displacement.

$$\bar{r}_P = x\bar{i} + v\bar{j} \quad (3.3)$$

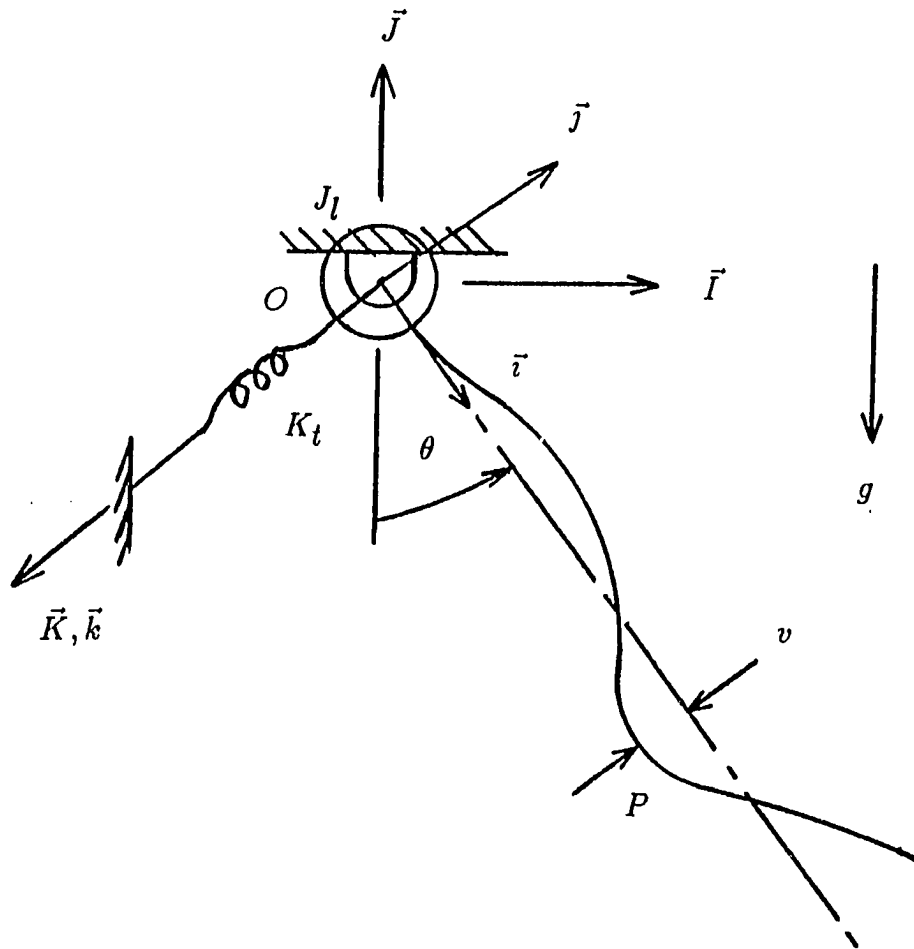


Figure 3.1: Elastic arm system

By use of the following coordinate transformations, the position vector is expressed in terms of the $\bar{I}\bar{J}\bar{K}$ coordinate system.

$$\bar{i} = \sin \theta \bar{I} - \cos \theta \bar{J} \quad (3.4)$$

$$\bar{j} = \cos \theta \bar{I} + \sin \theta \bar{J} \quad (3.5)$$

The resulting position vector is given by equation 3.6.

$$\bar{r}_P = [x \sin \theta - v \cos \theta] \bar{I} + [v \sin \theta - x \cos \theta] \bar{J} \quad (3.6)$$

Differentiating equation 3.6 with respect to time yields the velocity vector, equation 3.7.

$$\begin{aligned} \dot{\bar{r}}_P = & [x\dot{\theta} \cos \theta + \dot{v} \cos \theta - v\dot{\theta} \sin \theta] \bar{I} \\ & + [\dot{v} \sin \theta + v\dot{\theta} \cos \theta + x\dot{\theta} \sin \theta] \bar{J} \end{aligned} \quad (3.7)$$

To evaluate the kinetic energy expression, let the beam have cross sectional area, A , and density ρ . Then the mass of the infinitesimal element can be expressed by equation 3.8

$$dm = \rho A dx \quad (3.8)$$

Substituting equations 3.7 and 3.8 into equation 3.2 yields the kinetic energy expression for the arm.

$$T = \int_0^l \frac{\rho A}{2} [x^2 \dot{\theta}^2 + 2x\dot{\theta}\dot{v} + \dot{v}^2 + \dot{\theta}^2 v^2] dx \quad (3.9)$$

Equation 3.10, the total kinetic energy of the system, is obtained by summing equations 3.1 and 3.9.

$$T = \int_0^l \frac{\rho A}{2} [x^2 \dot{\theta}^2 + 2x\dot{\theta}\dot{v} + \dot{v}^2 + \dot{\theta}^2 v^2] dx + \frac{1}{2} J_l \dot{\theta}^2 \quad (3.10)$$

The potential energy of the system is divided into three parts; the elastic energy of the torsional spring, and the elastic and gravitational energies of the arm. The potential energy of the torsional spring is expressed in terms of θ .

$$\Pi_s = \frac{1}{2} K_t \theta^2 \quad (3.11)$$

The elastic energy of the arm is derived from the Euler-Bernoulli beam model.

$$\Pi_e = \int_0^l \frac{EI}{2} (v'')^2 dx \quad (3.12)$$

The gravitational potential energy of the elastic beam is obtained from the following equation:

$$\Pi_g = \int gy dm \quad (3.13)$$

where y is extracted from the \vec{J} component of equation 3.6.

$$y = v \sin \theta - x \cos \theta \quad (3.14)$$

The final expression for the gravitational potential energy is obtained by substituting equations 3.8 and 3.14 into equation 3.13.

$$\Pi_g = \int_0^l \rho Ag [v \sin \theta - x \cos \theta] dx \quad (3.15)$$

Summation of equations 3.11, 3.12, and 3.15 yields the total potential energy of the system.

$$\Pi = \frac{1}{2} K_t \theta^2 + \int_0^l \frac{EI}{2} (v'')^2 dx + \int_0^l \rho Ag [v \sin \theta - x \cos \theta] dx \quad (3.16)$$

The following form of Hamilton's Principle is used.

$$\delta \int_{t_1}^{t_2} (T - \Pi) dt + \int_{t_1}^{t_2} \delta W_{nc} dt = 0 \quad (3.17)$$

where θ and v are the independent coordinates. The only nonconservative forces are the reaction forces at point O. These forces do no work since the virtual displacement of point O is zero. Therefore, δW_{nc} vanishes in this problem. Substitute equations 3.10 and 3.16 into equation 3.17 and complete the first variation.

$$\begin{aligned} & \int_{t_1}^{t_2} \left\{ \int_0^l \rho A (x^2 \dot{\theta} + v^2 \dot{\theta} + x \dot{v}) \delta \theta dx - \int_0^l EI v'' \delta v'' dx \right\} dt \\ & + \int_{t_1}^{t_2} \left\{ \int_0^l \rho A (v \dot{\theta}^2 - g \sin \theta) \delta v dx + \int_0^l \rho A (\dot{v} + x \dot{\theta}) \delta v dx \right\} dt \\ & + \int_{t_1}^{t_2} \left\{ - \int_0^l \rho A g (v \cos \theta + x \sin \theta) \delta \theta dx + (J_l \dot{\theta} \delta \dot{\theta} - K_t \theta \delta \theta) \right\} dt = 0 \quad (3.18) \end{aligned}$$

The variations of the derivatives of θ and v are reduced to variations in θ and v by integration by parts. With this reduction, the variational statement simplifies to equation 3.19.

$$\begin{aligned} & \int_{t_1}^{t_2} \left\{ \int_0^l [-\rho A (x^2 \ddot{\theta} + v^2 \ddot{\theta} + 2v \dot{v} \dot{\theta} + x \ddot{v}) - \rho A g (v \cos \theta + x \sin \theta)] dx \right\} \delta \theta dt \\ & - \int_{t_1}^{t_2} \{-J_l \ddot{\theta} - K_t \theta\} \delta \theta dt + \int_{t_1}^{t_2} \{(EI v'') \delta v'(0)\} dt \\ & + \int_{t_1}^{t_2} \left\{ \int_0^l \rho A \left[v \dot{\theta}^2 - g \sin \theta - \ddot{v} - x \ddot{\theta} - \frac{1}{\rho A} (EI v'')'' \right] \delta v dx \right\} dt \\ & + \int_{t_1}^{t_2} \left\{ (EI v'')' \delta v(l) - (EI v'')' \delta v(0) - (EI v'') \delta v'(l) \right\} dt = 0 \quad (3.19) \end{aligned}$$

This variational statement generates two partial differential equations:

$$- \int_0^l \rho A (x^2 \ddot{\theta} + v^2 \ddot{\theta} + 2v \dot{v} \dot{\theta} + x \ddot{v} + g (v \cos \theta + x \sin \theta)) dx - J_l \ddot{\theta} - K_t \theta = 0 \quad (3.20)$$

$$v \dot{\theta}^2 - g \sin \theta - \ddot{v} - x \ddot{\theta} - \frac{1}{\rho A} (EI v'')'' = 0 \quad (3.21)$$

two geometric boundary conditions:

$$v(0, t) = 0 \quad (3.22)$$

$$v'(0, t) = 0 \quad (3.23)$$

and two natural boundary conditions:

$$(EIv'')_l = 0 \quad (3.24)$$

$$(EIv'')'_l = 0 \quad (3.25)$$

The solution to this boundary value problem may be obtained if the beam is uniform and homogeneous and the partial differential equations are linearized about the equilibrium point, $(\theta, v) = (0, 0)$. Define a new material constant:

$$a^2 = \frac{EI}{\rho A} \quad (3.26)$$

and linearize the partial differential equations. Equations 3.20 and 3.21 reduce to the following forms.

$$-K_t \theta - \ddot{\theta} \left(J_l + \frac{\rho A l^3}{3} \right) - \rho A \int_0^l (x \ddot{v} + gv) dx - \frac{\rho A g l^2 \theta}{2} = 0 \quad (3.27)$$

$$-g\theta - \ddot{v} - x\ddot{\theta} - a^2 \frac{\partial^4 v}{\partial x^4} = 0 \quad (3.28)$$

Apply a separation of variables method to the problem by substituting the following equations into equation 3.28.

$$v(x, t) = Y(x) e^{j\omega t} \quad (3.29)$$

$$\theta(t) = \Theta e^{j\omega t} \quad (3.30)$$

The following differential equation is obtained.

$$\frac{\partial^4 Y}{\partial x^4} - \frac{\omega^2}{a^2} Y = \frac{\Theta}{a^2} (x\omega^2 - g) \quad (3.31)$$

The homogeneous and particular solutions to equation 3.31 are given by equations 3.32 and 3.33:

$$Y_h(x) = C_1 \sin(\alpha x) + C_2 \cos(\alpha x) + C_3 \sinh(\alpha x) - C_4 \cosh(\alpha x) \quad (3.32)$$

$$Y_p(x) = \Theta \left(\frac{g}{\omega^2} - x \right) \quad (3.33)$$

where:

$$\alpha = \sqrt{\frac{\omega}{a}} \quad (3.34)$$

The total solution is the sum of the homogeneous and particular solutions.

$$Y(x) = C_1 \sin(\alpha x) + C_2 \cos(\alpha x) + C_3 \sinh(\alpha x) - C_4 \cosh(\alpha x) + \Theta \left(\frac{g}{\omega^2} - x \right) \quad (3.35)$$

The unknown coefficients in equation 3.35 are determined by substitution of equations 3.29 and 3.30 into the first partial differential equation, equation 3.27, and the boundary conditions, equations 3.22 to 3.25. The following five equations are obtained.

$$-K_t \Theta + \omega^2 \Theta \left(J_l + \frac{\rho A l^3}{3} \right) + \omega^2 \rho A \int_0^l x Y(x) dx - \rho A g \int_0^l Y(x) dx - \frac{\rho A g l^2 \Theta}{2} = 0 \quad (3.36)$$

$$Y(0) = 0 \quad (3.37)$$

$$\frac{\partial Y}{\partial x}(0) = 0 \quad (3.38)$$

$$\frac{\partial^2 Y}{\partial x^2}(l) = 0 \quad (3.39)$$

$$\frac{\partial^3 Y}{\partial x^3}(l) = 0 \quad (3.40)$$

Substitution of equation 3.35 into equations 3.36 to 3.40 yields the following set of equations.

$$\begin{aligned} & \Theta \left\{ \omega^2 J_l - K_t + \rho A l \left(\frac{gl}{2} - \frac{g^2}{\omega^2} \right) \right\} \\ & + C_1 \left\{ a\omega\rho A \sin(\alpha l) + \frac{\rho A}{\alpha} \cos(\alpha l) (g - l\omega^2) - \frac{\rho A g}{\alpha} \right\} \\ & + C_2 \left\{ a\omega\rho A \cos(\alpha l) + \frac{\rho A}{\alpha} \sin(\alpha l) (l\omega^2 - g) - a\omega\rho A \right\} \\ & + C_3 \left\{ \frac{\rho A}{\alpha} \cosh(\alpha l) (l\omega^2 - g) - a\omega\rho A \sinh(\alpha l) + \frac{\rho A g}{\alpha} \right\} \\ & + C_4 \left\{ \frac{\rho A}{\alpha} \sinh(\alpha l) (l\omega^2 - g) - a\omega\rho A \cosh(\alpha l) + a\omega\rho A \right\} = 0 \end{aligned} \quad (3.41)$$

$$\Theta \left(\frac{g}{\omega^2} \right) + C_2 + C_4 = 0 \quad (3.42)$$

$$-\Theta + \alpha C_1 - \alpha C_3 = 0 \quad (3.43)$$

$$\begin{aligned} C_1 (-\alpha^2 \sin(\alpha l)) + C_2 (-\alpha^2 \cos(\alpha l)) + C_3 (\alpha^2 \sinh(\alpha l)) \\ + C_4 (\alpha^2 \cosh(\alpha l)) = 0 \end{aligned} \quad (3.44)$$

$$\begin{aligned} C_1 (-\alpha^3 \cos(\alpha l)) + C_2 (\alpha^3 \sin(\alpha l)) + C_3 (\alpha^3 \cosh(\alpha l)) \\ + C_4 (\alpha^3 \sinh(\alpha l)) = 0 \end{aligned} \quad (3.45)$$

If the preceding equations are used in the following order, 3.42, 3.43, 3.44, 3.45, and 3.41; they may be expressed in the following matrix form;

$$\begin{bmatrix} B_{11} & 0 & 1 & 0 & 1 \\ B_{21} & B_{22} & 0 & B_{24} & 0 \\ 0 & B_{32} & B_{33} & B_{34} & B_{35} \\ 0 & B_{42} & B_{43} & B_{44} & B_{45} \\ B_{51} & B_{52} & B_{53} & B_{54} & B_{55} \end{bmatrix} \begin{Bmatrix} \Theta \\ C_1 \\ C_2 \\ C_3 \\ C_4 \end{Bmatrix} = \bar{0} \quad (3.46)$$

where the B_{ij} symbolically represent the coefficients of the equations. For a nontrivial solution, the determinant of the coefficient matrix must vanish. This condition

on the determinant yields the characteristic equation of the problem; which may be solved numerically for the circular natural frequencies of the system. For brevity, the characteristic equation is not shown.

The mode shapes of the exact solution may also be obtained. The i th mode shape is represented by equation 3.35, where ω is the i th root of the characteristic equation. The values for C_j and Θ are obtained in the following manner.

Solve the first equation of equation 3.46 for C_2 .

$$C_2 = -C_4 - B_{11}\Theta \quad (3.47)$$

Substitute equation 3.47 into the last three equations of equation 3.46. The following equations are obtained.

$$C_1 B_{32} + C_3 B_{34} + C_4 (B_{35} - B_{33}) = B_{11} B_{33} \Theta \quad (3.48)$$

$$C_1 B_{42} + C_3 B_{44} + C_4 (B_{45} - B_{43}) = B_{11} B_{43} \Theta \quad (3.49)$$

$$C_1 B_{52} + C_3 B_{54} + C_4 (B_{55} - B_{53}) = (B_{11} B_{53} - B_{51}) \Theta \quad (3.50)$$

Solve the second equation of equation 3.46 for C_1 .

$$C_1 = \frac{-C_3 B_{24} - B_{21} \Theta}{B_{22}} \quad (3.51)$$

Substitute equation 3.51 into equations 3.48 to 3.50. The following equations are obtained.

$$C_3 \left(B_{34} - \frac{B_{24} B_{32}}{B_{22}} \right) + C_4 (B_{35} - B_{33}) = \Theta \left(B_{11} B_{33} + \frac{B_{21} B_{32}}{B_{22}} \right) \quad (3.52)$$

$$C_3 \left(B_{44} - \frac{B_{24} B_{42}}{B_{22}} \right) + C_4 (B_{45} - B_{43}) = \Theta \left(B_{11} B_{43} + \frac{B_{21} B_{42}}{B_{22}} \right) \quad (3.53)$$

$$C_3 \left(B_{54} - \frac{B_{52} B_{24}}{B_{22}} \right) + C_4 (B_{55} - B_{53}) = \Theta \left(B_{11} B_{53} - B_{51} + \frac{B_{21} B_{52}}{B_{22}} \right) \quad (3.54)$$

Solve equation 3.54 for C_4 .

$$C_4 = \frac{1}{B_{55} - B_{53}} \left[\Theta \left(B_{11} B_{53} - B_{51} + \frac{B_{21} B_{52}}{B_{22}} \right) - C_3 \left(B_{54} - \frac{B_{52} B_{24}}{B_{22}} \right) \right] \quad (3.55)$$

Substitute equation 3.55 into equations 3.52 and 3.53. The following equations are obtained.

$$= \Theta \left[B_{11} B_{33} + \frac{B_{21} B_{32}}{B_{22}} - \left(\frac{B_{35} - B_{33}}{B_{55} - B_{53}} \right) \left(B_{11} B_{53} - B_{51} + \frac{B_{21} B_{52}}{B_{22}} \right) \right] \quad (3.56)$$

$$= \Theta \left[B_{11} B_{43} + \frac{B_{21} B_{42}}{B_{22}} - \left(\frac{B_{45} - B_{43}}{B_{55} - B_{53}} \right) \left(B_{11} B_{53} - B_{51} + \frac{B_{21} B_{52}}{B_{22}} \right) \right] \quad (3.57)$$

Equations 3.56 and 3.57 are linearly dependent. Therefore, either may be used to solve for the ratio of C_3 to Θ .

To find the coefficients, set Θ arbitrarily. Use equation 3.56 to solve for C_3 . C_4 is then obtained from equation 3.55. C_1 is obtained from equation 3.51 and C_2 from equation 3.47.

3.2 Derivation of Assumed Modes Model

The previous section derived the exact solution to the linearized boundary value problem of the elastic arm. However, this may not always be possible. Therefore, an alternative solution procedure is desirable. One alternative solution procedure is the assumed modes method. The nonlinear boundary value problem is discretized by use of a finite number of assumed mode shapes. The resulting set of ordinary

differential equations are linearized and formulated as an eigenvalue problem. The natural frequencies are then computed.

The boundary value problem of the previous section may be transformed to an assumed modes formulation by a simple substitution. Assume the elastic displacement, v , may be written as a linear combination of the assumed mode shapes, $\Psi_i(x)$, and the deformation coordinates, $D_i(t)$.

$$v(x, t) = \sum_{i=1}^n D_i(t) \Psi_i(x) = \bar{D}^T \bar{\Psi} \quad (3.58)$$

where

$$\begin{aligned} \bar{D}^T &= \{D_1(t) \ D_2(t) \ \cdots \ D_n(t)\} \\ \bar{\Psi}^T &= \{\Psi_1(x) \ \Psi_2(x) \ \cdots \ \Psi_n(x)\} \end{aligned}$$

Substitute equation 3.58 into the kinetic energy expression for the system, equation 3.10.

$$T = \int_0^l \frac{\rho A}{2} \left[x^2 \dot{\theta}^2 + 2x \dot{\theta} \dot{\bar{D}}^T \bar{\Psi} + \left(\dot{\bar{D}}^T \bar{\Psi} \right)^2 + \dot{\theta}^2 \left(\bar{D}^T \bar{\Psi} \right)^2 \right] dx + \frac{1}{2} J_I \dot{\theta}^2 \quad (3.59)$$

This equation is then simplified via the following transformation:

$$\left(\dot{\bar{D}}^T \bar{\Psi} \right)^2 = \left(\dot{\bar{D}}^T \bar{\Psi} \right) \left(\dot{\bar{D}}^T \bar{\Psi} \right)^T = \dot{\bar{D}}^T \bar{\Psi} \bar{\Psi}^T \dot{\bar{D}} = \dot{\bar{D}}^T \bar{\Psi} \dot{\bar{D}} \quad (3.60)$$

where $\bar{\Psi}$ is an n by n modal matrix defined by equation 3.61.

$$\bar{\Psi} = \bar{\Psi} \bar{\Psi}^T \quad (3.61)$$

A similar reduction is performed on the $\left(\bar{D}^T \bar{\Psi} \right)^2$ term.

$$T = \int_0^l \frac{\rho A}{2} \left[x^2 \dot{\theta}^2 + 2x \dot{\theta} \dot{\bar{D}}^T \bar{\Psi} + \dot{\bar{D}}^T \bar{\Psi} \dot{\bar{D}} + \dot{\theta}^2 \bar{D}^T \bar{\Psi} \bar{D} \right] dx + \frac{1}{2} J_I \dot{\theta}^2 \quad (3.62)$$

Substitute equation 3.58 into the potential energy expression, equation 3.16; and utilize a transformation similar to that of equation 3.60.

$$\Pi = \frac{1}{2} K_t \theta^2 + \int_0^l \frac{EI}{2} \bar{D}^T \tilde{\Upsilon} \bar{D} + \int_0^l \rho A g \left[\bar{D}^T \bar{\Psi} \sin \theta - x \cos \theta \right] dx \quad (3.63)$$

In the preceding equation, $\tilde{\Upsilon}$ is a n by n modal matrix defined by equation 3.64.

$$\tilde{\Upsilon} = \bar{\Psi}'' \bar{\Psi}''^T \quad (3.64)$$

For a finite degree of freedom problem, Hamilton's Principle reduces to equation 3.65 [51];

$$\frac{d}{dt} \left(\frac{\partial T}{\partial \dot{\bar{q}}} \right) - \frac{\partial T}{\partial \bar{q}} + \frac{\partial \Pi}{\partial \bar{q}} = \bar{Q} \quad (3.65)$$

where \bar{q} is a vector of the independent coordinates.

$$\bar{q}^T = \{ \theta \ D_1 \ D_2 \ \dots \ D_n \} \quad (3.66)$$

The only external nonconservative forces are the reaction forces at point O. However, these forces do no work since the virtual displacement of point O is zero. Therefore, the generalized force vector, \bar{Q} , is zero. Differentiation of equations 3.62 and 3.63 yields the following expressions.

$$\frac{\partial T}{\partial \dot{\bar{q}}} = \int_0^l \rho A \left\{ \begin{array}{c} x^2 \dot{\theta} + x \dot{\bar{D}}^T \bar{\Psi} + \dot{\theta} \bar{D}^T \bar{\Psi} \bar{D} \\ x \dot{\theta} \bar{\Psi} + \bar{\Psi} \dot{\bar{D}} \end{array} \right\} dx + \left\{ \begin{array}{c} J_l \dot{\theta} \\ \bar{0} \end{array} \right\} \quad (3.67)$$

$$\begin{aligned} \frac{d}{dt} \left(\frac{\partial T}{\partial \dot{\bar{q}}} \right) &= \int_0^l \rho A \left\{ \begin{array}{c} x^2 \ddot{\theta} + x \ddot{\bar{D}}^T \bar{\Psi} + \ddot{\theta} \bar{D}^T \bar{\Psi} \bar{D} + 2 \dot{\theta} \dot{\bar{D}}^T \bar{\Psi} \bar{D} \\ x \ddot{\theta} \bar{\Psi} + \bar{\Psi} \ddot{\bar{D}} \end{array} \right\} dx \\ &\quad + \left\{ \begin{array}{c} J_l \ddot{\theta} \\ \bar{0} \end{array} \right\} \end{aligned} \quad (3.68)$$

$$\frac{\partial T}{\partial \bar{q}} = \int_0^l \rho A \left\{ \begin{array}{c} 0 \\ \dot{\theta}^2 \bar{\Psi} \bar{D} \end{array} \right\} dx \quad (3.69)$$

$$\begin{aligned} \frac{\partial \Pi}{\partial \bar{q}} = & K_t \left\{ \begin{array}{c} \theta \\ \bar{0} \end{array} \right\} + \int_0^l EI \left\{ \begin{array}{c} 0 \\ \bar{\Upsilon} \bar{D} \end{array} \right\} dx \\ & + \int_0^l \rho A g \left\{ \begin{array}{c} \bar{D}^T \bar{\Psi} \cos \theta + x \sin \theta \\ \bar{\Psi} \sin \theta \end{array} \right\} dx \end{aligned} \quad (3.70)$$

The equations of motion are obtained by substituting equations 3.68, 3.69, and 3.70 into equation 3.65 and using transformations of the following form.

$$\left(\ddot{\bar{D}}^T \bar{\Psi} \right) = \left(\ddot{\bar{D}}^T \bar{\Psi} \right)^T = \bar{\Psi}^T \ddot{\bar{D}} \quad (3.71)$$

The resulting set of $n - 1$, nonlinear ordinary differential equations is shown in equation 3.72.

$$\bar{M} \left\{ \begin{array}{c} \ddot{\theta} \\ \ddot{\bar{D}} \end{array} \right\} - \bar{K} \left\{ \begin{array}{c} \theta \\ \bar{D} \end{array} \right\} + \bar{P} = \bar{0} \quad (3.72)$$

where \bar{M} , \bar{K} , and \bar{P} are as follows. \bar{M} and \bar{K} are constant mass and stiffness matrices of the system, while \bar{P} is a vector of nonlinear terms.

$$\bar{M} = \left[\begin{array}{cc} \int_0^l \rho A x^2 dx + J_l & \int_0^l \rho A x \bar{\Psi}^T dx \\ \int_0^l \rho A x \bar{\Psi} dx & \int_0^l \rho A \bar{\Psi} dx \end{array} \right] \quad (3.73)$$

$$\bar{K} = \left[\begin{array}{cc} K_t & \bar{0}^T \\ \bar{0} & \int_0^l EI \bar{\Upsilon} dx \end{array} \right] \quad (3.74)$$

$$\bar{P} = \left\{ \begin{array}{l} \int_0^l \rho A (\ddot{\theta} \bar{D}^T \bar{\Psi} \bar{D} + 2\dot{\theta} \dot{\bar{D}}^T \bar{\Psi} \bar{D}) dx + \int_0^l \rho Ag (\bar{D}^T \bar{\Psi} \cos \theta + x \sin \theta) dx \\ \int_0^l \rho Ag \bar{\Psi} \sin \theta dx - \int_0^l \rho A \dot{\theta}^2 \bar{\Psi} \bar{D} dx \end{array} \right\} \quad (3.75)$$

To obtain the natural frequencies of the system from equation 3.72, \bar{P} is linearized about the equilibrium point $\bar{q} = 0$. This is accomplished by approximating $\cos \theta$ by 1, $\sin \theta$ by θ , and neglecting all terms of second order and higher. This linearization only alters the stiffness matrix. The coupled differential equations reduce to the following form:

$$\bar{M} \ddot{\bar{q}} + \bar{K} \bar{q} = \bar{0} \quad (3.76)$$

where \bar{K} is the modified stiffness matrix.

$$\bar{K} = \begin{bmatrix} K_t + \int_0^l \rho Ag x dx & \int_0^l \rho Ag \bar{\Psi}^T dx \\ \int_0^l \rho Ag \bar{\Psi} dx & \int_0^l EI \ddot{\gamma} dx \end{bmatrix} \quad (3.77)$$

Assuming simple harmonic motion, the accelerations are related to the displacements.

$$\ddot{\bar{q}} = -\omega^2 \bar{q} \quad (3.78)$$

Substituting this relationship into equation 3.76 reduces the set of differential equations to a generalized eigenvalue problem;

$$\bar{K} \bar{q} = \omega^2 \bar{M} \bar{q} \quad (3.79)$$

which may be solved for the natural frequencies of the system.

3.2.1 Selection of Assumed Mode Shapes

The fundamental assumption of the assumed modes model is the elastic deformations of the arm may be represented as a linear combination of the assumed

mode shapes and deformation coordinates.

$$v(x, t) = \bar{D}^T \bar{\Psi} \quad (3.80)$$

In the derivation of the model, the selection of the Ψ_j functions was not discussed. However, the accuracy of the model is dependent upon the type and number of assumed mode shapes. Therefore, a review of the theoretical basis for selecting the mode shapes is important.

Assumed mode shapes may be divided into three classes; admissible functions, comparison functions, and eigenfunctions [52]. The criteria for this division are the three parts of the governing boundary value problem; partial differential equations, geometric boundary conditions, and natural boundary conditions. Admissible functions are any arbitrary functions that satisfy the geometric boundary conditions of the boundary value problem. Comparison functions are more restrictive; they must satisfy both the geometric and the natural boundary conditions. Eigenfunctions are the most restrictive class. They must satisfy the partial differential equations as well as all of the boundary conditions.

Since the eigenfunctions are solutions for the boundary value problem, they are the exact mode shapes of the problem. Therefore, an assumed modes model that uses the eigenfunctions of the problem will also be exact, for the number of modes included in the model. However, the eigenfunctions can rarely be obtained for realistic problems. Therefore, the simpler admissible and comparison functions are used to obtain approximate models of the system.

The theory of the assumed modes method presents few guidelines for selecting the admissible or comparison functions. One desirable characteristic of the approximate solution is that it converges to the true solution as the number of degrees of

freedom increases to infinity. This characteristic can be guaranteed if the assumed mode shapes satisfy the following conditions [51].

1. The assumed mode shapes are linearly independent.
2. The assumed mode shapes are continuous and p times differentiable, where p is the highest order derivative in the governing partial differential equation.
3. The assumed mode shapes satisfy the geometric boundary conditions of the problem.
4. The set of assumed mode shapes is complete. Complete is used in the mathematical sense. This condition can be satisfied by selecting the mode shapes from the lowest order to the highest order, without missing any intermediate terms [51]. For example, the set $\{ 1 \ x \ x^2 \}$ is complete, while $\{ 1 \ x^2 \ x^3 \}$ is incomplete.

Although these conditions guarantee convergence of the solution, they cannot determine the rate of convergence.

Since theory provides few guidelines for selection of the assumed mode shapes, this thesis studies the effect of mode shape selection by comparison of models using different assumed mode shapes. This topic will be addressed in Chapters 4 and 5.

3.3 Derivation of Rigid Model

For purposes of comparison, a rigid model of the robot arm is derived. Assume the arm is rigid. Using the free body diagram shown in Figure 3.2 and summing moments about point O yields the equation of motion.

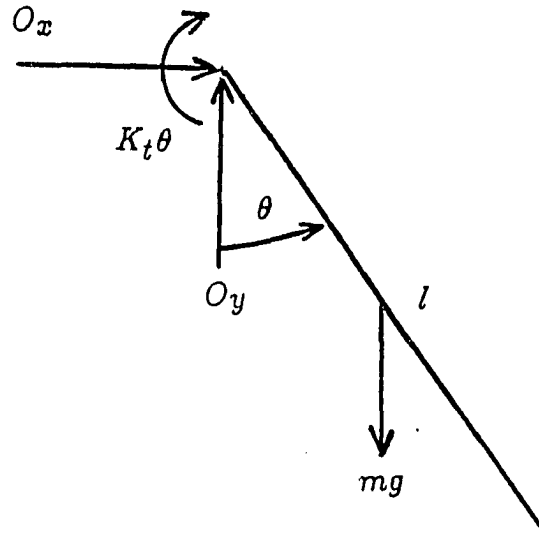


Figure 3.2: Free body diagram of rigid arm

$$-K_t \theta - \frac{mgl}{2} \sin \theta = \left(\frac{ml^2}{3} + J_l \right) \ddot{\theta} \quad (3.81)$$

Linearize the $\sin \theta$ term by assuming θ is small. Then equation 3.81 reduces to the differential equation of a undamped oscillator.

$$\left(J_l + \frac{ml^2}{3} \right) \ddot{\theta} + \left(K_t + \frac{mgl}{2} \right) \theta = 0 \quad (3.82)$$

Therefore, the only natural frequency available from the rigid model is given by equation 3.83.

$$f_r = \frac{1}{2\pi} \sqrt{\frac{K_t + \frac{mgl}{2}}{J_l + \frac{ml^2}{3}}} \quad (3.83)$$

4 COMPARISON OF MODELS

This chapter examines the accuracy of the models developed in Chapter 3, by comparing their natural frequencies to experimentally measured natural frequencies. The next section describes the experimental apparatus and procedure used to measure the natural frequencies. Following sections compare the experimental frequencies to the natural frequencies obtained from the models, and address the topics of assumed mode shape selection, coupling of gross and elastic motions, and gravity.

4.1 Experimental Apparatus and Procedure

The experimental apparatus for testing the elastic arm system is shown in Figure 4.1. A long thin elastic beam is clamped in a rigid block. The block is attached to a shaft, which is free to rotate in a pair of anti-friction bearings. A pair of coil tension springs induces a torsional stiffness about the shaft. The coil springs are used instead of a wire torsion spring, to reduce friction. The entire system is mounted on a stiff beam.

The natural frequencies of the system are determined from the frequency content of its free vibration response. The response of the system is determined by measuring both displacement and acceleration. Due to the low natural frequencies

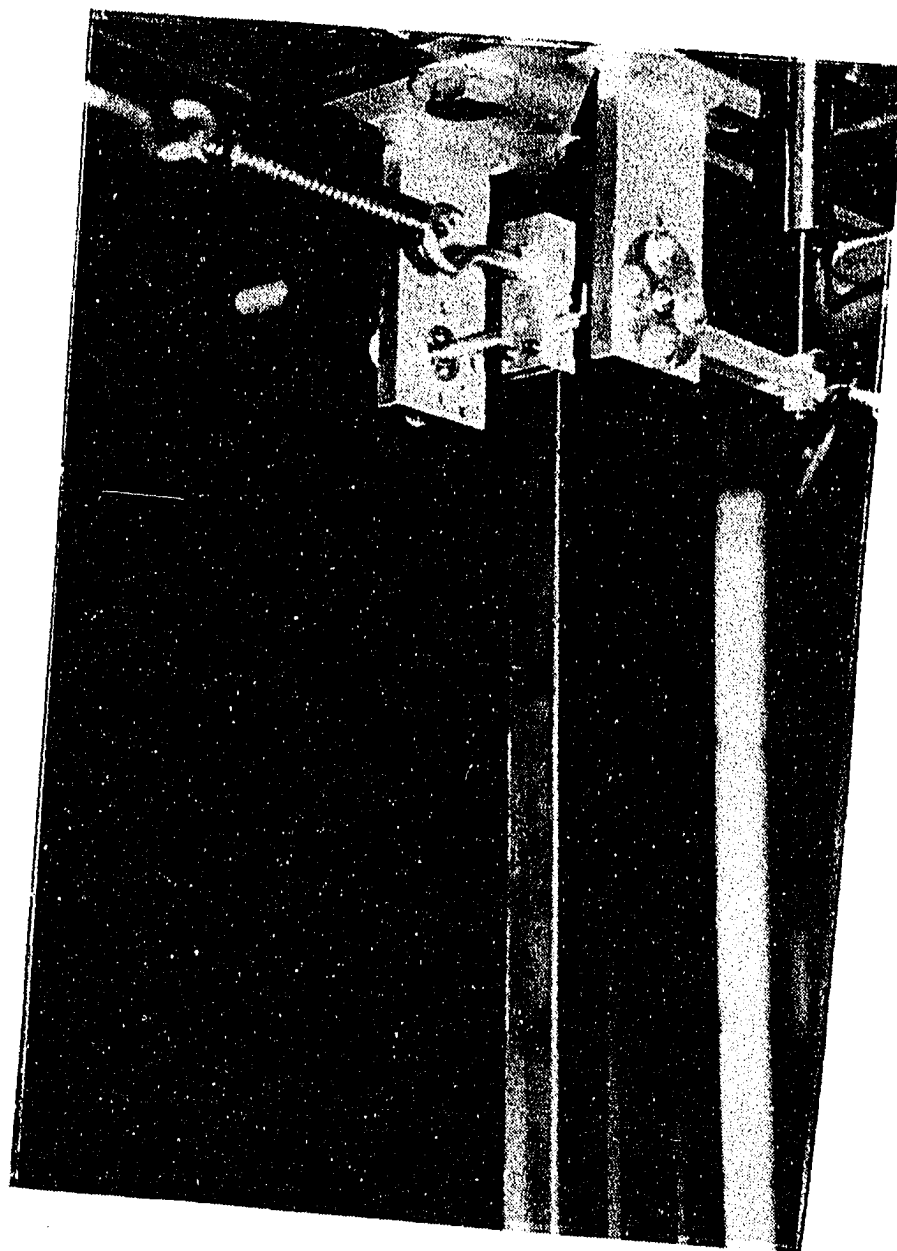


Figure 4.1: Experimental elastic arm apparatus

of the system, the accelerations of some modes are too small to be easily measured. Therefore, the rotational displacement of the mounting shaft is used to measure the response of these modes. As shown in Figures 4.2 and 4.3, a torque arm is clamped to the shaft. The displacement of the end of the arm is measured by a LVDT type displacement transducer. Provided the rotations are small, the displacement of the tip of the torque arm is proportional to the angular rotation of the shaft. While displacement measurement works well for most modes of the system, the displacements of higher modes are too small to be measured with this apparatus. For these modes, the acceleration of the elastic arm is used as the system response. As shown in Figure 4.3, an accelerometer is attached to the arm. The output voltage from the charge amplifier is measured as the system response.

To excite the system, the end of the elastic arm is plucked by hand or struck with a hammer. The resulting displacement or acceleration response is measured and its autospectrum computed with a signal analyzer. The natural frequencies of the system appear as peaks in the autospectrum. Further details of the experimental procedure are presented in Appendix A.

The free vibration technique for determining natural frequencies is used because it eliminates excitation problems encountered with frequency response function measurements. Shaker excitation of the system introduces errors in the experiment, as the arm has such large rotations that the torsional stiffness of the shaker alters the torsional stiffness of the system. Impact excitation does not sufficiently excite the first mode of the system, nor does it have sufficient frequency resolution to accurately determine the natural frequencies.

The instrumentation shown in Figure 4.3 is also used to calibrate the torsional

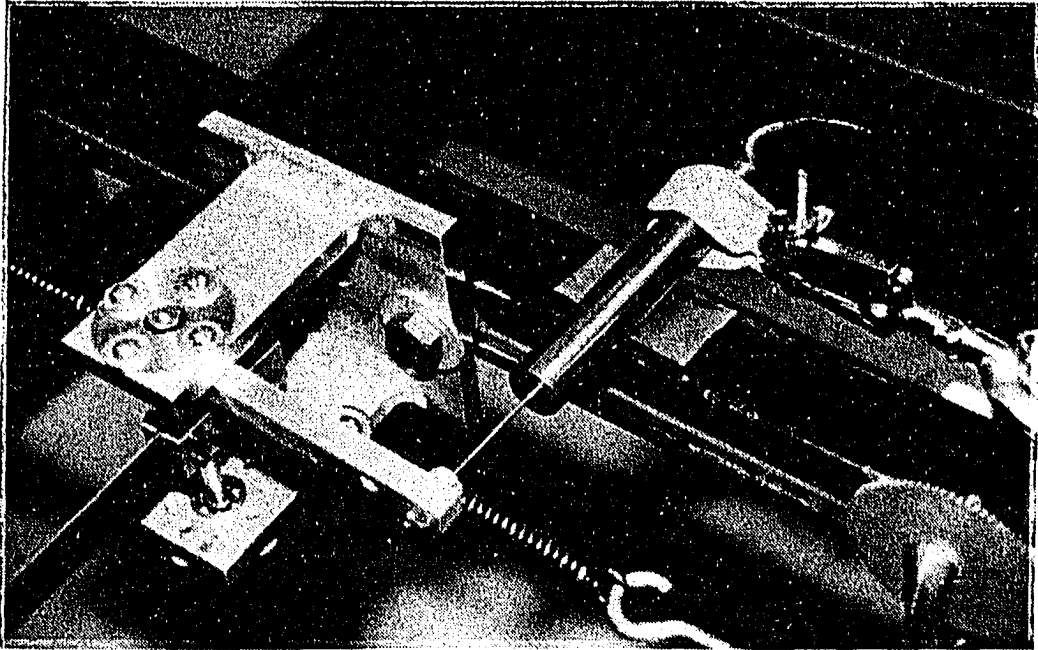


Figure 4.2: Displacement measurement system

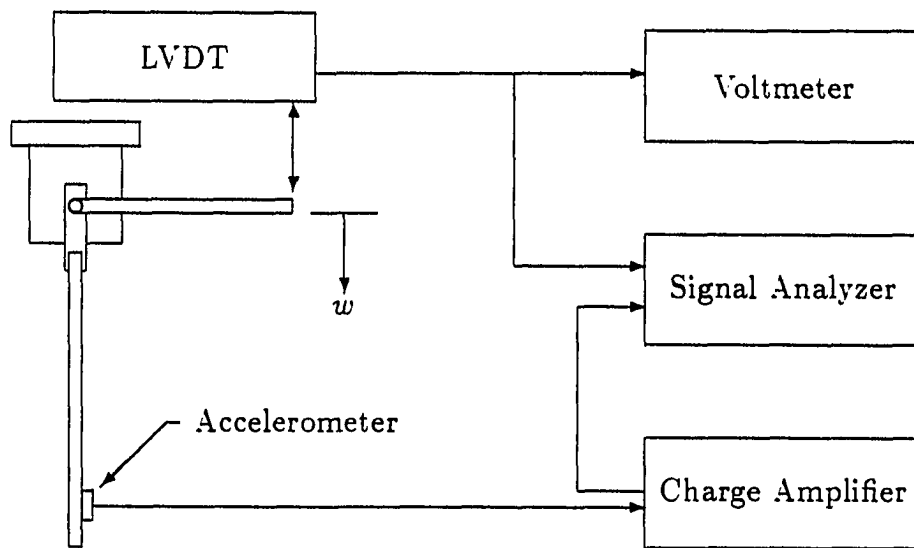


Figure 4.3: Schematic of instrumentation

stiffness of the system. The elastic arm is removed from the system. A known torque is applied to the mounting shaft by attaching weights to the end of the torque arm. The resulting rotation of the shaft is computed from the displacement of the tip of the arm. Knowledge of the applied moment and the resulting rotation allows calculation of the torsional stiffness. Details of this procedure are presented in Appendix A.

4.2 Effect of Mode Shape Selection

This section studies the effect of the assumed mode shape selection upon the accuracy of the assumed modes model. The theoretical criteria for selection of the assumed mode shapes are discussed in Section 3.2.1. These criteria are used to develop alternative assumed mode shapes, which are subsequently used in the model developed in Section 3.2. Conclusions about the accuracy of these alternative models are made by comparison of their natural frequencies to experimental data.

4.2.1 Development of Alternative Assumed Mode Shapes

As discussed in Section 3.2.1, the assumed mode shapes may be divided into three classes; admissible functions, comparison functions, and eigenfunctions. In this section, admissible and comparison functions are derived for this problem using the mode shapes of a cantilever beam and sets of polynomials.

In determining these functions, the boundary conditions are applied to the assumed mode shapes, $\Psi_i(x)$. The boundary conditions are applied by assuming EI is independent of x , and imposing them on the individual mode shapes. Therefore,

the revised geometric boundary conditions are:

$$\Psi_i(0) = 0 \quad (4.1)$$

$$\Psi_i'(0) = 0 \quad (4.2)$$

while the natural boundary conditions reduce to the following equations.

$$\Psi_i''(l) = 0 \quad (4.3)$$

$$\Psi_i'''(l) = 0 \quad (4.4)$$

The normal modes of a cantilever beam are used as approximations to the eigenfunctions of the system. They do not satisfy the partial differential equations, but they satisfy the geometric and natural boundary conditions; qualifying them as comparison functions.

There are many sets of polynomials that can be used as assumed mode shapes. One set of assumed mode shapes for this problem is the following series of monomials.

$$\Psi_i(x) = x^{i+1}; \quad i = 1, 2, 3 \quad (4.5)$$

These assumed mode shapes qualify as admissible functions as they are continuous, complete, linearly independent, and satisfy the geometric boundary conditions. However, they differ from the cantilever mode shapes as they do not satisfy the natural boundary conditions, nor are they orthogonal.

A more complex set of polynomial assumed mode shapes is constructed by imposing both geometric boundary conditions and orthogonality conditions. Consider the following set of polynomials.

$$\Psi_1(x) = c_1 x^2 \quad (4.6)$$

$$\Psi_2(x) = c_2x^2 + d_2x^3 \quad (4.7)$$

$$\Psi_3(x) = c_3x^2 + d_3x^3 + e_3x^4 \quad (4.8)$$

These polynomials are linearly independent and satisfy the geometric boundary conditions of the problem. They are made orthogonal with respect to a unity weighting function by imposing the following equation.

$$\int_0^l \Psi_i \Psi_j dx = 0; \quad i \neq j \quad (4.9)$$

Imposing equation 4.9 upon the assumed polynomials results in the following set of algebraic equations.

$$\frac{c_2}{5} + \frac{d_2l}{6} = 0 \quad (4.10)$$

$$\frac{c_3}{5} + \frac{d_3l}{6} + \frac{e_3l^2}{7} = 0 \quad (4.11)$$

$$\frac{c_2c_3}{5} + \frac{(c_2d_3 + d_2c_3)l}{6} + \frac{(c_2e_3 + d_2d_3)l^2}{7} + \frac{d_2e_3l^3}{8} = 0 \quad (4.12)$$

The six unknown coefficients in equations 4.6, 4.7, and 4.8 are obtained by setting c_1 , c_2 , and c_3 equal to unity, and solving for the remaining three coefficients by use of equations 4.10 to 4.12. The following set of polynomial mode shapes is obtained.

$$\Psi_1(x) = x^2 \quad (4.13)$$

$$\Psi_2(x) = x^2 - \frac{6x^3}{5l} \quad (4.14)$$

$$\Psi_3(x) = x^2 - \frac{14x^3}{5l} + \frac{28x^4}{15l^2} \quad (4.15)$$

Although these polynomials are orthogonal, they do not qualify as comparison functions, as they do not satisfy the natural boundary conditions. In this thesis, they will be referred to as the admissible polynomials.

A set of polynomial comparison functions can be obtained by using the geometric and natural boundary conditions, and the orthogonality condition given in equation 4.9. Due to the increased number of conditions, the order of the polynomials must be higher than those used previously, to provide sufficient unknowns for a nontrivial solution. Consider the following polynomial.

$$\Psi_1(x) = a_1 + b_1x + c_1x^2 + d_1x^3 + e_1x^4 \quad (4.16)$$

The five unknown coefficients in this equation are determined by imposing the geometric and natural boundary conditions, equations 4.1 to 4.4, and by setting c_1 to unity. The following mode shape is obtained.

$$\Psi_1(x) = x^2 - \frac{2x^3}{3l} + \frac{x^4}{6l^2} \quad (4.17)$$

To obtain the second mode shape, assume the following function.

$$\Psi_2(x) = c_2x^2 + d_2x^3 + e_2x^4 + f_2x^5 \quad (4.18)$$

The geometric boundary conditions are already satisfied. To solve for the four unknown coefficients, impose the two natural boundary conditions upon Ψ_2 , the orthogonality condition between Ψ_1 and Ψ_2 , and make c_2 unity. The coefficients d_2 , e_2 , and f_2 are determined from the resulting set of three linear algebraic equations. These equations are presented in Appendix B.

The third mode shape is computed in a similar manner. Start with the following polynomial.

$$\Psi_3(x) = c_3x^2 + d_3x^3 + e_3x^4 + f_3x^5 + g_3x^6 \quad (4.19)$$

The geometric boundary conditions are already satisfied. Let c_3 be unity, impose the two natural boundary conditions, and the two orthogonality conditions. The

Table 4.1: Case 1 parameters

E	$10.11 \times 10^6 \text{ lb-in}^{-2}$	l	39.625 in
A	0.0453 in^2	J_l	$2.77 \times 10^{-4} \text{ lb-in-sec}^2$
ρ	$2.534 \times 10^{-4} \text{ lb-sec}^2\text{-in}^{-4}$	K_t	$0 \rightarrow 300 \text{ in-lb-rad}^{-1}$
I	$1.404 \times 10^{-5} \text{ in}^4$	g	$386.2 \text{ in-sec}^{-2}$

resulting set of linear algebraic equations, shown in Appendix B, is then solved for the unknown coefficients; d_3 , e_3 , f_3 , and g_3 .

4.2.2 Results

To study the effect of mode shape selection, the natural frequencies of the assumed modes model are compared to those of the exact model and experimental data. Gravity is removed from the problem for simplification. In the experiment, gravity is removed from the problem by testing the arm in the horizontal plane. The assumed modes model is used with the four different sets of assumed mode shapes developed in Section 4.2.1. As each set has three assumed mode shapes, each model has four degrees of freedom. The modal integrals in the mass and stiffness matrices are evaluated analytically for the polynomial mode shapes and numerically for the cantilever mode shapes.

The parameters for the arm are listed in Table 4.1. The beam is fabricated from aluminum and its nominal dimensions are $3/4 \times 1/16 \times 40$ inches. The effective length of the beam, l , is shorter than the nominal length since $3/8$ inch of the beam is gripped inside the mounting block.

Figure 4.4 shows that all four sets of assumed mode shapes and the exact solution yield identical first natural frequencies, that agree with the experimental

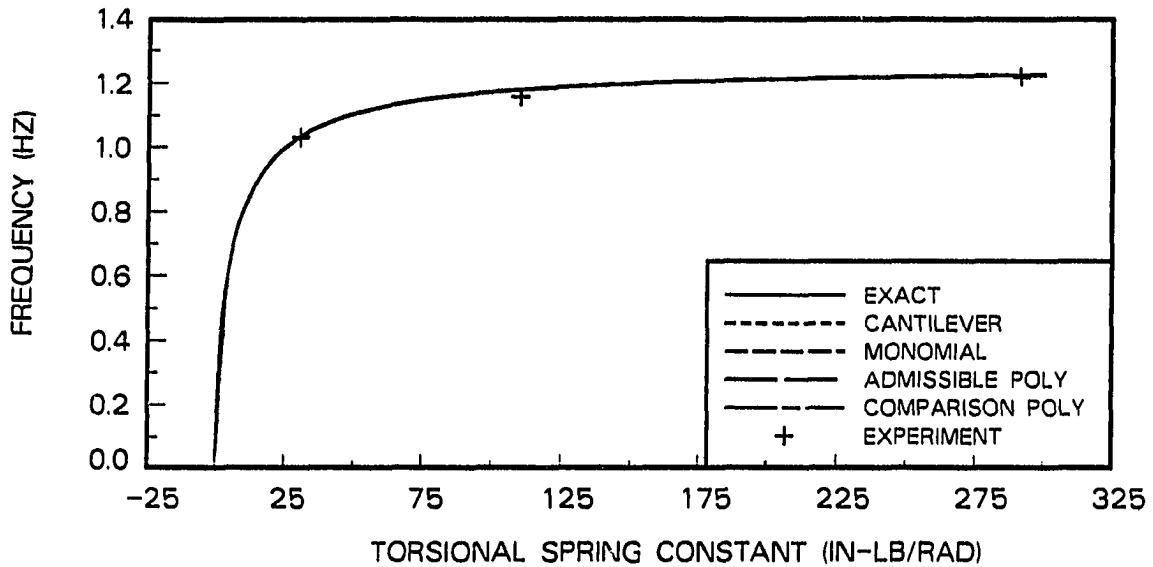


Figure 4.4: Comparison of first natural frequencies from alternative assumed mode shapes; horizontal orientation; case 1

data. However, Figure 4.5 shows significant frequency differences for the second mode. The cantilever and comparison polynomial models agree with the exact solution and best fit the experimental data, while the monomial and admissible polynomial frequencies are higher than the exact solution. Since the admissible polynomials are linear combinations of the monomials, these two models should have identical natural frequencies. The difference in frequencies between them is caused by the lumped inertia of the hub and the torsional spring.

These results are explained by comparing the linear combinations of the assumed mode shapes defined by the eigenvectors of the assumed modes model, to the mode shapes of the exact solution. The linear combination of assumed mode

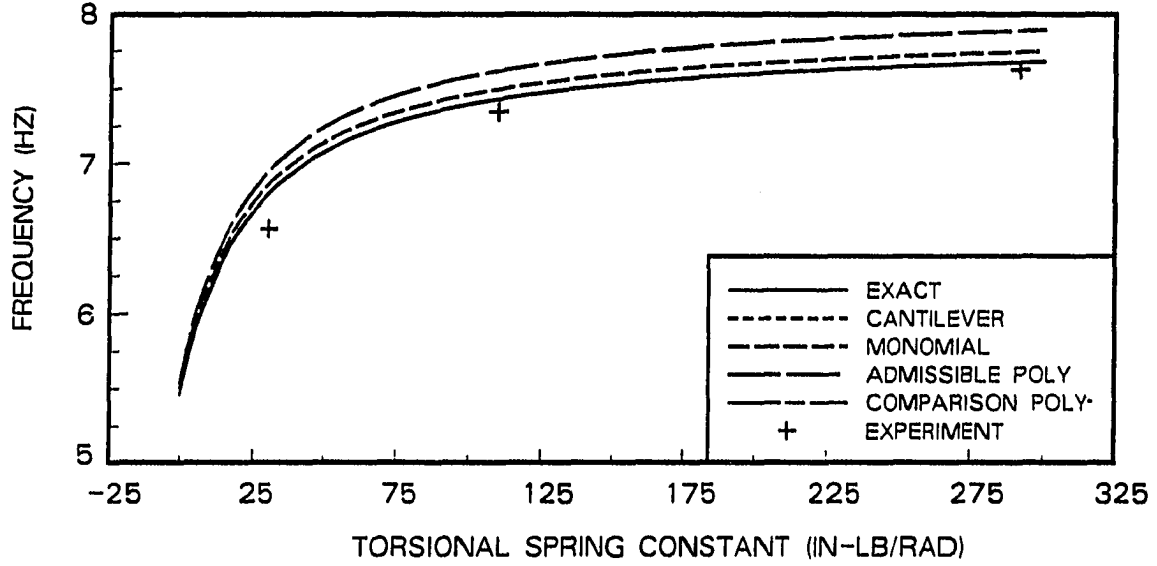


Figure 4.5: Comparison of second natural frequencies from alternative assumed mode shapes; horizontal orientation; case 1

shapes for the i th mode is defined by:

$$X_i(x) = x \tan(u_{1i}) + \sum_{j=1}^3 u_{(j+1)i} \Psi_j(x) \quad (4.20)$$

where u_{ji} is the j th element of the i th eigenvector. Since the first element of the eigenvector, u_{1i} , corresponds to the θ coordinate; the effective mode shape for the first element of the eigenvector is a straight line, as shown in Figure 4.6. The exact mode shape is defined by equation 4.21, to be consistent with equation 4.20.

$$X_i(x) = Y_i(x) + \Theta x \quad (4.21)$$

The mode shapes are normalized by setting u_{1i} and Θ to 0.10, and scaled to match displacements at the end of the arm.

The best set of assumed mode shapes is that set whose linear combinations most accurately model the exact mode shapes of the arm. Figure 4.7 shows that all

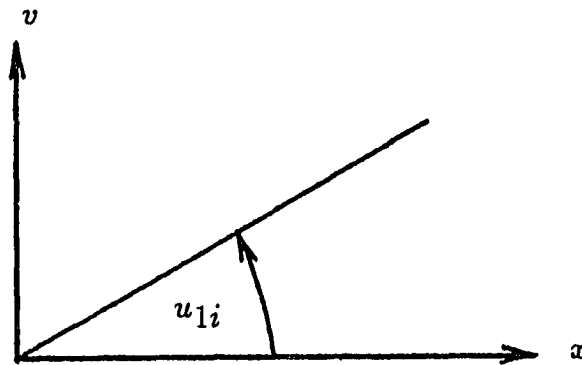


Figure 4.6: Effective mode shape for first element of eigenvector

four sets of assumed mode shapes are good bases for the first mode, when $K_t = 200$ in-lb-rad⁻¹. Therefore, all four should provide accurate natural frequencies. This is exactly the behavior observed in Figure 4.4. For the second mode, Figure 4.8 shows small differences between the linear combinations of mode shapes. The cantilever and comparison mode shapes agree with the exact mode shape, while the monomial and admissible mode shapes differ slightly. This correlates with Figure 4.5, which shows the cantilever and comparison models agreeing with the exact solution while the monomial and admissible models are in error. Comparison of Figures 4.5 and 4.8 also shows the sensitivity of the natural frequencies to the linear combinations of assumed mode shapes.

The cantilever mode shapes and comparison polynomials are the best assumed mode shapes for the elastic arm, as they provide the best bases for the exact mode shapes. Later, when gravity is included, it is necessary to have basis functions

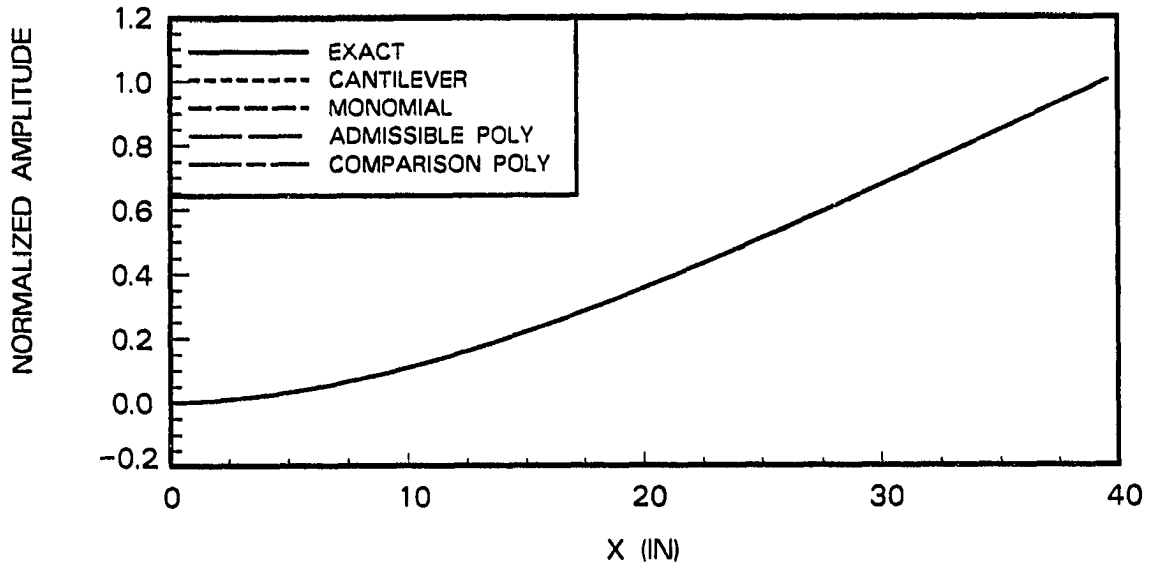


Figure 4.7: Comparison of linear combinations of assumed mode shapes to first exact mode shape; horizontal orientation; $K_t = 200 \text{ in-lb-rad}^{-1}$; case 1

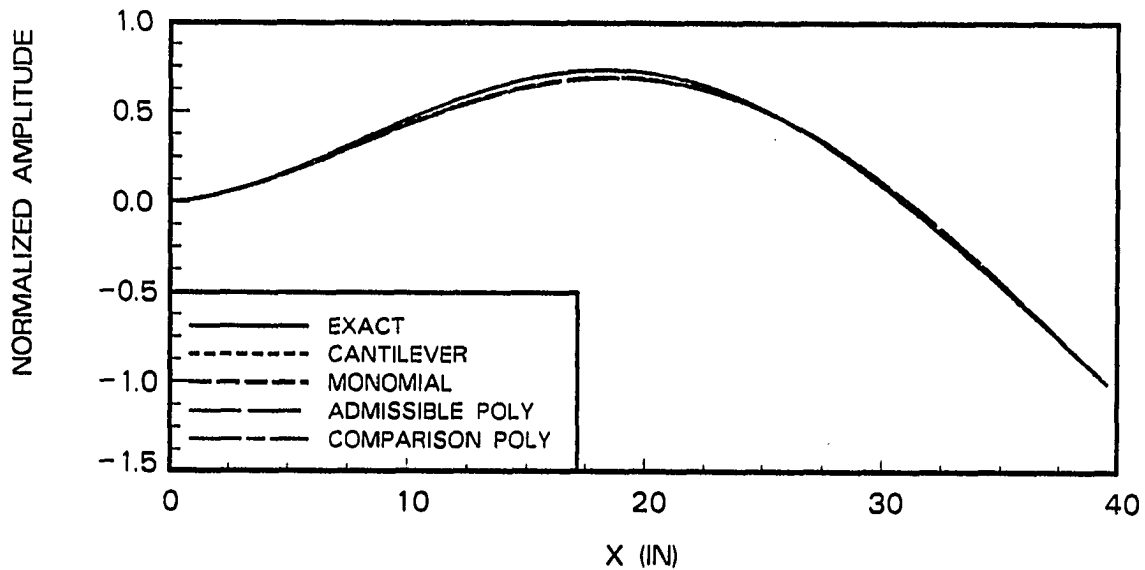


Figure 4.8: Comparison of linear combinations of assumed mode shapes to second exact mode shape; horizontal orientation; $K_t = 200 \text{ in-lb-rad}^{-1}$; case 1

as close to the exact mode shapes, including gravity, as possible. In this case, the superiority of the cantilever mode shapes and comparison polynomials becomes more apparent.

4.3 Coupling of Elastic and Gross Motion

This section examines coupling between elastic and gross motions of the elastic arm. To simplify the problem, gravity is neglected. Figure 4.9 compares the first natural frequency of the exact model, the rigid model developed in Section 3.3, and an uncoupled cantilever model.

The coupling effect between the elastic and gross motions is illustrated by the discrepancy between the rigid model and the exact solution in Figure 4.9. At low values of K_t , the two models agree since the frequencies of the elastic and rigid motions are sufficiently separated. As the torsional spring becomes increasingly stiff, the rigid body frequency increases. When this frequency nears the frequency of the elastic motion, the motions couple and produce modes having both motions. For large values of K_t , the rigid motion becomes very small compared to the elastic motion and the modes become dominated by the elastic motion. As expected, Figure 4.9 shows that the natural frequency of the coupled model approaches the cantilever beam frequency as K_t increases.

In order to predict the coupling effects, the error between the rigid model and the exact solution is plotted versus the ratio of the rigid frequency to the uncoupled cantilever frequency. This error is the frequency shift from the rigid model due to elastic coupling, and correlates to the amount of elastic motion relative to rigid motion. The frequency shift is plotted for three significantly different arms; case

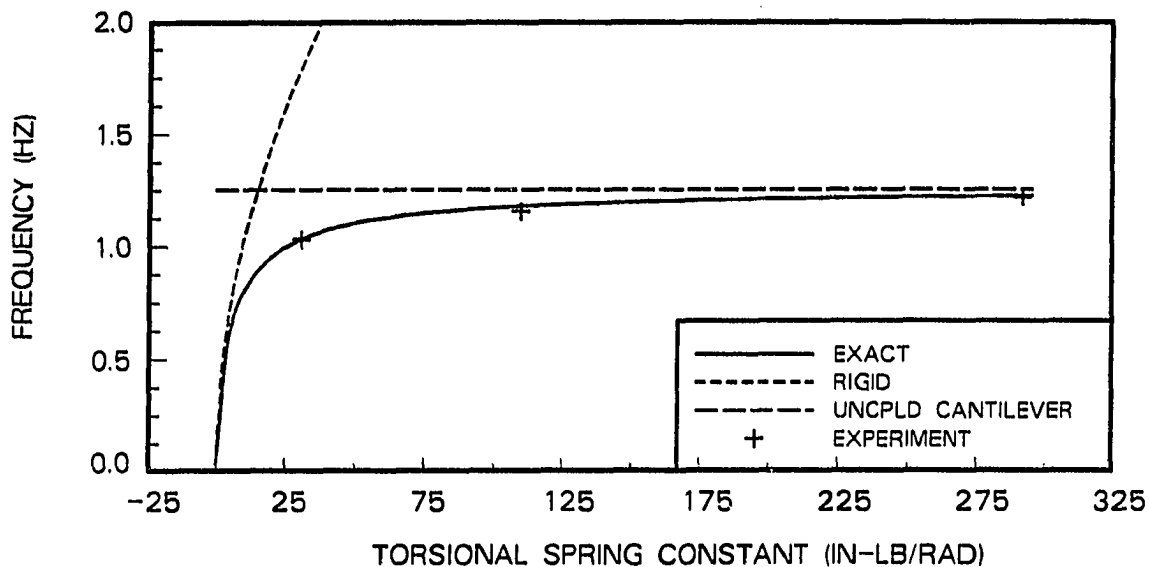


Figure 4.9: Comparison of first natural frequencies of coupled and uncoupled models; horizontal orientation; case 1

Table 4.2: Case 2 parameters

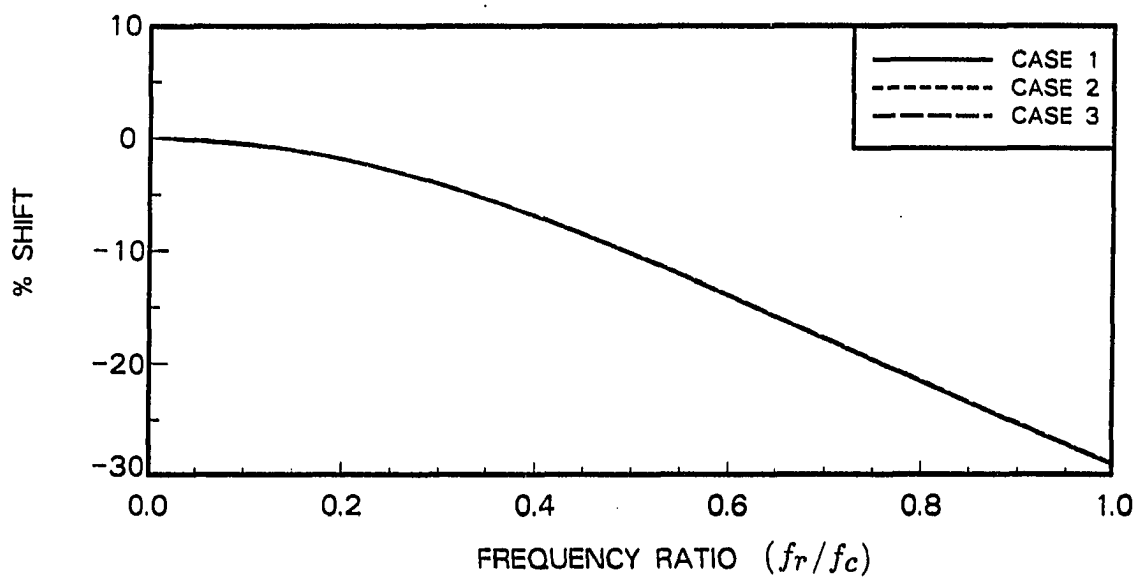
E	$29.27 \times 10^6 \text{ lb-in}^{-2}$	l	29.625 in
A	0.0488 in^2	J_l	$2.77 \times 10^{-4} \text{ lb-in-sec}^2$
ρ	$7.290 \times 10^{-4} \text{ lb-sec}^2\text{-in}^{-4}$	I	$1.716 \times 10^{-5} \text{ in}^4$

1 is a $3/4 \times 1/16 \times 40$ inch aluminum arm, case 2 is a $3/4 \times 1/16 \times 30$ inch steel arm, and case 3 is a $3/4 \times 1/16 \times 20$ inch aluminum arm. The parameters for these three cases are listed in Tables 4.1 to 4.3. Figure 4.10 shows the shifts for the three different arms are virtually identical. This indicates that this plot provides a simple means of predicting the frequency shifts produced by elastic coupling. Computing cantilever and rigid frequencies for an arm is simple, and Figure 4.10 can be used to predict the true first frequency from these simple calculations.

This plot is relevant to conventional robot arms. A conventional robot arm is

Table 4.3: Case 3 parameters

E	$9.76 \times 10^6 \text{ lb-in}^{-2}$	l	19.625 in
A	0.0483 in^2	J_l	$2.77 \times 10^{-4} \text{ lb-in-sec}^2$
ρ	$2.503 \times 10^{-4} \text{ lb-sec}^2\text{-in}^{-4}$	I	$1.596 \times 10^{-5} \text{ in}^4$

Figure 4.10: Frequency shift from rigid model as function of (f_r/f_c)

stiff and massive, and has high torsional stiffnesses at its joints, due to the control actuators. This combination makes the first cantilever frequency much higher than the frequency of the rigid model. Therefore, it has a small frequency ratio, placing it near the origin of Figure 4.10. Use of a rigid model is reasonable in this region. However, the trend in robots is towards lighter, faster, more elastic arms. This trend will increase the rigid frequency, but decrease the first cantilever frequency; moving new robot designs away from the origin of Figure 4.10. In this region, the rigid and elastic motions will couple, causing significant elastic motion and shifting the first natural frequency. Figure 4.10 can aid in the design of elastic robots by predicting these frequency shifts from the rigid model.

4.4 Effect of Gravity

This section investigates the elastic arm in a vertical position, where gravity has significant effects on the accuracy of the model. To illustrate this, Figure 4.11 compares the first natural frequencies of the exact and coupled cantilever models to experimental data. As shown in this figure and Table 4.4, the analytical frequencies are generally lower than the experimental frequencies, and the percentage error increases with K_t . The analytical models are more accurate in predicting the second natural frequencies of the system, as shown in Figure 4.12. They predict the second natural frequency to within 3.5% of the experimental results, and the error does not increase with K_t , as is the case for the first mode.

The large errors observed in the predictions of the first natural frequency are due to gravity. These errors are not present in Figure 4.4, which presents the same models in the absence of gravity. The effect is also illustrated by considering shorter,

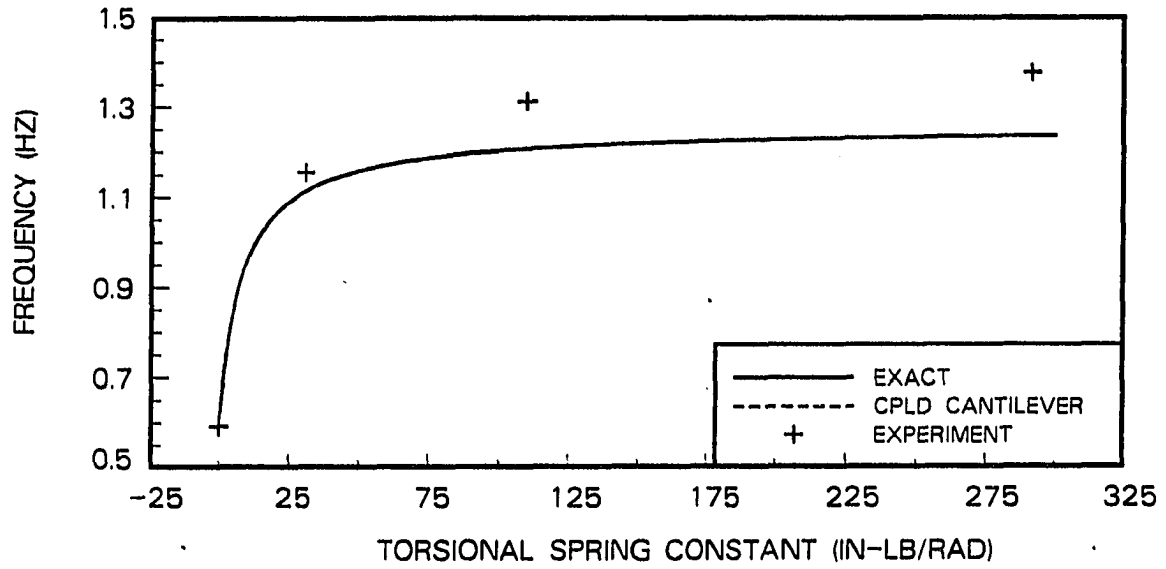


Figure 4.11: First natural frequency of coupled models in presence of gravity; case 1

Table 4.4: Errors in first natural frequency of exact and coupled cantilever models in presence of gravity; case 1

K_t (in-lb-rad ⁻¹)	f_1^{exp} (Hz)	f_1^{ana} (Hz)	% error in f_1^{ana}
0	0.593	0.607	2.43
31.18	1.156	1.116	-3.46
105.5	1.312	1.205	-8.16
291.5	1.375	1.235	-10.2

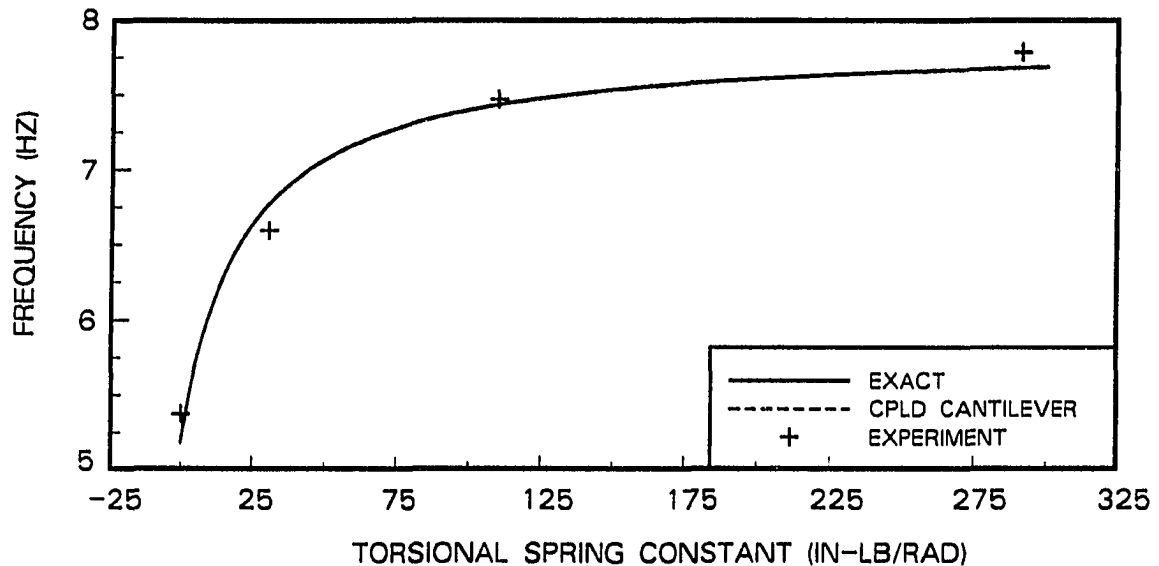


Figure 4.12: Second natural frequency of coupled model in presence of gravity; case 1

stiffer beams, which are less affected by gravity. While case 1 is a $3/4 \times 1/16 \times 40$ inch aluminum beam, case 2 is a $3/4 \times 1/16 \times 30$ inch steel beam, and case 3 is an $3/4 \times 1/16 \times 20$ inch aluminum beam. The parameters for these later two cases are shown in Tables 4.2 and 4.3. As shown in Figure 4.13, the first mode of the exact model is more accurate for shorter, stiffer beams.

The failure of the exact and coupled cantilever models to properly model gravity is caused by neglecting the vertical displacement of the beam due to transverse deflections. As shown in Figure 4.14, transverse deflection of the beam causes a vertical displacement, h . This displacement is caused by curvature of the beam, not axial deformations. If the beam is oriented vertically, this displacement increases the potential energy of the system, thereby increasing its natural frequencies. Since neither model accounts for the vertical displacement, their natural frequencies should

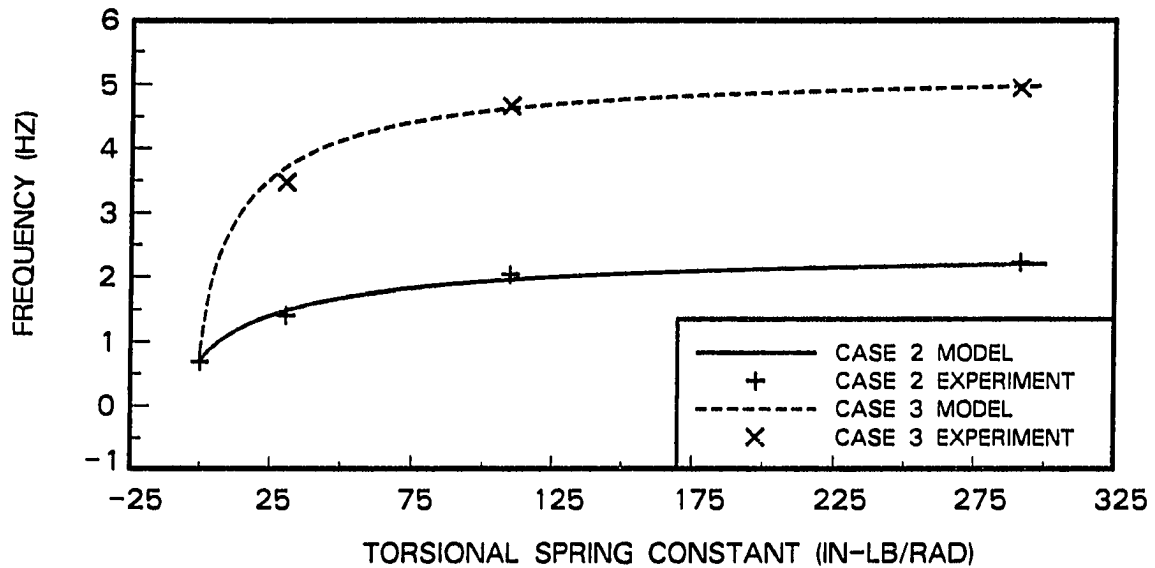


Figure 4.13: First natural frequency of the exact model in presence of gravity; case 2 ($3/4 \times 1/16 \times 30$ inch steel beam); case 3 ($3/4 \times 1/16 \times 20$ inch aluminum beam)

be lower than the experimentally measured frequencies when gravity is present; but correct when gravity is absent. This is exactly the behavior observed in the first mode of case 1. The second mode does not display this behavior because its elastic potential energy is much larger than that of the first mode. Therefore, the error due to neglecting the vertical displacement is negligible. For the same reason, the first modes of cases 2 and 3 do not display the frequency error. The arms are so stiff that their elastic potential energies are much larger than the error due to the vertical displacement.

4.4.1 Correction Term for Gravity

An estimate of the error caused by neglecting the vertical displacement due to transverse deflections is first derived for a cantilever beam model. Consider the

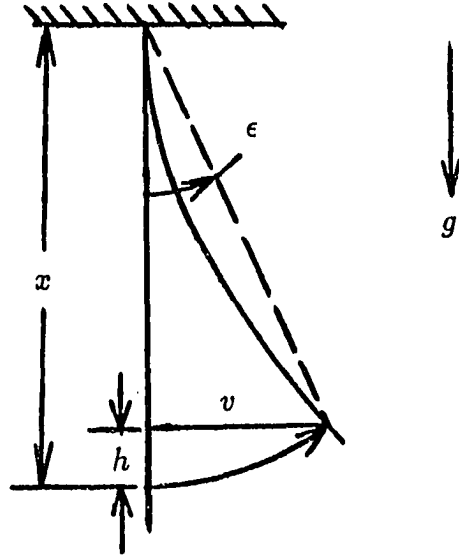


Figure 4.14: Cantilever beam model

cantilever beam shown in Figure 4.14. The transverse and vertical deflections of a point are denoted by v and h , respectively. Assume the axial deformations are negligible. The Rayleigh method is used to estimate the first natural frequency of this system, including the effect of gravity. The error due to neglecting the vertical displacement is calculated by comparing this natural frequency to the frequency of a gravity free cantilever beam.

The kinetic energy of the beam is expressed in terms of the transverse deflection.

$$T = \int \frac{\dot{v}^2}{2} dm \quad (4.22)$$

Assume $v(x, t)$ is harmonic and may be expressed in terms of an assumed mode shape, $\Psi(x)$.

$$v(x, t) = \Psi(x) \sin(\omega t - \phi) \quad (4.23)$$

With this substitution, the kinetic energy simplifies to the following equation.

$$T = \frac{\rho A \omega^2}{2} \int_0^l \Psi^2 dx \cos^2(\omega t - \phi) \quad (4.24)$$

The potential energy has both elastic and gravitational components.

$$\Pi = \int_0^l \frac{EI}{2} (v'')^2 dx + \int hg dm \quad (4.25)$$

To evaluate the above expression, $h(x)$ can be obtained from the arc length of $v(x)$.

$$h(x) = \int_0^x \sqrt{1 + (v')^2} dx - x \quad (4.26)$$

For an assumed deflection, $v(x)$, the vertical displacement can be evaluated from the previous equation. However, the arc length integral is intractable for all but the most elementary functions for $v(x)$.

An approximation for $h(x)$ can be obtained from an equivalent arc length [53], as shown in Figure 4.14. This approximation is only valid for the first mode. The vertical displacement may be expressed in terms of ϵ , provided ϵ is small.

$$h \approx x(1 - \cos \epsilon) \approx x \left(1 - 1 + \frac{\epsilon^2}{2} \right) \approx \frac{x\epsilon^2}{2} \quad (4.27)$$

However, ϵ can be expressed in terms of the transverse displacement.

$$\epsilon \approx \frac{v}{x} \quad (4.28)$$

Substitution of equation 4.28 into equation 4.27 yields the final expression for h .

$$h \approx \frac{v^2}{2x} \quad (4.29)$$

The accuracy of this approximation is investigated by a comparison of $h(x)$ calculated from equations 4.26 and 4.29 for the static deflection curve of a uniformly

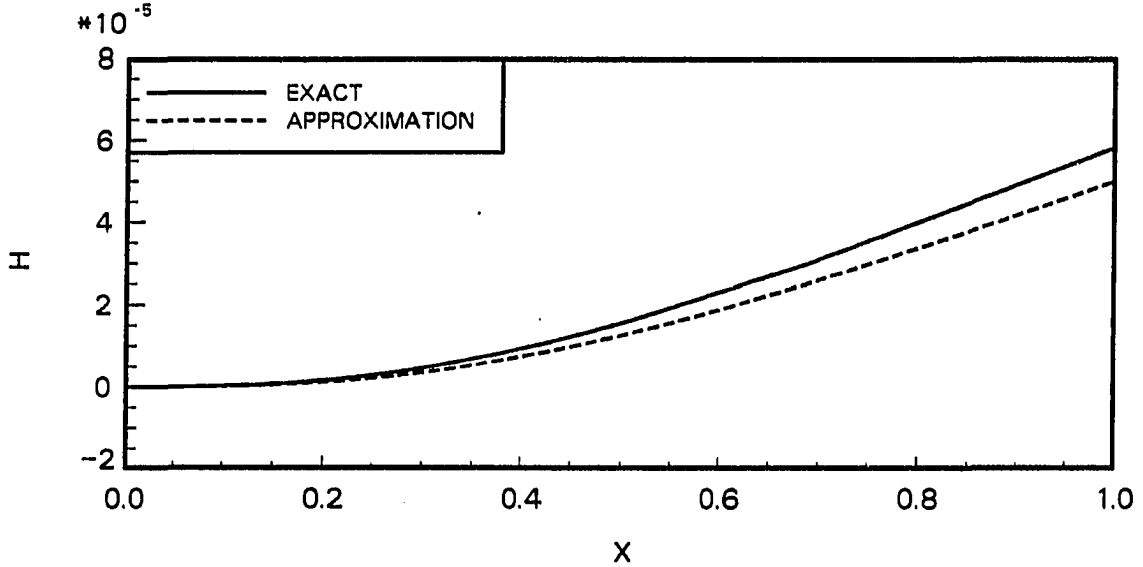


Figure 4.15: Comparison of exact and approximate vertical displacements.
 $v_{\max} = 0.01$

loaded cantilever beam.

$$v = v_{\max} \left(\frac{4lx^3 - x^4 - 6l^2x^2}{3l^4} \right) \quad (4.30)$$

Equation 4.26 is the exact solution and is evaluated numerically, while equation 4.29 is the approximation. As shown in Figure 4.15, equation 4.29 only approximates the true value of $h(x)$. However, its use allows the effect of gravity upon the first natural frequency to be developed in a closed form equation.

To incorporate the approximate $h(x)$ into the potential energy, substitute equation 4.29 into equation 4.25 and let $dm = \rho A dx$. Then, the potential energy expression simplifies to the following equation.

$$\Pi = \left[\frac{EI}{2} \int_0^l (\Psi'')^2 dx + \frac{\rho Ag}{2} \int_0^l \frac{\Psi^2}{x} dx \right] \sin^2(\omega t - \phi) \quad (4.31)$$

To apply the Rayleigh Principle, equate T_{\max} and Π_{\max} , the maximum values

of equation 4.24 and equation 4.31, respectively.

$$\frac{\omega^2 \rho A}{2} \int_0^l \Psi^2 dx = \frac{EI}{2} \int_0^l (\Psi'')^2 dx + \frac{\rho Ag}{2} \int_0^l \frac{\Psi^2}{x} dx \quad (4.32)$$

To evaluate the integrals in equation 4.32, let $\Psi(x)$ be the static deflection curve for a uniformly loaded cantilever beam, equation 4.30. With this substitution, equation 4.32 simplifies to the following equation.

$$\frac{52\omega^2 \rho Al}{405} = \frac{8EI}{5l^3} + \frac{2561\rho Ag}{15120} \quad (4.33)$$

Solve equation 4.33 for ω^2 .

$$\omega^2 = \left(\frac{3.530}{l^2}\right)^2 \left(\frac{EI}{\rho A}\right) + \frac{1.319g}{l} \quad (4.34)$$

If $g = 0$, equation 4.34 estimates the natural frequency for the case without gravity, ω_{ng} .

$$\omega_{ng} = \frac{3.530}{l^2} \sqrt{\frac{EI}{\rho A}} \quad (4.35)$$

This estimate is only 0.4% in error with respect to the the exact natural frequency. Substitute equation 4.35 into equation 4.34 and rearrange the resulting equation to obtain a ratio of the gravity affected frequency, f , to the gravity free frequency, f_{ng} .

$$\frac{f}{f_{ng}} = \sqrt{1 + \frac{g}{29.93lf_{ng}^2}} \quad (4.36)$$

Equation 4.36 predicts the error in the first natural frequency of a cantilever beam resulting from neglect of the vertical displacement.

The validity of this model was tested by comparing its frequency predictions against experimentally obtained natural frequencies for a cantilever beam. A beam was clamped in the mounting block used for the elastic arm. In turn, the mounting

block was rigidly clamped to a structure. The end of the beam was plucked and the acceleration response of the beam measured by the system shown in Figure 4.3. The first two natural frequencies were determined from the peaks in the autospectrum of the acceleration response. To obtain the natural frequencies with and without the effect of gravity, the experiment was conducted in both the vertical and horizontal orientations.

Table 4.5 compares the change in the first natural frequency, due to gravity, predicted by equation 4.36 to experimental data. Case 1 is a 3/4 x 1/16 x 40 inch aluminum beam, case 2 is a 3/4 x 1/16 x 30 inch steel beam, and case 3 is a 3/4 X 1/16 X 20 inch aluminum beam. The first frequency is significantly increased by gravity for case 1, but cases 2 and 3 are affected less significantly. This behavior can be explained by equation 4.36. The gravity free natural frequency, f_{ng} , increases rapidly as the beam length is decreased. Therefore, shorter beams are less affected by gravity. This is illustrated by Figure 4.16; which presents the percentage change in the first frequency, due to gravity, for the analytical model and the experimental data. The effect of gravity is only noticeable for very long, highly elastic beams. Table 4.6 presents the experimental data for the second natural frequency of the beam. The second mode is not significantly affected by gravity. Although gravity can change the first natural frequency of a cantilever beam, the model developed in this section can estimate the change.

The vertical displacement effect is easily incorporated into the assumed modes model by use of the approximate expression for $h(x)$, equation 4.29. If the exact expression for $h(x)$ was used, it would have to be evaluated for the linear combination of assumed mode shapes, $v' = \bar{D}^T \bar{\Psi}'$. The complexity of the assumed mode

Table 4.5: Effect of gravity on first natural frequency of cantilever beam

Case	Experimental f_1 (Hz)		% change due to g	
	No g	With g	Experiment	Model
1	1.218	1.375	12.9	10.4
2	2.343	2.468	5.34	3.89
3	4.906	4.937	0.63	1.36

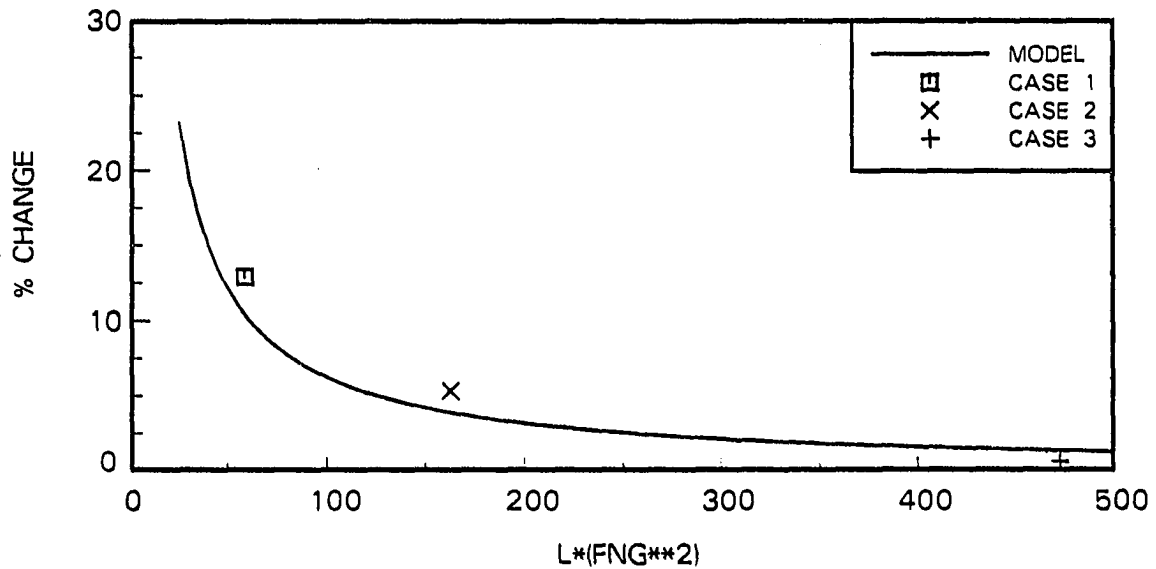


Figure 4.16: Change in first natural frequency of cantilever beam due to gravity

Table 4.6: Effect of gravity on second natural frequency of cantilever beam

Case	Experimental f_2 (Hz)		% change due to g	
	No g	With g	Experiment	Model
1	7.687	7.843	2.03	0.0
2	14.656	14.718	0.42	0.0
3	31.156	31.125	-0.1	0.0

shapes makes this integral intractable. Since the approximation for $h(x)$ estimated the effect of gravity upon the first natural frequency of a cantilever beam, it is also applicable to the elastic arm. Furthermore, the approximation can be easily incorporated into the assumed modes model.

The potential energy associated with the vertical displacement is given by the following equation:

$$\Pi_d = \int hg \cos \theta dm \quad (4.37)$$

where the $\cos \theta$ term is introduced since the elastic arm can rotate about its base. Since the displacement due to the transverse deflection is along the axis of the arm, its vertical component is obtained by multiplying by $\cos \theta$. Use equation 4.29 to express h in terms of the transverse displacement. In addition, let $dm = \rho A dx$. With these substitutions, equation 4.37 simplifies to the following equation.

$$\Pi_d = \int_0^l \frac{\rho A g v^2}{2x} \cos \theta dx \quad (4.38)$$

The transverse displacement is expressed in terms of the deformation coordinates and the assumed mode shapes.

$$v = \bar{D}^T \bar{\Gamma} \quad (4.39)$$

where $\bar{\Gamma}$ is an assumed mode shape vector that uses only the first mode.

$$\bar{\Gamma} = \{ \Psi_1 \ 0 \ 0 \ } \quad (4.40)$$

The second and third mode shapes are equated to zero, as the gravity correction term is only valid for the first mode of the arm. Substitution of equation 4.39 into equation 4.38 and use of a transformation similar to that shown in equation 3.60

yields the final potential energy expression:

$$\Pi_d = \bar{D}^T \int_0^l \frac{\rho A g \bar{\Gamma}}{2x} \cos \theta dx \bar{D} \quad (4.41)$$

where

$$\bar{\Gamma} = \bar{\Gamma} \bar{\Gamma}^T \quad (4.42)$$

The potential energy expression is differentiated with respect to the coordinate vector, \bar{q} , linearized about the operating point $\bar{q} = \bar{0}$, and the new terms incorporated into the linearized stiffness matrix, equation 3.77. The revised stiffness matrix reduces to the following form.

$$\bar{K} = \begin{bmatrix} K_t + \int_0^l \rho A g x dx & \int_0^l \rho A g \bar{\Psi}^T dx \\ \int_0^l \rho A g \bar{\Psi} dx & \int_0^l EI \bar{\Upsilon} dx + \int_0^l \frac{\rho A g \bar{\Gamma}}{x} dx \end{bmatrix} \quad (4.43)$$

The revised assumed modes model is significantly more accurate than the original model. Figures 4.17 and 4.18 compare the revised model and the experimental data for the vertical orientation. Comparison of these graphs to Figures 4.11 and 4.12 shows the revised model to be more accurate than the original model for the first mode, and as accurate for the second mode.

4.4.2 Effect of Gravity on Mode Shape Selection

The addition of gravity and the gravity correction term makes the selection of the assumed mode shapes more critical. Figures 4.19 and 4.20 compare the first and second natural frequencies of the exact and assumed modes models in the presence of gravity. The gravity correction term is included in the assumed modes models, but is not incorporated into the exact model. Figure 4.19 shows the cantilever,

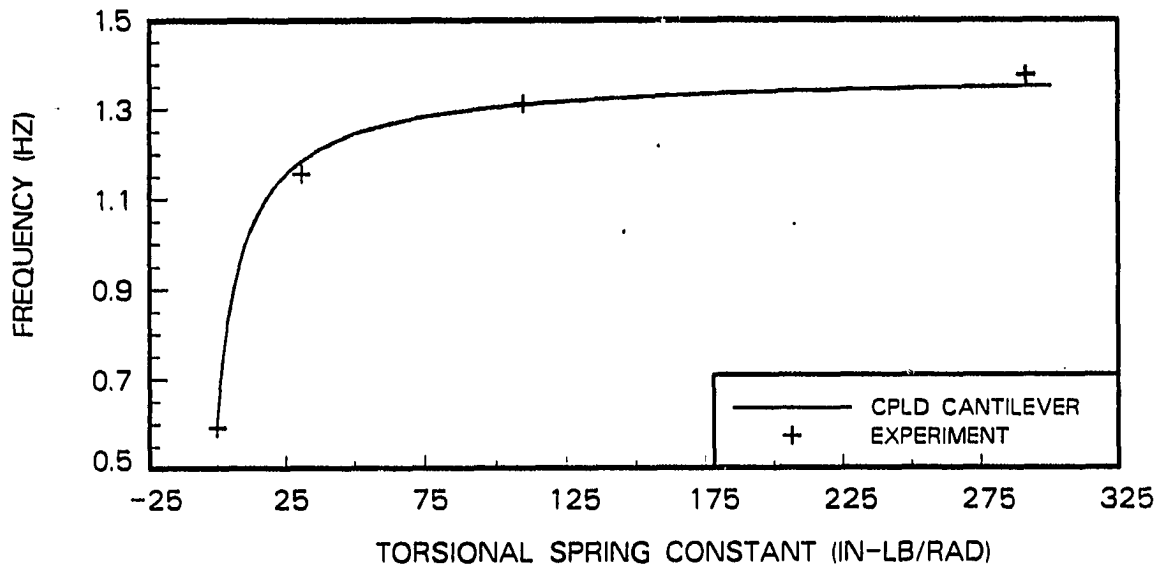


Figure 4.17: First natural frequency of revised assumed modes model in presence of gravity; case 1

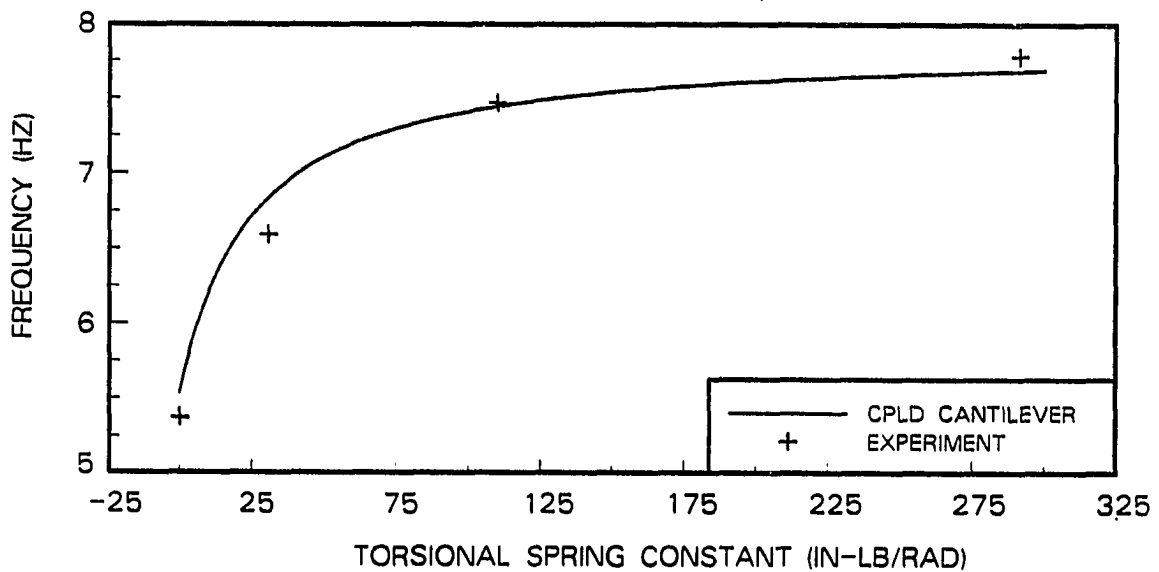


Figure 4.18: Second natural frequency of revised assumed modes model in presence of gravity; case 1

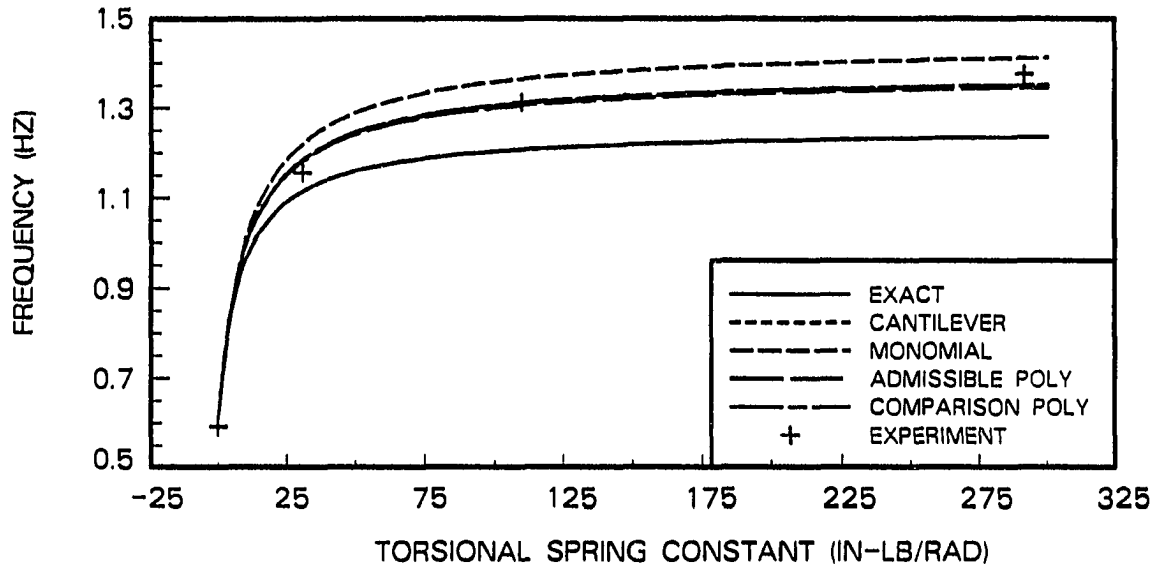


Figure 4.19: Comparison of first natural frequencies from alternative assumed mode shapes; vertical orientation; revised model; case 1

admissible, and comparison models agree well with the experimental data, but the exact and monomial models do not. For the second natural frequency, Figure 4.20 shows the exact, cantilever, and comparison models agree with the experimental results. The admissible model is slightly less accurate, while the monomial model is significantly in error. The error in the first mode of the exact model is caused by its neglect of the vertical displacement effect. Comparison of Figures 4.5 and 4.20 shows that gravity has significantly reduced the accuracy of the second mode of the monomial model, but has not affected the accuracy of the cantilever and comparison polynomial models.

These results are explained by comparison of the linear combinations of the assumed mode shapes defined by the eigenvectors of the assumed modes models. Figures 4.21 and 4.22 show that the monomial coupled system mode shapes differ

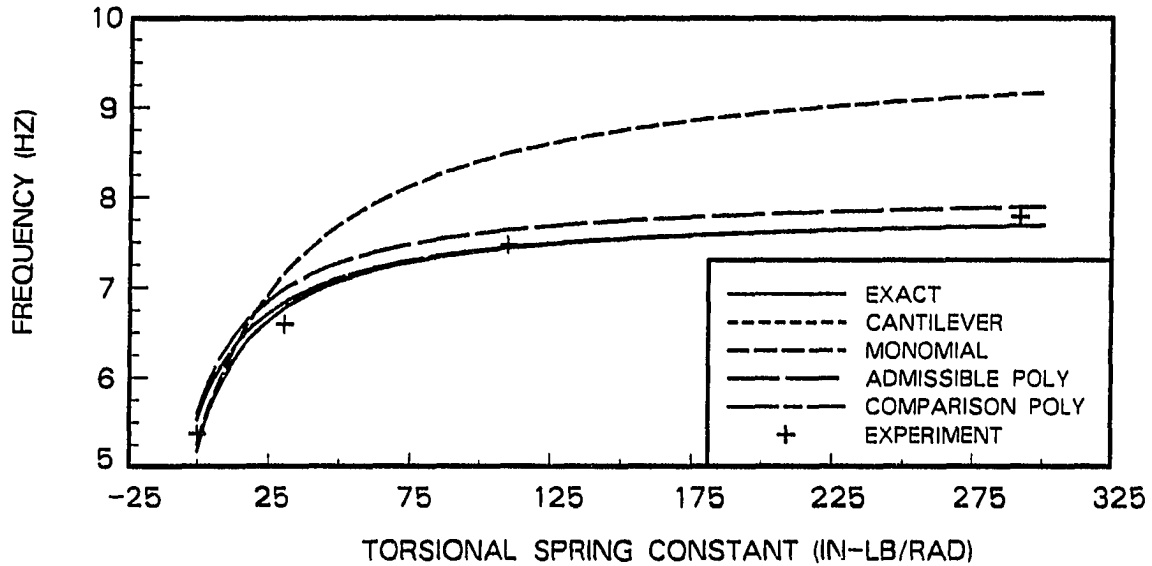


Figure 4.20: Comparison of second natural frequencies from alternative assumed mode shapes; vertical orientation; revised model; case 1

significantly from the other mode shapes, especially for the second mode. These figures show that, in the presence of gravity, the monomial assumed mode shapes are poor basis functions for the elastic arm. Therefore, the monomial model does not accurately predict the frequencies of the system.

4.5 Conclusions

Several conclusions may be drawn from this chapter. First, the selection of assumed mode shapes is important, especially in the presence of gravity. The cantilever mode shapes and comparison polynomials are the most accurate assumed mode shapes, for both the gravity free and gravity cases. However, their accuracy advantage over the monomials and the admissible polynomials is small in the absence of gravity, especially for the first mode. When gravity is included in the

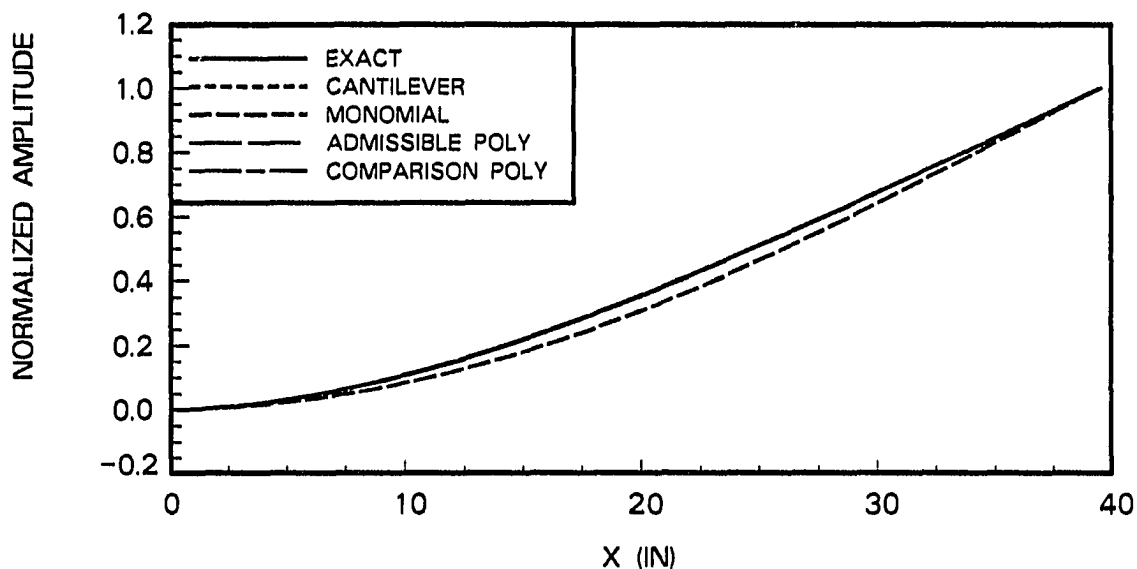


Figure 4.21: Comparison of linear combinations of assumed mode shapes to first exact mode shape; vertical orientation; $K_t = 200 \text{ in-lb-rad}^{-1}$; revised model; case 1

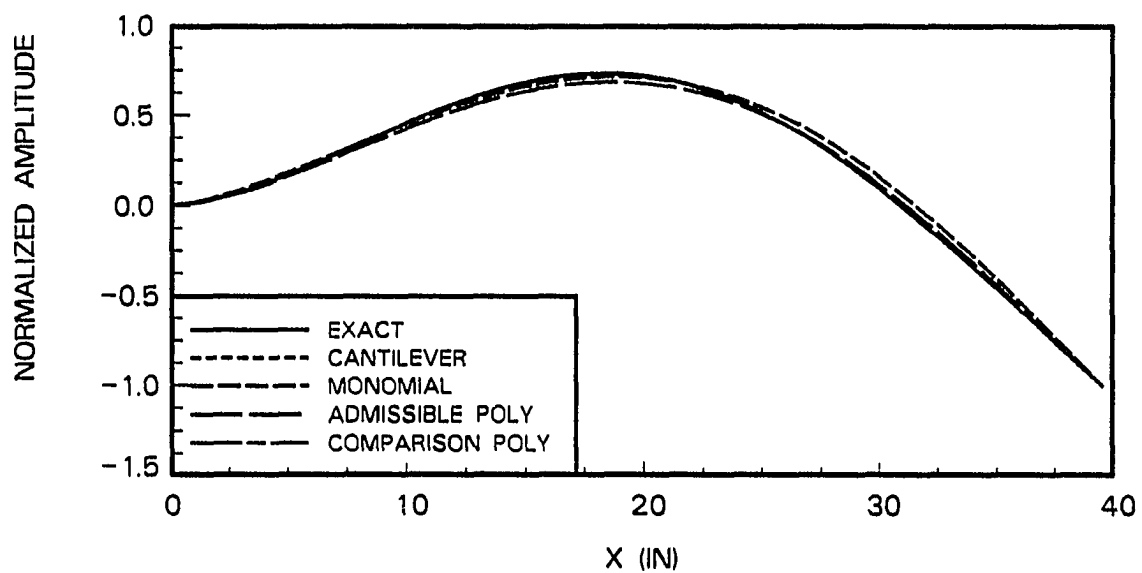


Figure 4.22: Comparison of linear combinations of assumed mode shapes to second exact mode shape; vertical orientation; $K_t = 200 \text{ in-lb-rad}^{-1}$; revised model; case 1

problem, the accuracy advantage of the cantilever and comparison polynomials becomes significant, especially over the monomials. The best assumed mode shapes for the elastic arm are the comparison polynomials. They are accurate, even in the presence of gravity, but they do not require numerical integration to evaluate the modal integrals. Therefore, they require significantly less computing time than the equally accurate cantilever mode shapes.

Second, a simple but effective plot has been developed to show the effect of elastic coupling upon the first natural frequency of robot arms. Elasticity in robot arms can cause significant frequency shifts from a rigid model. These frequency shifts are due to the coupling between the elastic and gross motions. However, the magnitude of these frequency shifts is easily predicted by the use of Figure 4.10 and the ratio of the rigid frequency of the arm to the first cantilever frequency of the arm.

Third, gravity can significantly affect the first natural frequency of the elastic arm. Accurate modeling of the effect of gravity requires that the vertical displacement due to transverse deflections be included. A simple model based upon a cantilever beam was developed to allow prediction of the error caused by neglect of the vertical displacement. This simple model, incorporated into the assumed modes model as a gravity correction term, greatly reduces the error in the first natural frequency due to gravity. Although the gravity effect only appears significant for unrealistically elastic arms, the next chapter will show how an end mass extends this effect to more realistic designs.

5 EFFECT OF END MASS

The previous chapters of this thesis have studied an elastic robot arm with a free end. However, the purpose of a robot is to carry an end effector and payload at the end of the arm. The effect of this end mass can be important for an elastic arm, since the arm is light and the end mass can be a significant percentage of the mass of the arm. This chapter examines the effect of adding a mass to the end of an elastic robot arm. In addition, this work models the mass moment of inertia of the end mass, unlike several previous studies of elastic robot arms [43,46,48].

The next three sections of this chapter modify the models developed in Chapter 3 to include an end mass. The following sections examine the effects of mode shape selection, coupling of gross and elastic motion, and gravity.

5.1 Derivation of Exact Model

The exact model of the elastic arm, developed in Section 3.1, is easily extended to include an end mass. As shown in Figure 5.1, a rigid mass is attached to the tip of the elastic arm. Denote its mass by m_a , and its mass moment of inertia about its center of mass by J_a . Also, assume the center of mass of the end mass is located at the end of the arm.

The kinetic energy expression for the arm developed in Section 3.1, equa-

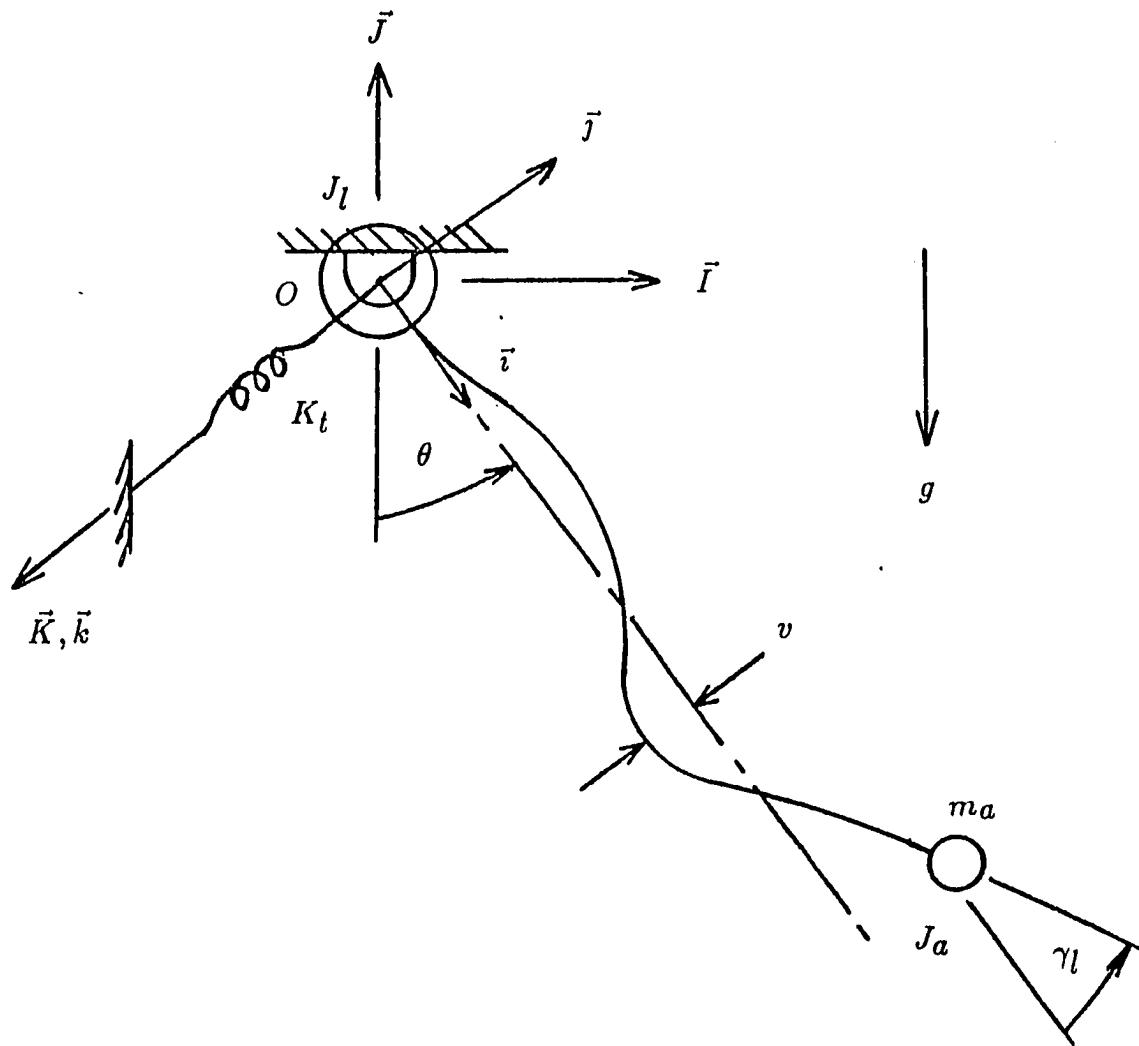


Figure 5.1: Elastic arm with end mass

tion 3.10, is still applicable, with the addition of end mass terms. The kinetic energy of the end mass is given by equation 5.1, in which $\bar{\mu}$ denotes the angular velocity of a point on the beam and the 'l' subscript denotes evaluation at $x = l$; i.e. $\bar{v}_l = \bar{v}(x = l)$.

$$T_a = \frac{1}{2} m_a \bar{v}_l \cdot \bar{v}_l + \frac{1}{2} J_a \bar{\mu}_l \cdot \bar{\mu}_l \quad (5.1)$$

The velocity of the end mass is known from equation 3.7, the general velocity expression for the beam.

$$\begin{aligned} \bar{v}_l = & [l\dot{\theta} \cos \theta + \dot{v}_l \cos \theta - v_l \dot{\theta} \sin \theta] \bar{I} \\ & + [\dot{v}_l \sin \theta + v_l \dot{\theta} \cos \theta + l\dot{\theta} \sin \theta] \bar{J} \end{aligned} \quad (5.2)$$

The angular velocity of the end mass is computed from the angular addition theorem, where γ is the rotation of the beam relative to the $\bar{i}\bar{j}\bar{k}$ coordinate system.

$$\bar{\mu}_l = (\dot{\theta} + \dot{\gamma}) \bar{K} \quad (5.3)$$

However, $\dot{\gamma}$ is expressed in terms of the transverse displacement of the beam.

$$\dot{\gamma}_l \approx \frac{d}{dt} (v'_l) \quad (5.4)$$

Substitute equations 5.2, 5.3 and 5.4 into equation 5.1 to obtain the kinetic energy of the end mass.

$$\begin{aligned} T_a = & \frac{m_a}{2} (l^2 \dot{\theta}^2 + 2l\dot{\theta}\dot{v}_l + \dot{v}_l^2 + \dot{\theta}^2 v_l^2) \\ & + \frac{J_a}{2} \left[\dot{\theta} + \frac{d}{dt} (v'_l) \right]^2 \end{aligned} \quad (5.5)$$

The total kinetic energy of the system is obtained by summing equations 3.10 and 5.5.

$$T = \int_0^l \frac{\rho A}{2} [x^2 \dot{\theta}^2 + 2x\dot{\theta}\dot{v} - \dot{v}^2 + \dot{\theta}^2 v^2] dx + \frac{1}{2} J_l \dot{\theta}^2$$

$$\begin{aligned}
& + \frac{m_a}{2} (l^2 \dot{\theta}^2 + 2l\dot{\theta}\dot{v}_l + \dot{v}_l^2 - \dot{\theta}^2 v_l^2) \\
& + \frac{J_a}{2} \left[\dot{\theta} + \frac{d}{dt} (v_l') \right]^2
\end{aligned} \tag{5.6}$$

The potential energy expression for the arm, equation 3.16, is also applicable, with the addition of end mass terms. The potential energy of the end mass is due only to gravity.

$$\Pi = m_a g y_l \tag{5.7}$$

Extract y_l from the \bar{J} component of equation 3.6 and substitute it into equation 5.7. The potential energy expression then reduces to the following equation.

$$\Pi = m_a g (v_l \sin \theta - l \cos \theta) \tag{5.8}$$

The final expression for the potential energy is obtained by summing equations 3.16 and 5.8.

$$\begin{aligned}
\Pi = \frac{1}{2} K_t \theta^2 + \int_0^l \frac{EI}{2} (v'')^2 dx - \int_0^l \rho A g [v \sin \theta - x \cos \theta] dx \\
+ m_a g (v_l \sin \theta - l \cos \theta)
\end{aligned} \tag{5.9}$$

The boundary value problem is obtained by substitution of equations 5.6 and 5.9 into Hamilton's Principle, equation 3.17. The details of the variational calculus are similar to those shown in Section 3.1 and are not presented here. The following variational statement is obtained.

$$\begin{aligned}
& \int_{t_1}^{t_2} \left\{ \int_0^l [-\rho A (x^2 \ddot{\theta} + v^2 \ddot{\theta} + 2v\dot{v}\dot{\theta} + x\ddot{v}) - \rho Ag (v \cos \theta + x \sin \theta)] dx \right\} \delta \theta dt \\
& + \int_{t_1}^{t_2} \left\{ -m_a [l^2 \ddot{\theta} + v_l^2 \ddot{\theta} + 2v_l \dot{v}_l \dot{\theta} + l\ddot{v} + g (v_l \cos \theta + l \sin \theta)] \right\} \delta \theta dt \\
& + \int_{t_1}^{t_2} \left\{ -J_l \ddot{\theta} - K_t \theta - J_a \left(\ddot{\theta} + \frac{d^2}{dt^2} (v_l') \right) \right\} \delta \theta dt \\
& - \int_{t_1}^{t_2} \left\{ \int_0^l \rho A \left[v \dot{\theta}^2 - g \sin \theta - \ddot{v} - x \ddot{\theta} - \frac{1}{\rho A} (EIv'')'' \right] \delta v dx \right\} dt \\
& + \int_{t_1}^{t_2} \left\{ (EIv'') \delta v'(0) - \left[EIv'' - J_a \left(\ddot{\theta} + \frac{d^2}{dt^2} (v_l') \right) \right]_l \delta v'(l) \right\} dt \\
& + \int_{t_1}^{t_2} \left\{ (EIv'')' \delta v(0) \right\} dt \\
& + \int_{t_1}^{t_2} \left\{ [(EIv'')' + m_a (v \dot{\theta}^2 - g \sin \theta - ddot{v} - l\ddot{\theta})] \delta v(l) \right\} dt = 0 \quad (5.10)
\end{aligned}$$

This variational statement generates two partial differential equations:

$$\begin{aligned}
& - \int_0^l \rho A (x^2 \ddot{\theta} + v^2 \ddot{\theta} + 2v\dot{v}\dot{\theta} + x\ddot{v} - g (v \cos \theta + x \sin \theta)) dx \\
& - m_a (l^2 \ddot{\theta} + v_l^2 \ddot{\theta} + 2v_l \dot{v}_l \dot{\theta} + l\ddot{v} + g (v_l \cos \theta + l \sin \theta)) \\
& - J_l \ddot{\theta} - K_t \theta - J_a \left(\ddot{\theta} + \frac{d^2}{dt^2} (v_l') \right) = 0 \quad (5.11)
\end{aligned}$$

$$v \dot{\theta}^2 - g \sin \theta - \ddot{v} - x \ddot{\theta} - \frac{1}{\rho A} (EIv'')'' = 0 \quad (5.12)$$

two geometric boundary conditions:

$$v(0, t) = 0 \quad (5.13)$$

$$v'(0, t) = 0 \quad (5.14)$$

and two natural boundary conditions:

$$\left[EIv'' + J_a \left(\ddot{\theta} + \frac{d^2}{dt^2} (v_l') \right) \right]_l = 0 \quad (5.15)$$

$$\left[(EIv'')' + m_a (v\dot{\theta}^2 - g \sin \theta - \ddot{v} - l\ddot{\theta}) \right]_l = 0 \quad (5.16)$$

The solution to this boundary value problem may be obtained if the beam is uniform and homogeneous and the partial differential equations and boundary conditions are linearized about the equilibrium point, $(\theta, v) = (0, 0)$. Linearize the partial differential equations and the boundary conditions. Equations 5.11 through 5.16 reduce to the following forms.

$$\begin{aligned} -K_t \theta - \ddot{\theta} \left(J_l + \frac{\rho A l^3}{3} \right) - \rho A \int_0^l (x\ddot{v} + g v) dx - \frac{\rho A g l^2 \theta}{2} \\ - J_a \left(\ddot{\theta} + \frac{d^2}{dt^2} (v'_l) \right) - m_a (l^2 \ddot{\theta} - l\ddot{v}_l + g (v_l - l\theta)) = 0 \end{aligned} \quad (5.17)$$

$$-g\theta - \ddot{v} - x\ddot{\theta} - a^2 \frac{\partial^4 v}{\partial x^4} = 0 \quad (5.18)$$

$$v(0, t) = 0 \quad (5.19)$$

$$v'(0, t) = 0 \quad (5.20)$$

$$\left[EIv'' + J_a \left(\ddot{\theta} + \frac{d^2}{dt^2} (v'_l) \right) \right]_l = 0 \quad (5.21)$$

$$\left[EIv''' + m_a (-g\theta - \ddot{v} - l\ddot{\theta}) \right]_l = 0 \quad (5.22)$$

The solution to this boundary value problem is obtained by the method used in Section 3.1. In that section, the solution to equation 5.18 was shown to be the following equation.

$$\begin{aligned} Y(x) = C_1 \sin(\alpha x) + C_2 \cos(\alpha x) + C_3 \sinh(\alpha x) + C_4 \cosh(\alpha x) \\ + \Theta \left(\frac{g}{\omega^2} - x \right) \end{aligned} \quad (5.23)$$

The unknown coefficients in equation 5.23 are determined by substitution of equations 3.29 and 3.30 into the first partial differential equation, equation 5.17, and the boundary conditions, equations 5.19 to 5.22. The following five equations are obtained.

$$\begin{aligned}
& \Theta \left\{ \omega^2 J_l - K_t + \rho A l \left(\frac{gl}{2} - \frac{g^2}{\omega^2} \right) + m_a g l \left(1 - \frac{g}{\omega^2 l} \right) \right\} \\
& \quad + C_1 \left\{ a \omega \rho A \sin(\alpha l) + \frac{\rho A}{\alpha} \cos(\alpha l) (g - l \omega^2) \right\} \\
& \quad + C_1 \left\{ -\frac{\rho A g}{\alpha} + m_a \sin(\alpha l) (\omega^2 l - g) \right\} \\
& \quad + C_2 \left\{ a \omega \rho A \cos(\alpha l) + \frac{\rho A}{\alpha} \sin(\alpha l) (l \omega^2 - g) - a \omega \rho A \right\} \\
& \quad + C_2 \left\{ m_a \cos(\alpha l) (l \omega^2 - g) - J_a \omega^2 \alpha \sin(\alpha l) \right\} \\
& \quad + C_3 \left\{ \frac{\rho A}{\alpha} \cosh(\alpha l) (l \omega^2 - g) - a \omega \rho A \sinh(\alpha l) + \frac{\rho A g}{\alpha} \right\} \\
& \quad + C_3 \left\{ m_a \sinh(\alpha l) (l \omega^2 - g) + J_a \omega^2 \alpha \cosh(\alpha l) \right\} \\
& \quad + C_4 \left\{ \frac{\rho A}{\alpha} \sinh(\alpha l) (l \omega^2 - g) - a \omega \rho A \cosh(\alpha l) + a \omega \rho A \right\} \\
& \quad + C_4 \left\{ m_a \cosh(\alpha l) (l \omega^2 - g) + J_a \omega^2 \alpha \sinh(\alpha l) \right\} = 0 \quad (5.24)
\end{aligned}$$

$$\Theta \left(\frac{g}{\omega^2} \right) + C_2 + C_4 = 0 \quad (5.25)$$

$$-\Theta + \alpha C_1 + \alpha C_3 = 0 \quad (5.26)$$

$$\begin{aligned}
C_1 \left(-\alpha \sin(\alpha l) - \frac{J_a \omega^2}{EI} \cos(\alpha l) \right) + C_2 \left(-\alpha \cos(\alpha l) + \frac{J_a \omega^2}{EI} \sin(\alpha l) \right) \\
+ C_3 \left(\alpha \sinh(\alpha l) - \frac{J_a \omega^2}{EI} \cosh(\alpha l) \right) \\
+ C_4 \left(\alpha \cosh(\alpha l) - \frac{J_a \omega^2}{EI} \sinh(\alpha l) \right) = 0 \quad (5.27)
\end{aligned}$$

$$C_1 \left(-\alpha^3 \cos(\alpha l) + \frac{m_a \omega^2}{EI} \sin(\alpha l) \right) + C_2 \left(\alpha^3 \sin(\alpha l) + \frac{m_a \omega^2}{EI} \cos(\alpha l) \right)$$

$$\begin{aligned}
& +C_3 \left(\alpha^3 \cosh(\alpha l) + \frac{m_a \omega^2}{EI} \sinh(\alpha l) \right) \\
& +C_4 \left(\alpha^3 \sinh(\alpha l) + \frac{m_a \omega^2}{EI} \cosh(\alpha l) \right) = 0 \quad (5.28)
\end{aligned}$$

If the preceding equations are used in the following order, 5.25, 5.26, 5.27, 5.28, and 5.24; they may be expressed in the matrix form shown in equation 3.46. Therefore, the characteristic equation and mode shape derivations shown in Section 3.1 are also applicable to the end mass case. The only change is the B_{ij} coefficients are obtained from equations 5.24 to 5.28.

5.2 Derivation of Assumed Modes Model

The assumed modes model developed in Section 3.2 is easily extended to include the effect of an end mass. The kinetic and potential energy expressions developed in the previous section for the exact model are still valid. However, the assumed modes model allows use of the gravity correction term developed in Chapter 4, to account for the vertical displacement of the end mass. The correction term for the end mass is developed by analogy from equation 4.38.

$$\Pi = \frac{m_a g v_l^2}{2l} \cos \theta \quad (5.29)$$

The potential energy expression is obtained by summing equations 5.29 and 5.9.

$$\begin{aligned}
\Pi = \frac{1}{2} K_t \theta^2 + \int_0^l \frac{EI}{2} (v'')^2 dx + \int_0^l \rho A g [v \sin \theta - x \cos \theta] dx \\
+ \int_0^l \frac{\rho A g v^2}{2x} \cos \theta dx + m_a g (v_l \sin \theta - l \cos \theta) \\
+ \frac{m_a g v_l^2}{2l} \cos \theta \quad (5.30)
\end{aligned}$$

Represent the elastic displacement as a linear combination of the assumed mode shapes and the deformation coordinates

$$v(x, t) = \bar{D}^T \bar{\Psi} \quad (5.31)$$

However, the gravity correction terms in the potential energy expression only apply to the first mode. Therefore, let v in these terms be represented by a different linear combination.

$$v(x, t) = \bar{D}^T \bar{\Gamma} \quad (5.32)$$

where

$$\bar{\Gamma} = \{ \Psi_1 \ 0 \ 0 \} \quad (5.33)$$

The final kinetic and potential energy expressions are obtained by substituting equations 5.31 and 5.32 into the kinetic and potential energy expressions for the system, equations 5.6 and 5.30; and using transformations similar to equation 3.60.

$$\begin{aligned} T = \int_0^l \frac{\rho A}{2} \left[x^2 \dot{\theta}^2 + 2x \dot{\theta} \dot{\bar{D}}^T \bar{\Psi} + \dot{\bar{D}}^T \bar{\Psi} \dot{\bar{D}} + \dot{\theta}^2 \bar{D}^T \bar{\Psi} \bar{D} \right] dx + \frac{1}{2} J_l \dot{\theta}^2 \\ + \frac{m_a}{2} \left(l^2 \dot{\theta}^2 + 2l \dot{\theta} \dot{\bar{D}}^T \bar{\Psi}_l - \dot{\bar{D}}^T \bar{\Psi}_l \dot{\bar{D}} + \dot{\theta}^2 \bar{D}^T \bar{\Psi}_l \bar{D} \right) \\ + \frac{J_a}{2} \left(\dot{\theta} + \dot{\bar{D}}^T \bar{\Psi}'_l \right)^2 \end{aligned} \quad (5.34)$$

$$\begin{aligned} \Pi = \frac{1}{2} K_t \theta^2 + \int_0^l \frac{EI}{2} \bar{D}^T \tilde{\Upsilon} \bar{D} + \int_0^l \rho A g \left[\bar{D}^T \bar{\Psi} \sin \theta - x \cos \theta \right] dx \\ + \int_0^l \frac{\rho A g}{2x} \bar{D}^T \bar{\Gamma} \bar{D} \cos \theta dx + m_a g \left(\bar{D}^T \bar{\Psi}_l \sin \theta - l \cos \theta \right) \\ + \frac{m_a g}{2l} \bar{D}^T \bar{\Gamma}_l \bar{D} \cos \theta \end{aligned} \quad (5.35)$$

$\bar{\Gamma}$ and $\tilde{\Upsilon}$ are n by n modal matrices defined by equations 4.42 and 3.64.

The nonlinear equations of motion are obtained by applying Lagrange's equation, equation 3.65, to the kinetic and potential energy expressions. The resulting set of $n + 1$, nonlinear ordinary differential equations is shown in equation 5.36.

$$\bar{M} \begin{Bmatrix} \ddot{\theta} \\ \ddot{D} \end{Bmatrix} + \bar{K} \begin{Bmatrix} \theta \\ D \end{Bmatrix} + \bar{P} = \bar{0} \quad (5.36)$$

where \bar{M} , \bar{K} , and \bar{P} are as follows.

$$\bar{M} = \begin{bmatrix} \int_0^l \rho A x^2 dx + J_l + m_a l^2 + J_a & \int_0^l \rho A x \bar{\Psi}^T dx + m_a l \bar{\Psi}_l^T + J_a \bar{\Psi}_l'^T \\ \int_0^l \rho A x \bar{\Psi} dx + m_a l \bar{\Psi}_l + J_a \bar{\Psi}_l' & \int_0^l \rho A \bar{\Psi} dx + m_a \bar{\Psi}_l - J_a \bar{\Omega}_l \end{bmatrix} \quad (5.37)$$

$$\bar{K} = \begin{bmatrix} K_t & \bar{0}^T \\ \bar{0} & \int_0^l EI \bar{\Upsilon} dx \end{bmatrix} \quad (5.38)$$

$$\bar{P} = \begin{Bmatrix} \int_0^l \rho A (\ddot{\theta} \bar{D}^T \bar{\Psi} \bar{D} - 2\dot{\theta} \dot{\bar{D}}^T \bar{\Psi} \bar{D}) dx + \int_0^l \rho A g (\bar{\Psi}^T \bar{D} \cos \theta - x \sin \theta) dx \\ \int_0^l \rho A g \bar{\Psi} \sin \theta dx - \int_0^l \rho A \dot{\theta}^2 \bar{\Psi} \bar{D} dx \\ + m_a \begin{Bmatrix} \ddot{\theta} \bar{D}^T \bar{\Psi}_l \bar{D} + 2\dot{\theta} \dot{\bar{D}}^T \bar{\Psi}_l \bar{D} + g (\bar{\Psi}_l^T \bar{D} \cos \theta + l \sin \theta) \\ g \bar{\Psi}_l \sin \theta - \dot{\theta}^2 \bar{\Psi}_l \bar{D} \end{Bmatrix} \\ + g \begin{Bmatrix} -\frac{m_a g}{2l} \bar{D}^T \bar{\Gamma}_l \bar{D} \sin \theta - \int_0^l \frac{\rho A}{2x} \bar{D}^T \bar{\Gamma} \bar{D} \sin \theta dx \\ \frac{m_a g}{l} \bar{\Gamma}_l \bar{D} \cos \theta + \int_0^l \frac{\rho A}{x} \bar{\Gamma} \bar{D} \cos \theta dx \end{Bmatrix} \end{Bmatrix} \quad (5.39)$$

$\bar{\Omega}$ is defined by the following equation.

$$\bar{\Omega} = \bar{\Psi}' \bar{\Psi}'^T \quad (5.40)$$

Linear equations of motion are obtained by linearizing \bar{P} about the point $\bar{q} = 0$. The resulting set of linear differential equations is given by the following equation;

$$\bar{M}\ddot{\bar{q}} + \bar{K}\bar{q} = \bar{0} \quad (5.41)$$

where \bar{K} is the linearized stiffness matrix.

$$\bar{K} = \begin{bmatrix} K_t + \int_0^l \rho Agx \, dx + m_agl & \int_0^l \rho Ag\bar{\Psi}^T \, dx + m_ag\bar{\Psi}_l^T \\ \int_0^l \rho Ag\bar{\Psi} \, dx + m_ag\bar{\Psi}_l & \int_0^l EI\bar{\Upsilon} \, dx + \int_0^l \frac{\rho Ag}{x}\bar{\Gamma} \, dx + \frac{m_ag}{l}\bar{\Gamma}_l \end{bmatrix} \quad (5.42)$$

The natural frequencies of the system are determined by solving the eigenvalue problem corresponding to equation 5.41.

5.3 Derivation of Rigid Model

For purposes of comparison, a rigid model of the robot arm with end mass is derived. Using the free body diagram shown in Figure 5.2 and summing moments about point O yields the equation of motion.

$$-K_t\theta - \frac{mgl}{2}\sin\theta - m_agl\sin\theta = \left(J_l + \frac{ml^2}{3} + J_a + m_al^2\right)\ddot{\theta} \quad (5.43)$$

Linearize the $\sin\theta$ term by assuming θ is small. Then equation 5.43 reduces to the differential equation of a undamped oscillator.

$$\left(J_l + \frac{ml^2}{3} + J_a + m_al^2\right)\ddot{\theta} + \left(K_t + \frac{mgl}{2} + m_agl\right)\theta = 0 \quad (5.44)$$

Therefore, the only natural frequency available from the rigid model is given by equation 5.45.

$$f_r = \frac{1}{2\pi} \sqrt{\frac{K_t + \frac{mgl}{2} + m_agl}{J_l + \frac{ml^2}{3} + J_a + m_al^2}} \quad (5.45)$$

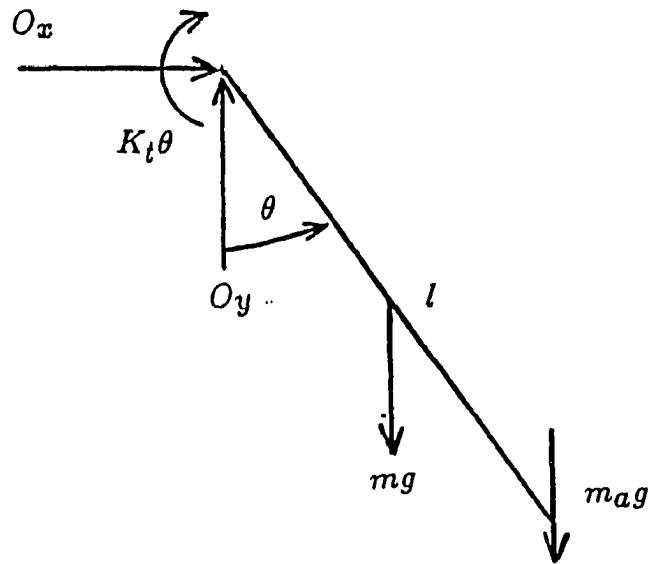


Figure 5.2: Free body diagram of rigid arm

5.4 Effect of Mode Shape Selection

This section studies the effect of assumed mode shape selection upon the accuracy of the model of the elastic arm with an end mass. In Chapter 4, alternative mode shapes for the elastic arm with a free end were developed and studied, to determine the best assumed mode shapes for modeling of the elastic arm. This section extends this work to an elastic arm with end mass.

5.4.1 Development of Alternative Assumed Mode Shapes

In Section 4.2.1, alternative assumed mode shapes were developed for the elastic arm without an end mass. The criteria for this development were the boundary conditions of the problem. Addition of the end mass only affects the two natural boundary conditions of the arm. Therefore, alternative assumed mode shapes for

the arm with end mass are developed in a manner similar to that for the free arm.

Since the end mass does not affect the geometric boundary conditions, they are unchanged from Section 4.2.1.

$$\Psi_i(0) = 0 \quad (5.46)$$

$$\Psi'_i(0) = 0 \quad (5.47)$$

The natural boundary conditions are affected by the addition of the end mass and are derived from the natural boundary conditions of the exact solution, equations 5.21 and 5.22. Neglect the θ terms in these two equations since the assumed mode shapes are only functions of x . Furthermore, assume $v(x, t)$ is harmonic. The natural boundary conditions then simplify to the following equations.

$$EI \frac{\partial^2 \Psi_i}{\partial x^2}(l) = J_a \omega_i^2 \frac{\partial \Psi_i}{\partial x}(l) \quad (5.48)$$

$$EI \frac{\partial^3 \Psi_i}{\partial x^3}(l) = -m_a \omega_i^2 \Psi_i(l) \quad (5.49)$$

The normal modes of a cantilever-mass loaded beam are used as approximations to the eigenfunctions of the elastic arm. Although these mode shapes do not satisfy the partial differential equations, they do satisfy the geometric and natural boundary conditions of the problem, and are orthogonal. Development of these assumed mode shapes is presented in Appendix C.

The normal mode shapes of the cantilever beam were used as approximate eigenfunctions for the elastic arm without an end mass. With the addition of the end mass, these mode shapes no longer satisfy the natural boundary conditions. Therefore, they may no longer be used as comparison functions. However, they still satisfy the geometric boundary conditions of the problem, qualifying them as admissible functions for the elastic arm with end mass.

The monomials were used as admissible polynomials for the elastic arm without end mass, and are used in the same capacity for the arm with end mass.

$$\Psi_i(x) = x^{i+1}; \quad i = 1, 2, 3 \quad (5.50)$$

These assumed mode shapes qualify as admissible functions as they are continuous, complete, linearly independent, and satisfy the geometric boundary conditions. However, they do not satisfy the natural boundary conditions, nor are they orthogonal.

The admissible polynomials developed in Section 4.2.1 are also used for the arm with end mass.

$$\Psi_1(x) = x^2 \quad (5.51)$$

$$\Psi_2(x) = x^2 - \frac{6x^3}{5l} \quad (5.52)$$

$$\Psi_3(x) = x^2 - \frac{14x^3}{5l} + \frac{28x^4}{15l^2} \quad (5.53)$$

Since the addition of the end mass only affected the natural boundary conditions, these polynomials remain orthogonal and still satisfy the geometric boundary conditions. Therefore, they are used as admissible polynomials for the arm with an end mass.

In Section 4.2.1, a set of comparison polynomials was developed by imposing geometric and natural boundary conditions, and orthogonality conditions upon a set of polynomials. These polynomials were similar to the more complicated cantilever mode shapes in satisfying the boundary and orthogonality conditions, but they eliminated the requirement for numerical integration of the assumed mode shapes in formulating the equations of motion. This method may also be applied to the elastic arm with end mass.

The geometric and natural boundary conditions to be applied to the polynomials are given by equations 5.46 to 5.49. Application of the natural boundary conditions is complicated by the natural frequency, ω_i , in the boundary condition expression. The natural frequency of a cantilever-mass loaded beam is used in application of these boundary conditions, since the purpose of the comparison polynomials is to approximate the more complex cantilever-mass loaded mode shapes.

To obtain the comparison polynomials for the arm with end mass, start with the following set of assumed mode shapes.

$$\Psi_1(x) = a_1 + b_1x + c_1x^2 + d_1x^3 + e_1x^4 \quad (5.54)$$

$$\Psi_2(x) = a_2 + b_2x + c_2x^2 + d_2x^3 + e_2x^4 + f_2x^5 \quad (5.55)$$

$$\Psi_3(x) = a_3 + b_3x + c_3x^2 + d_3x^3 + e_3x^4 + f_3x^5 + g_3x^6 \quad (5.56)$$

Application of the geometric boundary conditions eliminates the a_i and b_i coefficients. The first comparison polynomial is obtained by applying the natural boundary conditions to equation 5.54 and making c_1 unity. The resulting set of two linear algebraic equations, shown in Appendix B, are solved for d_1 and e_1 . The second comparison polynomial is obtained in a similar manner. Natural boundary conditions are imposed on equation 5.55, as is the orthogonality condition between Ψ_1 and Ψ_2 . By letting c_2 equal unity, the set of three linear algebraic equations may be solved for d_2 , e_2 , and f_2 . These equations are shown in Appendix B. The third comparison polynomial is obtained by applying the natural boundary conditions to equation 5.56, imposing orthogonality conditions between Ψ_3 and the other two comparison polynomials, and making c_3 unity. The set of four equations, shown in Appendix B, is then solved for the unknown coefficients, d_3 through e_3 .

Table 5.1: End mass parameters

Case	m_a (lb-sec ² -in ⁻¹)	J_a (lb-sec ² -in)	m_a/m
A	1.131×10^{-4}	1.220×10^{-5}	0.25
B	4.557×10^{-4}	1.311×10^{-4}	1.00

5.4.2 Results

To study the effect of mode shape selection, the natural frequencies of the assumed modes model are compared to those of the exact model and experimental data. Gravity is removed from the problem for simplification. The assumed modes model is used with the five different sets of assumed mode shapes developed in section 5.4.1. As each set has three assumed mode shapes, each model has four degrees of freedom. The modal integrals in the mass and stiffness matrices are evaluated analytically for the polynomial mode shapes and numerically for the cantilever and cantilever-mass loaded mode shapes.

The parameters for the arm are those of case 1 in Chapter 4 and are listed in Table 4.1. Two different end masses are used, the first having the ratio of the end mass to the mass of the beam equal 0.25 while the second has a mass ratio of 1.0. The parameters for both of these end masses are shown in Table 5.1.

Figures 5.3 and 5.4 show that all of the assumed mode shapes are equally accurate for the first mode, for both end masses. All of the coupled models agree with the exact solution and correlate with the experimental data. These results are similar to those shown for the arm without an end mass, Figure 4.4. As for the arm with no end mass, the linear combinations of the assumed mode shapes as defined by the first eigenvector, shown in Figures 5.5 and 5.6, explain the frequency

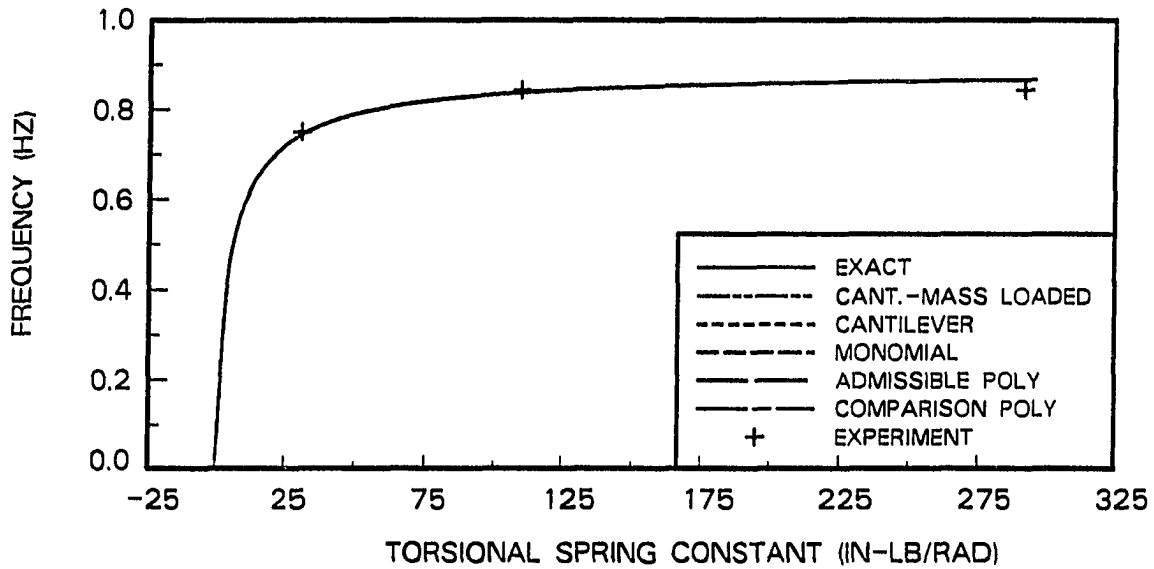


Figure 5.3: Comparison of first natural frequencies from alternative assumed mode shapes; horizontal orientation; case 1; $(m_a/m) = 0.25$

results. The similarity between the linear combinations of assumed mode shapes and the exact mode shapes shows that all of the sets of assumed mode shapes are good bases for representing the elasticity of the robot arm, despite the addition of the end mass.

Figures 5.7 and 5.8 show that mode shape selection is more important for the second mode of the system. For a mass ratio of 0.25, Figure 5.7 shows all of the alternative models, with the exception of the admissible polynomial model, agree with the exact solution and the experimental data. When the mass ratio is increased to 1.0, the differences between the models increase. As shown in Figure 5.8, the cantilever-mass loaded and monomial models still agree with the exact solution while the cantilever model is slightly in error. The admissible polynomial model is less accurate than the previously discussed models, while the comparison polynomial

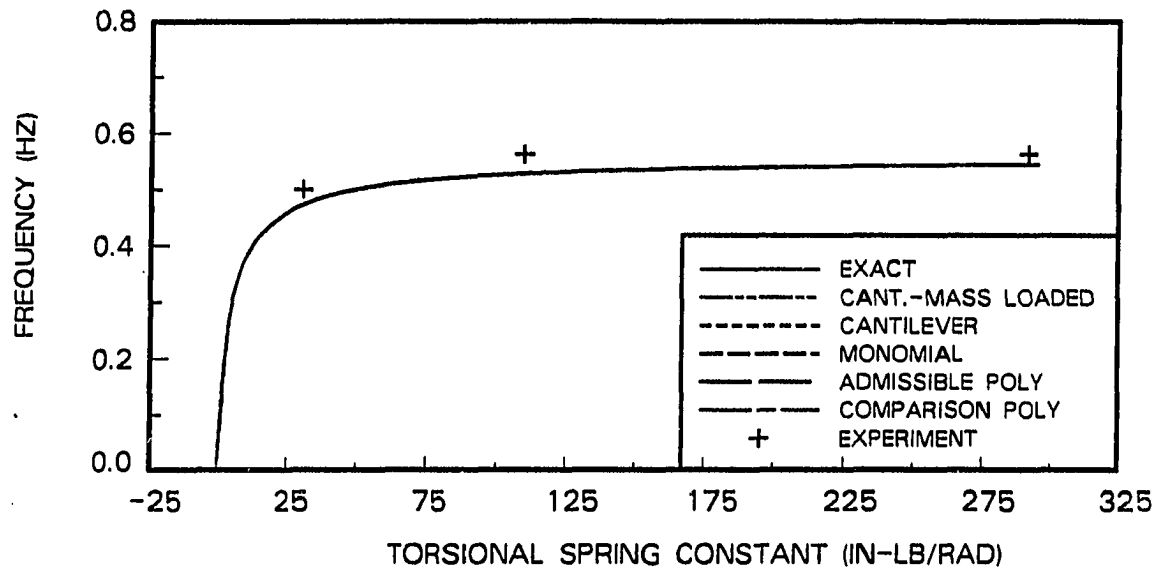


Figure 5.4: Comparison of first natural frequencies from alternative assumed mode shapes; horizontal orientation; case 1; $(m_a/m) = 1.0$

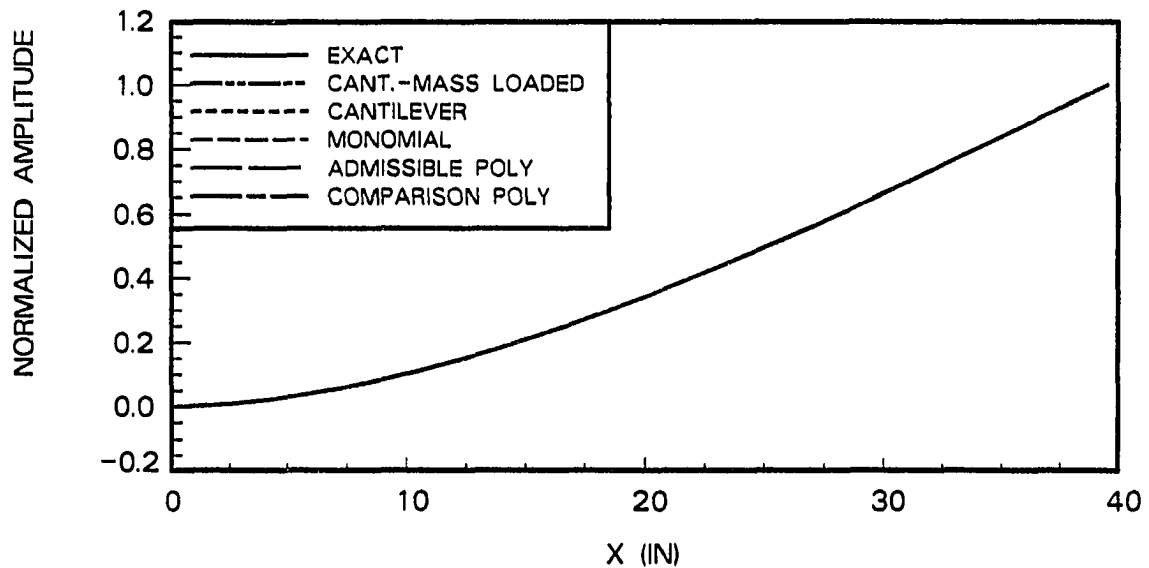


Figure 5.5: Comparison of linear combinations of assumed mode shapes to first exact mode shape; $K_t = 200 \text{ in-lb-rad}^{-1}$; horizontal orientation; case 1; $(m_a/m) = 0.25$

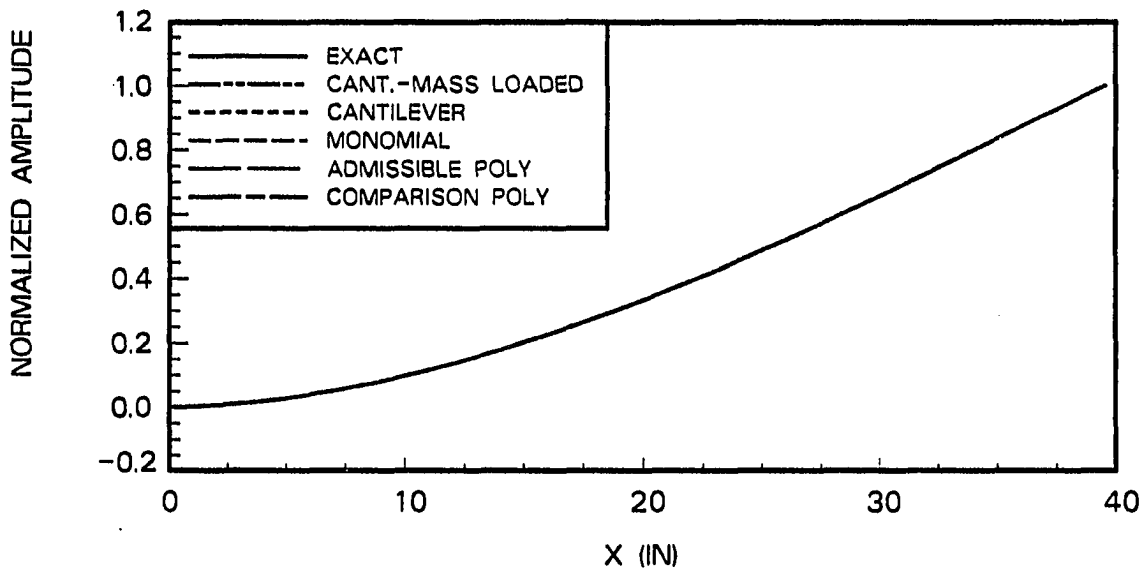


Figure 5.6: Comparison of linear combinations of assumed mode shapes to first exact mode shape; $K_t = 200 \text{ in-lb-rad}^{-1}$; horizontal orientation; case 1; $(m_a/m) = 1.0$

model differs significantly from the exact model.

The linear combinations of the assumed mode shapes for the second mode are similar to those for the free arm in Figure 4.8. Figure 5.9 shows that for a mass ratio of 0.25, all of the coupled system mode shapes are similar to the exact mode shape. The small differences between the mode shapes correlate to small differences between the frequencies of the models in Figure 5.7. Figure 5.10 shows similar behavior for a mass ratio of 1.0. Except for the comparison polynomial model, the linear combinations of mode shapes are similar to the exact mode shape. This observation agrees with Figure 5.8, which shows significant frequency errors for the comparison polynomial model.

The experimental data for the mass ratio of 1.0 does not agree with the exact solution as well as the data for the mass ratio of 0.25. This trend is due to an error

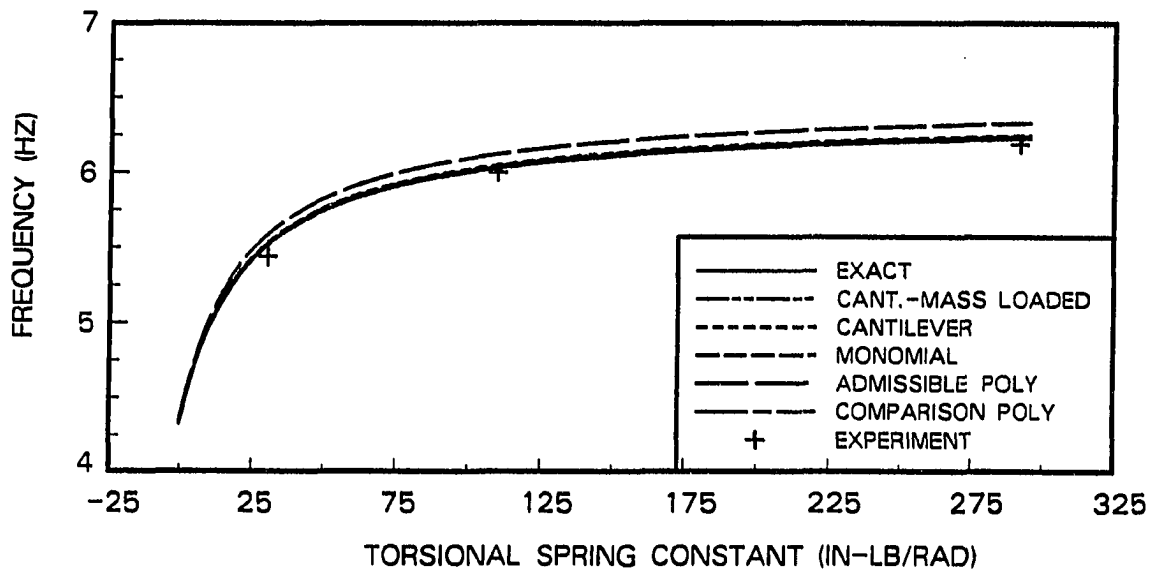


Figure 5.7: Comparison of second natural frequencies from alternative assumed mode shapes; horizontal orientation; case 1; $(m_a/m) = 0.25$

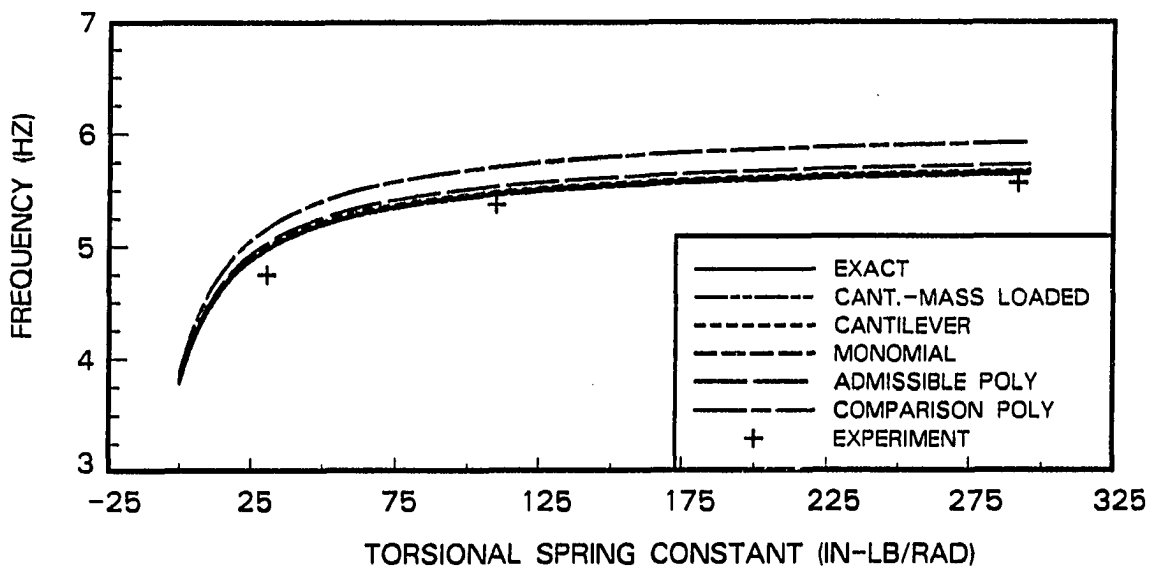


Figure 5.8: Comparison of second natural frequencies from alternative assumed mode shapes; horizontal orientation; case 1; $(m_a/m) = 1.0$

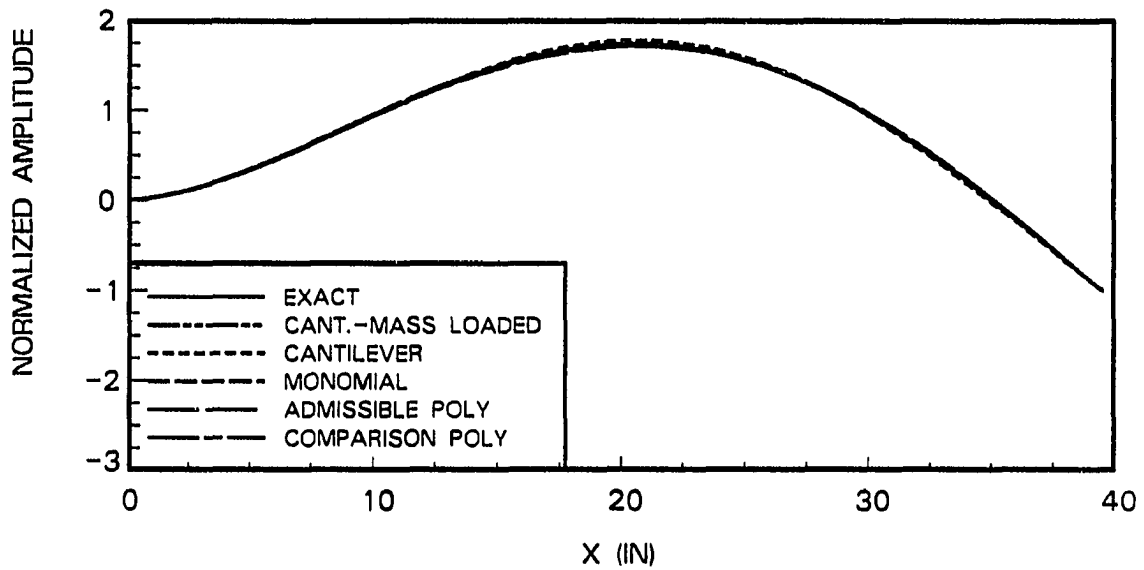


Figure 5.9: Comparison of linear combinations of assumed mode shapes to second exact mode shape; $K_t = 200 \text{ in-lb-rad}^{-1}$; horizontal orientation; case 1; $(m_a/m) = 0.25$

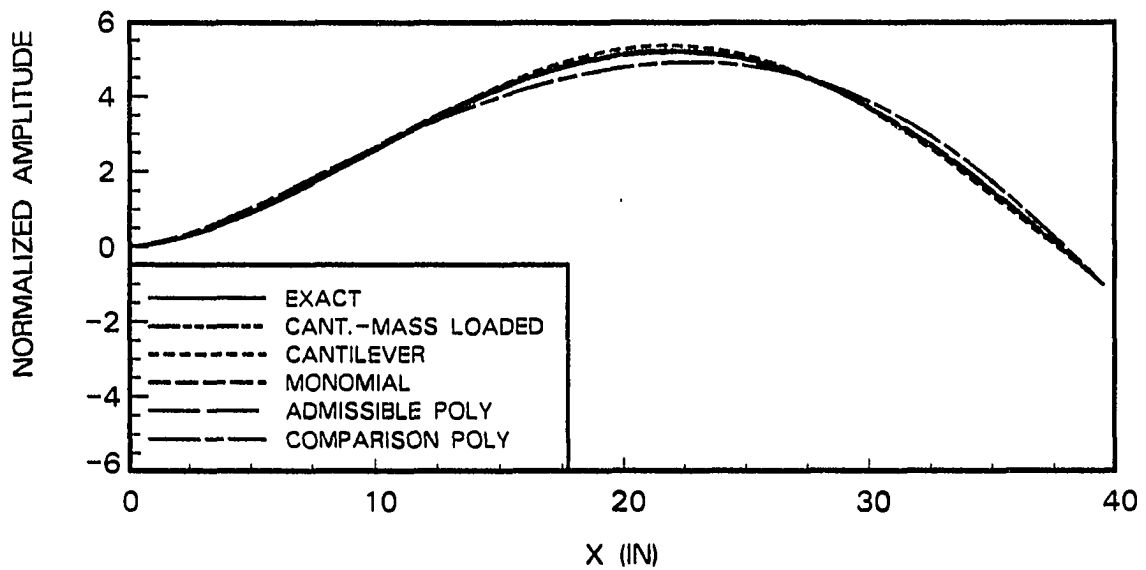


Figure 5.10: Comparison of linear combinations of assumed mode shapes to second exact mode shape; $K_t = 200 \text{ in-lb-rad}^{-1}$; horizontal orientation; case 1; $(m_a/m) = 1.0$

in the experiment. When the mass ratio is 1.0, the end mass causes large torsional deformations of the beam. Since the arm is horizontal, the deformations lower the elevation of the end mass. The resulting decrease in the gravitational potential energy of the system significantly reduces the natural frequencies of the system. To suppress the torsional deformations, a string was used to support the end of the arm. Although the string improved the agreement of the natural frequencies with the exact model, it reduced the overall accuracy of the experiment since the tension in the support string became a variable in the experiment.

The cantilever-mass loaded and monomial mode shapes are the best assumed mode shapes for the elastic arm in the horizontal plane. While both provide accurate frequencies, the monomial assumed mode shapes offer a significant computational savings in formulation of the equations of motion.

5.5 Coupling of Elastic and Gross Motion

This section examines coupling between elastic and gross motions of the elastic arm with end mass. To simplify the problem, gravity is neglected. Figures 5.11 and 5.12 compare the first natural frequencies of the exact model, the rigid model developed in Section 5.3, and an uncoupled cantilever-mass loaded model. The coupling effect between the elastic and gross motions for the elastic arm with end mass is similar to that for the free arm. The discrepancy between the rigid and exact models in Figures 5.11 and 5.12 is analogous to that shown in Figure 4.9. At low values of K_t , the coupled and uncoupled models agree since the frequencies of the elastic and rigid motions are sufficiently separated. As the torsional spring becomes increasingly stiff, the rigid body frequency increases. When this frequency

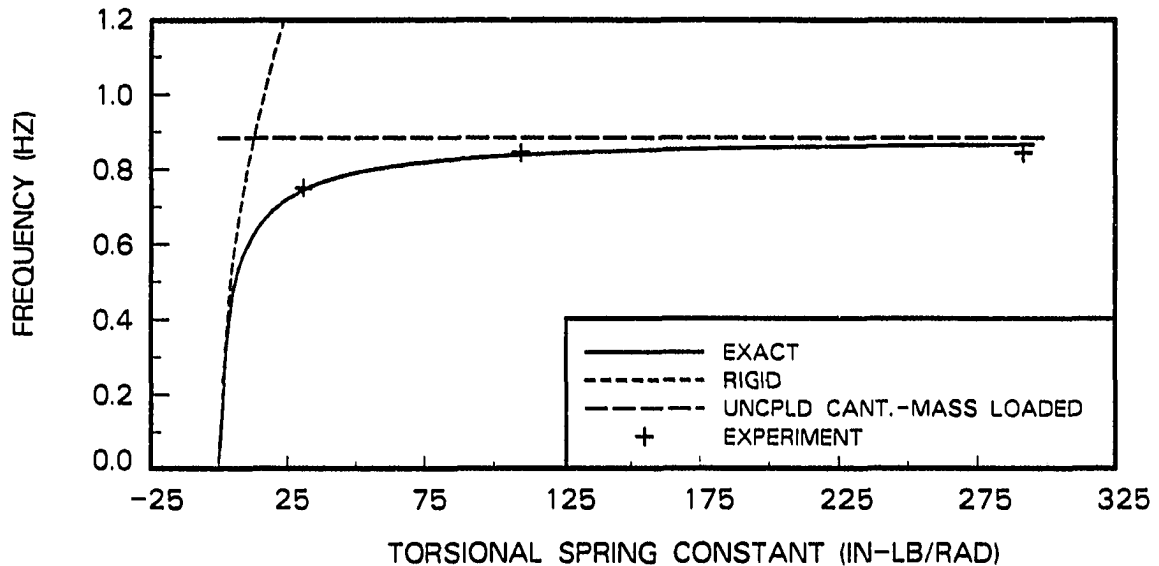


Figure 5.11: Comparison of first natural frequencies of coupled and uncoupled models; horizontal orientation; case 1; $(m_a/m) = 0.25$

nears the frequency of the elastic motion, the motions couple and produce modes having both motions. As K_t becomes very large, the gross motion becomes very small compared to the elastic motion and the modes become dominated by the elastic motion.

The coupling effect was illustrated for the free arm in Figure 4.10, by plotting the frequency shift from the rigid model to the exact solution, versus the ratio of the rigid frequency to the uncoupled cantilever frequency. Figure 5.13 is a similar plot for the arm with end mass. The frequency shift from the rigid model to the exact solution is plotted versus the ratio of the rigid frequency to the uncoupled cantilever-mass loaded frequency. Both mass ratios show identical frequency shifts. Unfortunately, this plot is not as easy to use as the free arm plot, since the uncoupled cantilever-mass loaded frequency is not easily calculated.

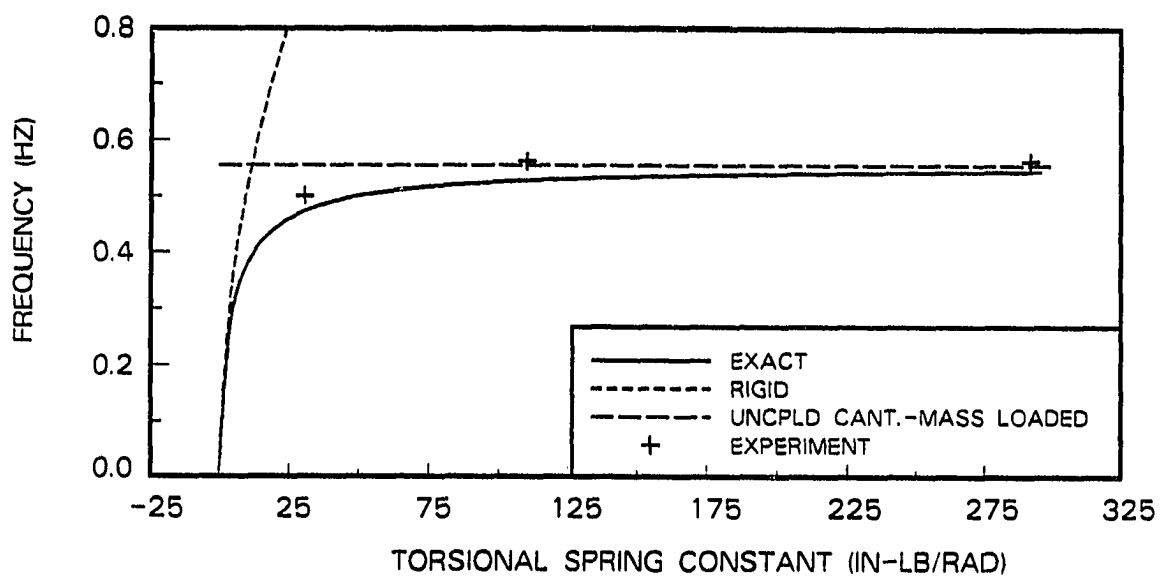


Figure 5.12: Comparison of first natural frequencies of coupled and uncoupled models; horizontal orientation; case 1; $(m_a/m) = 1.0$

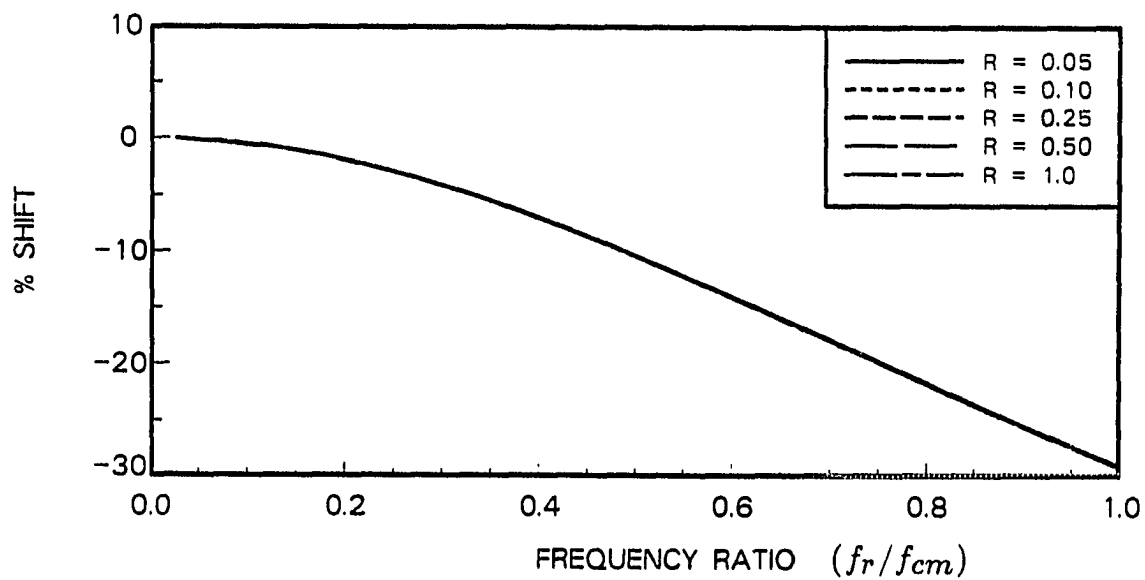


Figure 5.13: Frequency shift from rigid model as function of (f_r/f_{cm})

Figure 5.14 presents a coupling effect graph that is easier to use. This figure plots the same frequency shift from the rigid model versus the ratio of the rigid frequency to the frequency of a cantilever beam without end mass. Different mass ratios now result in different frequency shift curves. However, the frequency ratio is much easier to calculate. The dependency of the frequency shift upon both frequency ratio and mass ratio is now apparent.

A conventional robot has a very low frequency ratio due to its large mass and high transverse stiffness. In addition, the large mass of the arm relative to the payload gives the robot a low mass ratio. Figure 5.14 shows that a combination of low frequency and mass ratios gives small frequency shifts. Rigid models would be accurate in this region. The low frequency ratio of a conventional robot also places it in a region where the frequency shift is not significantly affected by a change in the mass ratio. Therefore, the rigid natural frequency of a conventional robot is not significantly altered by its payload.

Elastic robots have large frequency ratios due to their low mass and transverse stiffness. They operate in a region characterized by large frequency shifts and a strong dependence of the frequency shift upon the mass ratio. Due to their low mass, the mass ratios of elastic arms change significantly with changes in the payload. Therefore, the natural frequencies of elastic robot arms are strongly influenced by their payload. Figure 5.14 is a simple but effective design tool which shows the effects of both frequency and mass ratio upon the frequency shifts of elastic robot arms.

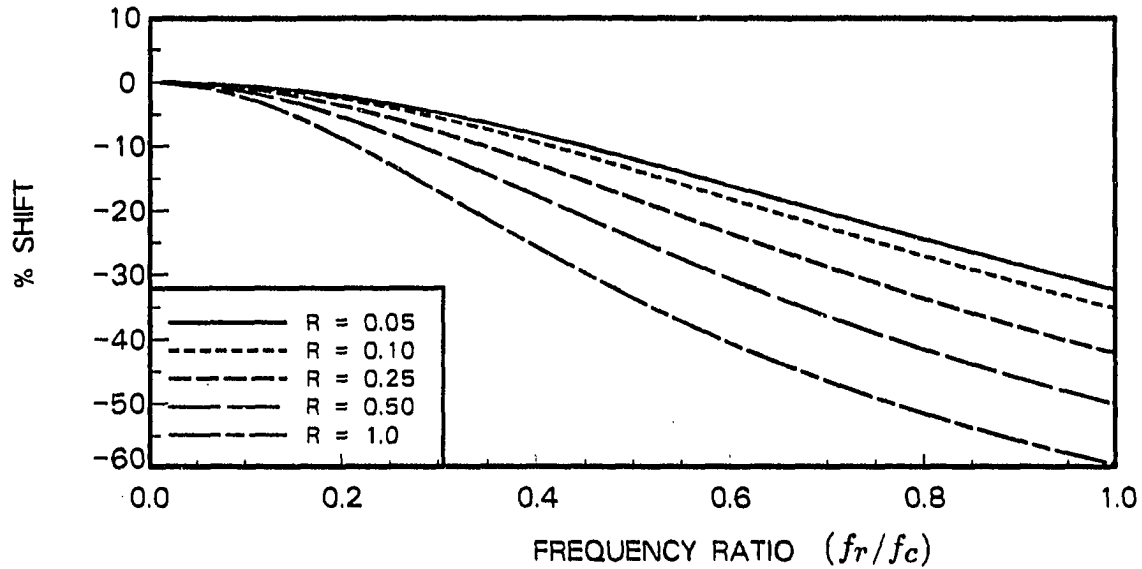


Figure 5.14: Error in rigid model as function of (f_r/f_c)

5.6 Effect of Gravity

This section investigates the elastic arm in a vertical position, where gravity has significant effects on the accuracy of the model. Figures 5.15 and 5.16 compare the first natural frequency of the exact and coupled cantilever-mass loaded models to experimental data, for mass ratios of 0.25 and 1.0, respectively. The assumed modes model agrees with the experimental data for both mass ratios. However, the frequencies of the exact model differ significantly from the experimental data. The inaccuracy of the exact model is caused by its neglect of the vertical displacement effect. The accuracy of the first mode of the assumed modes model in the presence of gravity can be attributed to the gravity correction term used to correct for the vertical displacement effect. Chapter 4 showed the importance of the vertical displacement effect for an arm without an end mass. Addition of an end mass mag-

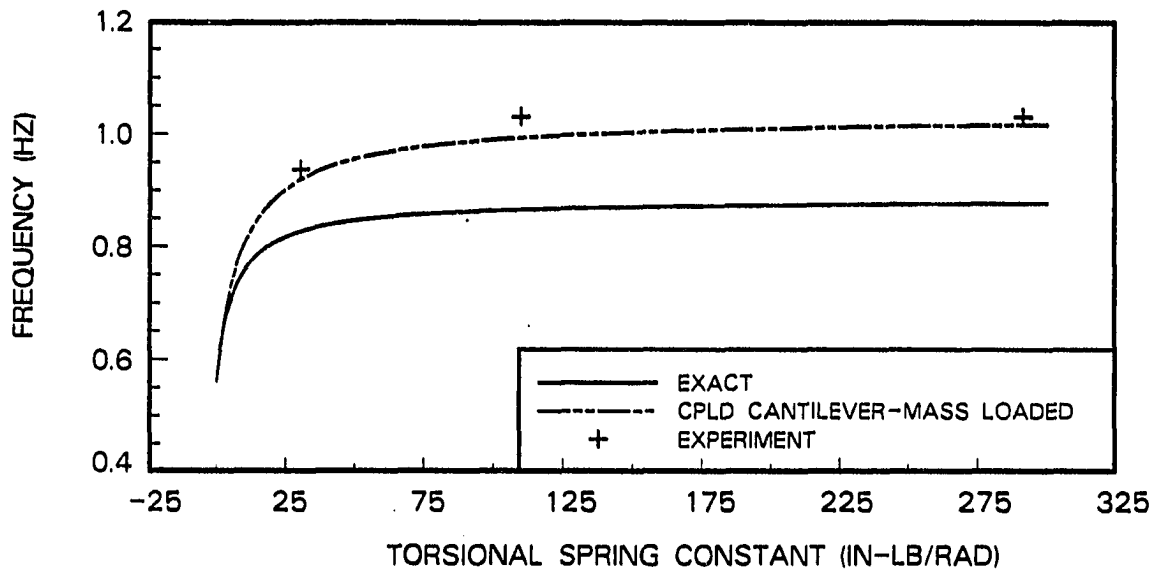


Figure 5.15: First natural frequency of coupled models in presence of gravity; case 1; $(m_a/m) = 0.25$

Table 5.2: Effect of gravity on experimentally measured first natural frequency of cantilever-mass loaded beam; $(m_a/m) = 1.0$

Case	f_1 (Hz) (No g)	f_1 (Hz) (With g)	% change due to g
1	0.562	0.781	39.0
2	1.062	1.218	14.7
3	2.312	2.437	5.40

nifies the importance of the this effect. This is illustrated by Table 5.2, which shows the experimentally measured first natural frequencies of cantilever beams with end mass ratios of 1.0. The increases in the frequencies due to gravity are much larger than the corresponding increases for the cantilever beam without end mass (see Table 4.5).

The assumed modes model is less accurate in predicting the second natural frequency of the arm. Figure 5.17 compares the second natural frequency of the

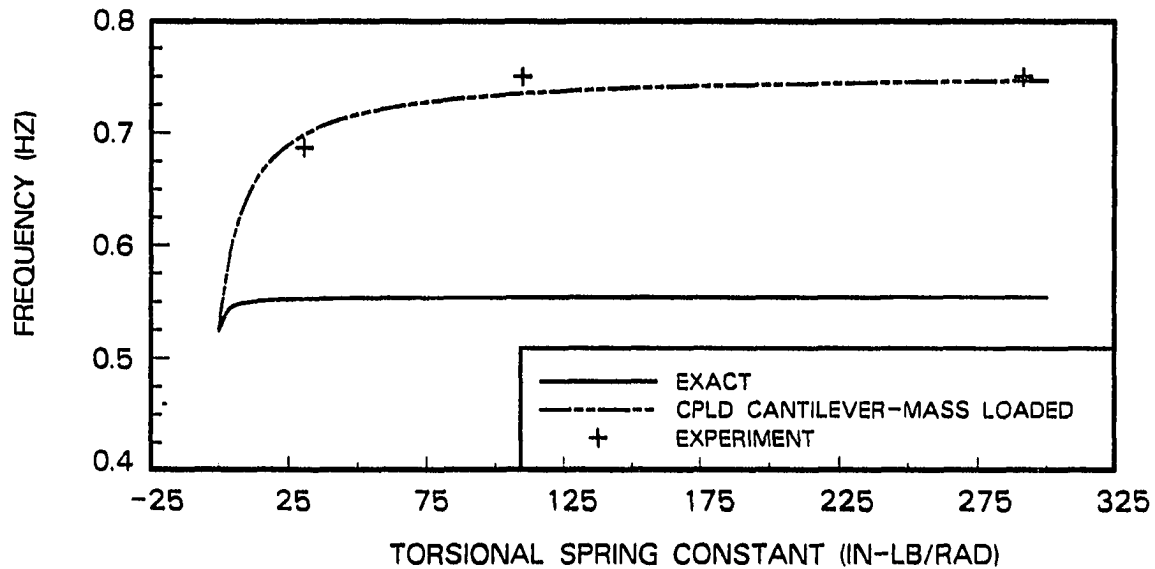


Figure 5.16: First natural frequency of coupled models in presence of gravity; case 1; $(m_a/m) = 1.0$

arm to experimental data for a mass ratio of 0.25. The natural frequencies of the model are lower than the experimental frequencies and the error increases with increasing K_t . When the mass ratio is increased to 1.0, as in Figure 5.18, the errors increase. The exact model is more accurate for the second mode than for the first mode, since the vertical displacement effect is less significant for this mode.

The errors in the second natural frequency are due to the vertical displacement effect. These errors are not present in Figures 5.7 and 5.8, which present the same model in the absence of gravity. In addition, the same type of errors, underestimation of the natural frequency and increased error for larger values of K_t , were observed in Chapter 4 for the first mode of the free arm, before the gravity correction term was included in the model. Chapter 4 showed that gravity did not significantly affect the second natural frequency of the arm. However, the end mass

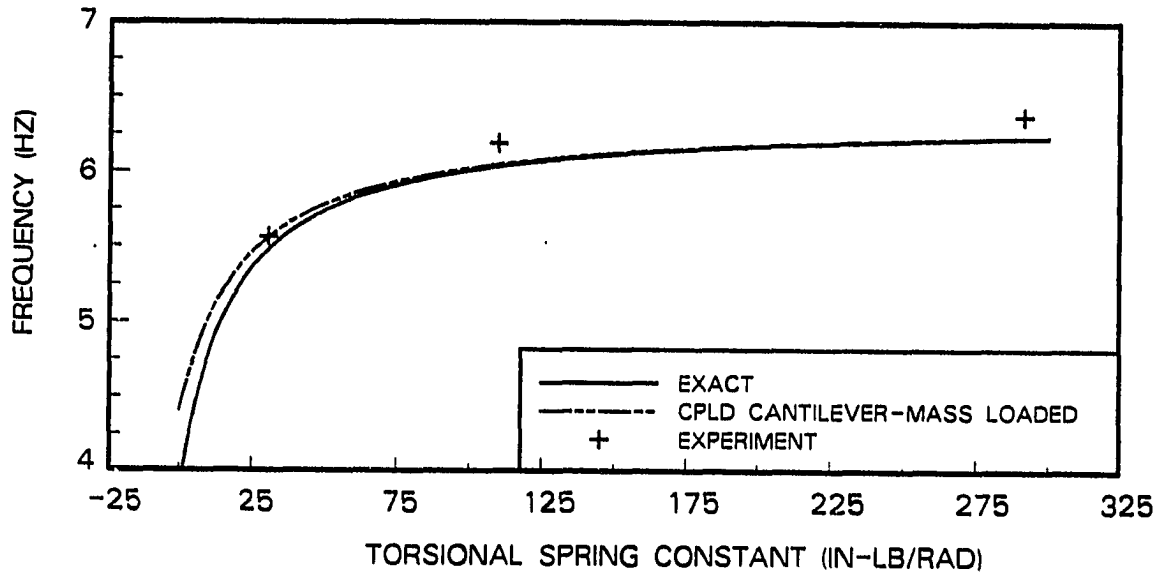


Figure 5.17: Second natural frequency of coupled models in presence of gravity; case 1; $(m_a/m) = 0.25$.

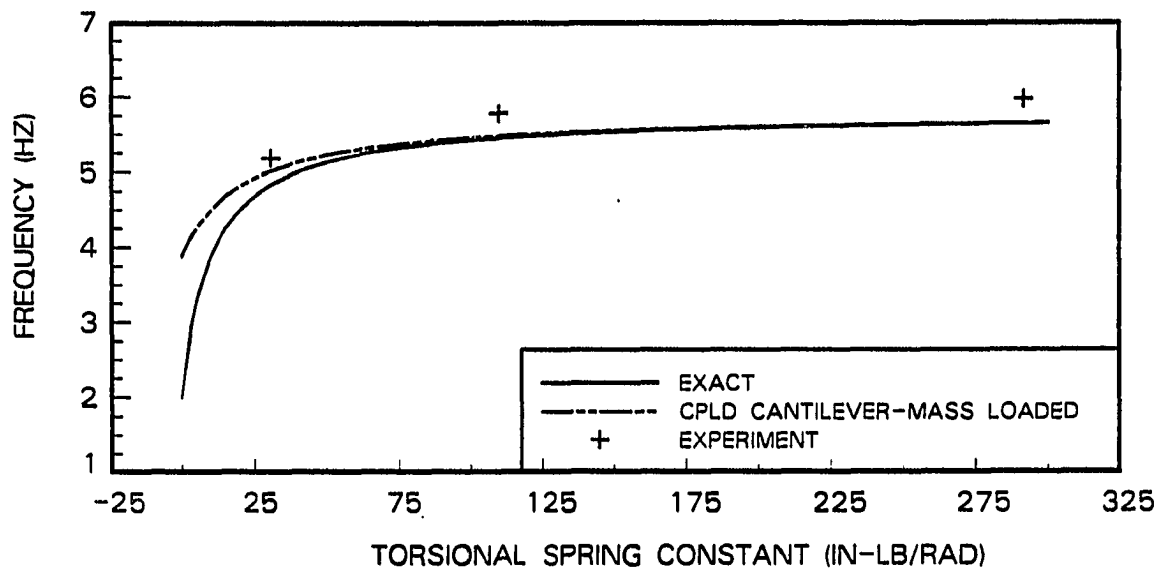


Figure 5.18: Second natural frequency of coupled models in presence of gravity; case 1; $(m_a/m) = 1.0$

Table 5.3: Effect of gravity on experimentally measured second natural frequency of cantilever-mass loaded beam; $(m_a/m) = 1.0$

Case	f_2 (Hz) (No g)	f_2 (Hz) (With g)	% change due to g
1	5.593	6.031	7.83
2	11.156	11.281	1.12

magnifies the importance of the vertical displacement effect. This is illustrated for the second mode by the experimentally measured second natural frequencies of a cantilever beam with end mass. As shown in Table 5.3, the increases in the second natural frequency due to gravity are much larger than the corresponding free arm cases shown in Table 4.6.

In Chapter 4, the vertical displacement effect was incorporated into the coupled model by a gravity correction term. However, the correction term is valid only for the first mode. Therefore, this gravity correction cannot be used to correct the frequency error in the second mode. An alternative gravity correction can be developed for all modes of the end mass. Since the end mass is the cause of the errors in the second natural frequency, it should improve the accuracy of the model.

The gravitational potential energy of the end mass due to the vertical displacement is given by equation 5.57.

$$\Pi = m_a g h_l \cos \theta \quad (5.57)$$

The vertical displacement at $x = l$ can be computed from the arc length integral.

$$h_l = \int_0^l \sqrt{1 + (v')^2} dx - x \quad (5.58)$$

If v' is small, equation 5.58 can be simplified to the following equation by use of a

binomial series.

$$h_l \approx \int_0^l \left(1 + \frac{(v')^2}{2} \right) dx - x = \int_0^l \frac{(v')^2}{2} dx \quad (5.59)$$

This potential energy expression is used to replace the previously used term for the end mass, equation 5.29. Substitution of equations 5.59 and 5.31 into equation 5.57 obtains the potential energy expression as a function of the deformation coordinates of the assumed mode shapes. With this replacement, the stiffness matrix is revised to the following form.

$$\bar{K} = \begin{bmatrix} K_t + \int_0^l \rho Agx dx + m_agl & \int_0^l \rho Ag \bar{\Psi}^T dx + m_ag \bar{\Psi}_l^T \\ \int_0^l \rho Ag \bar{\Psi} dx + m_ag \bar{\Psi}_l & \int_0^l EI \bar{\Upsilon} dx - \int_0^l \frac{\rho Ag}{x} \bar{\Gamma} dx + m_ag \int_0^l \bar{\Omega} dx \end{bmatrix} \quad (5.60)$$

Figures 5.19 and 5.20 compare the second natural frequencies of the two coupled cantilever-mass loaded models. The old model uses equation 5.29 to account for the vertical displacement of the end mass, while the new model uses equation 5.59. The new model agrees with the experimental data better than the old model, especially for large mass ratios.

The first natural frequencies of the old and new models are compared in Figures 5.21 and 5.22. The new model is marginally better than the old model for a mass ratio of 0.25, but is inferior to the old model for a mass ratio of 1.0. Since this new gravity correction term does not improve the assumed modes model for both modes, it is not used outside of this section.

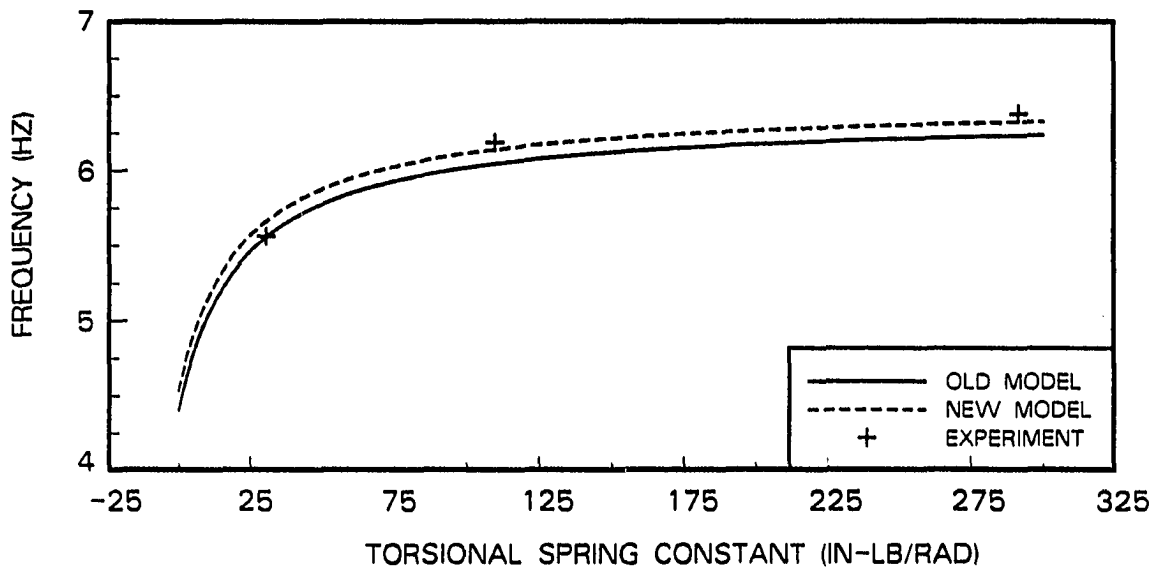


Figure 5.19: Second natural frequency of coupled cantilever-mass loaded model; comparison of gravity correction; case 1; $(m_a/m) = 0.25$

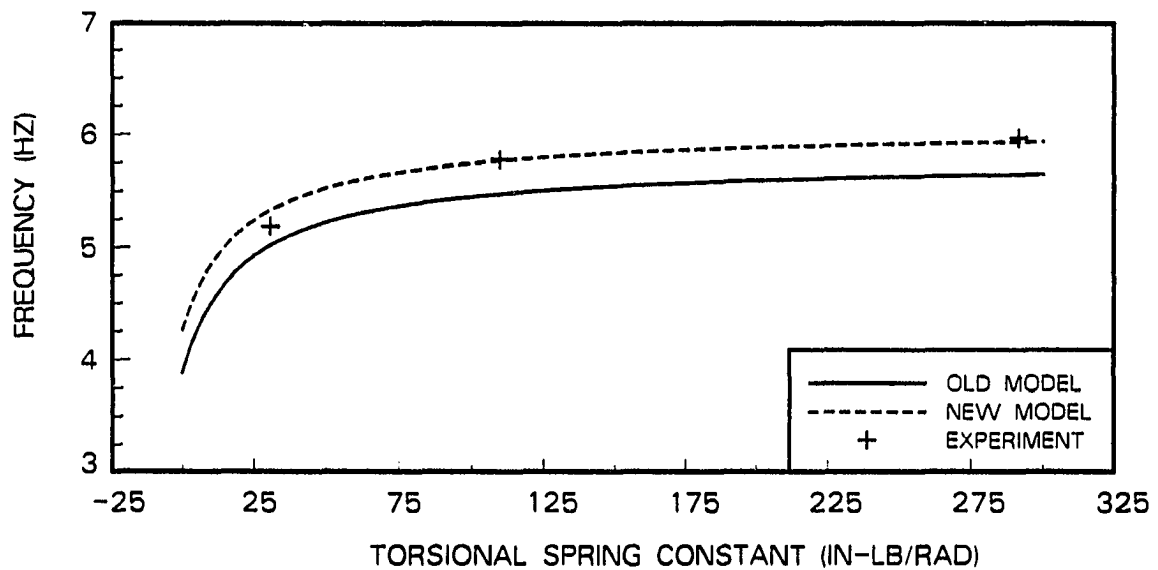


Figure 5.20: Second natural frequency of coupled cantilever-mass loaded model; comparison of gravity correction; case 1; $(m_a/m) = 1.0$

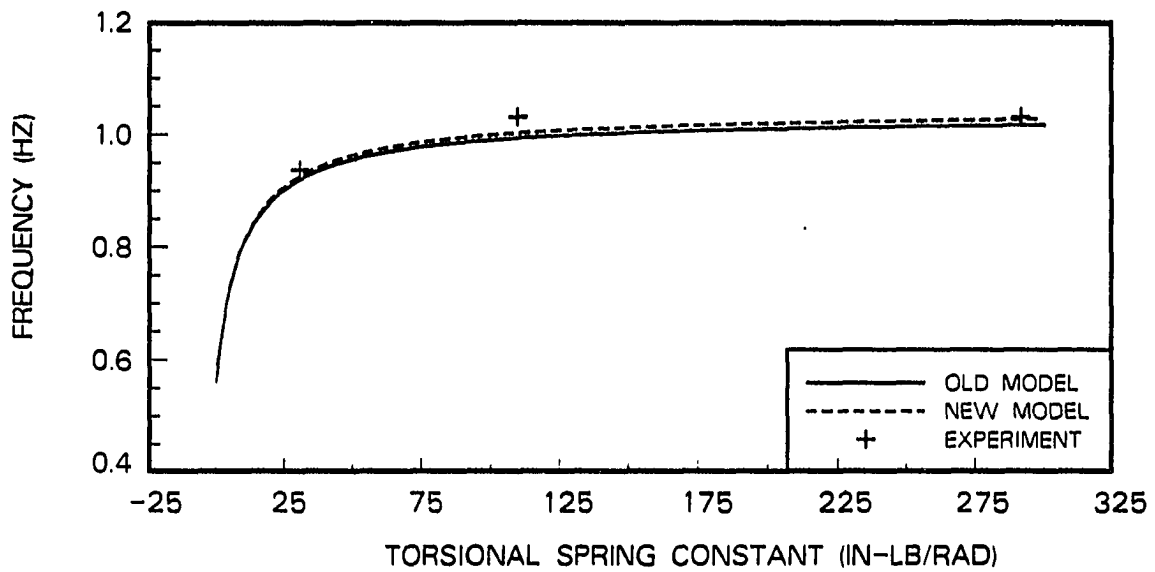


Figure 5.21: First natural frequency of coupled cantilever-mass loaded model; comparison of gravity correction; case 1; $(m_a/m) = 0.25$

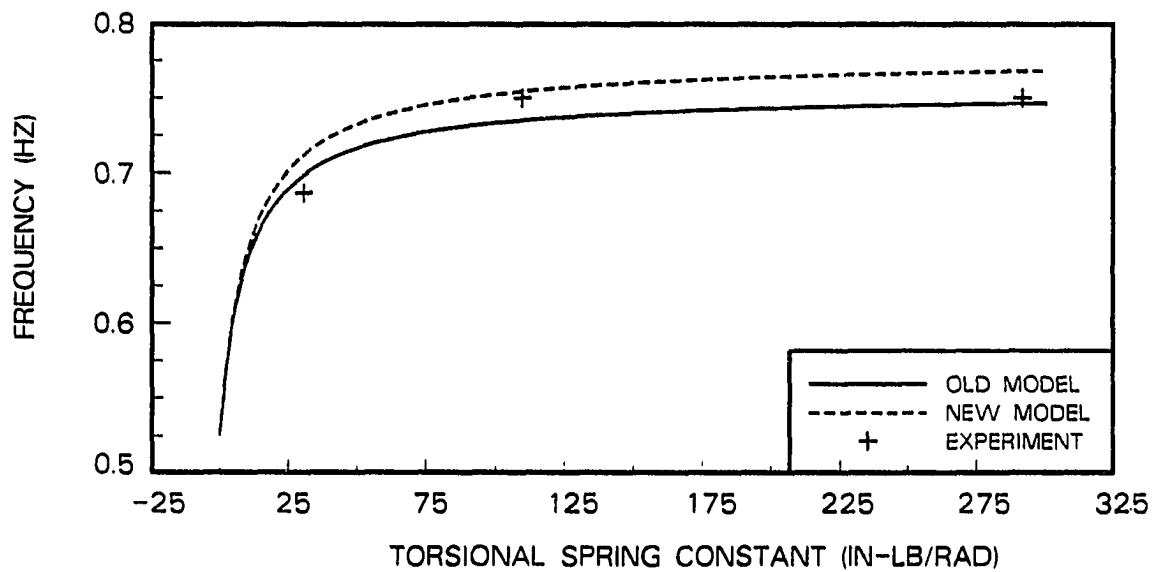


Figure 5.22: First natural frequency of coupled cantilever-mass loaded model; comparison of gravity correction; case 1; $(m_a/m) = 1.0$

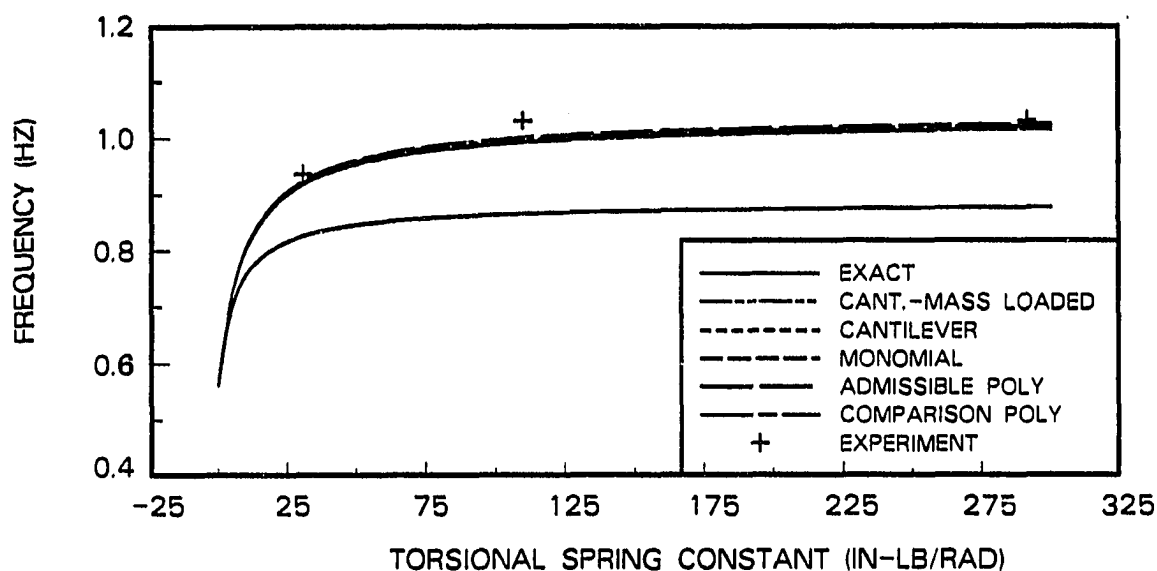


Figure 5.23: Comparison of first natural frequencies from alternative assumed mode shapes; vertical orientation; case 1; $(m_a/m) = 0.25$

5.6.1 Effect of Gravity on Mode Shape Selection

The addition of gravity makes the selection of the assumed mode shapes more critical. Figures 5.23 and 5.24 compare the first natural frequency of the assumed mode models for end mass ratios of 0.25 and 1.0, respectively. In the absence of gravity, all of the assumed mode shapes were equally accurate for either mass ratio. Figure 5.23 shows that assumed mode selection is still not critical for a mass ratio of 0.25. There are differences between the models, but these differences are negligible. When the mass ratio is increased to 1.0, the differences between the models become significant. The cantilever-mass loaded, cantilever, and comparison polynomial models agree with the experimental data, while the admissible polynomial and monomial models are significantly in error.

The linear combinations of the assumed mode shapes do not explain these

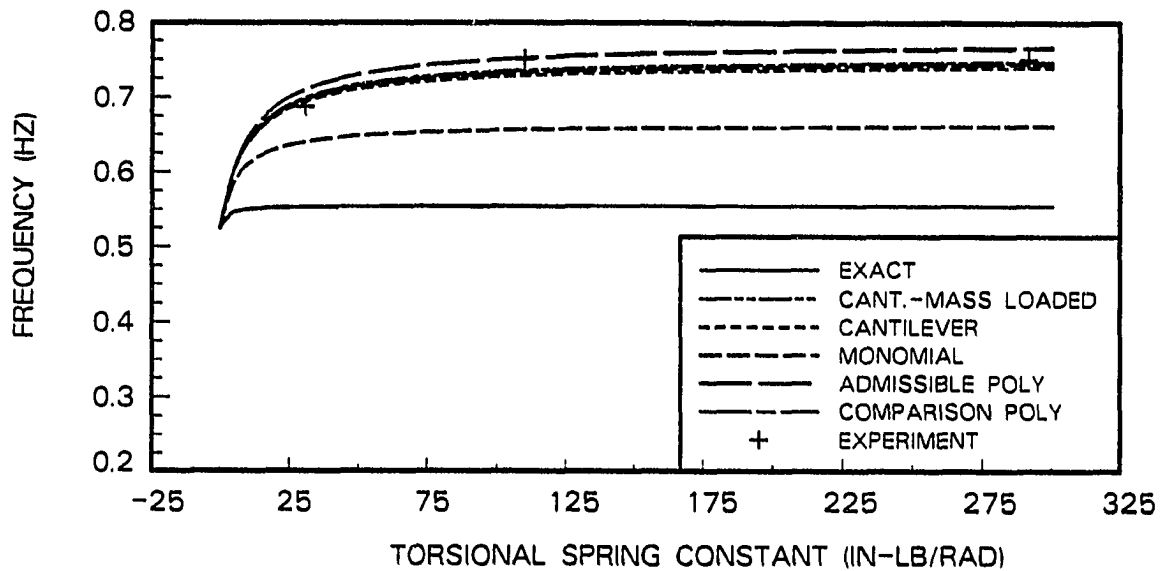


Figure 5.24: Comparison of first natural frequencies from alternative assumed mode shapes; vertical orientation; case 1; $(m_a/m) = 1.0$

frequency plots well. The first mode coupled mode shape plots for the two mass ratios are shown in Figures 5.25 and 5.26. The discrepancy between the coupled mode shapes of the monomial model and those of the other models indicates that the frequencies of the monomial model should be significantly different from the other models. The frequencies of the monomial model are different for a mass ratio of 1.0, but are virtually identical to the other models for a mass ratio of 0.25. The similarity between the exact mode shapes and the coupled mode shapes of the assumed modes models implies that they should have similar natural frequencies. However, Figures 5.23 and 5.24 show large frequency errors for the exact model. These errors are due to the absence of a gravity correction term in the exact model.

Figures 5.27 and 5.28 compare the second natural frequencies for the alternative

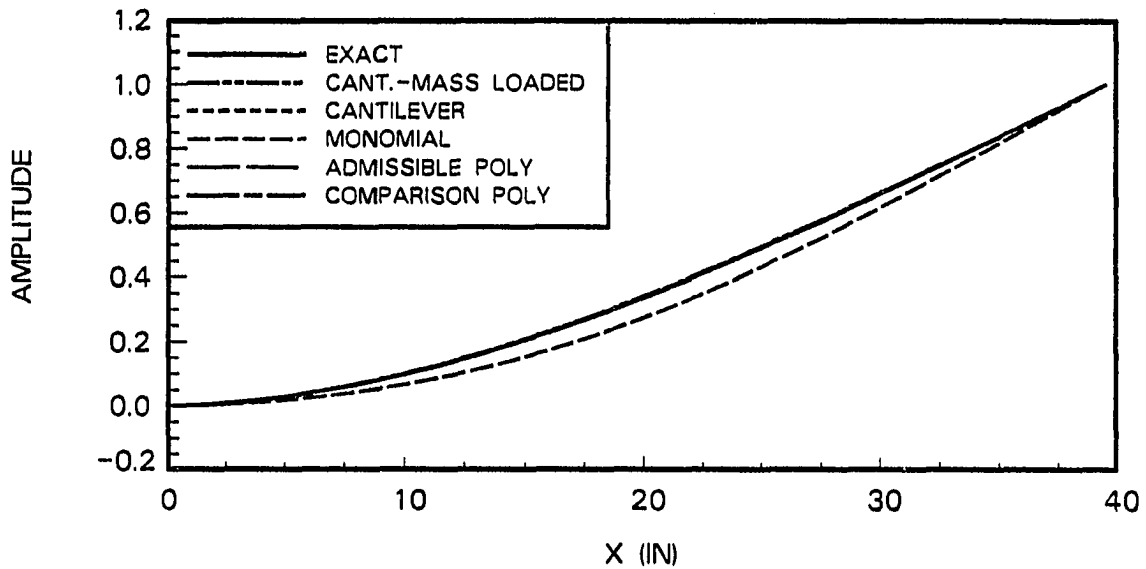


Figure 5.25: Comparison of linear combinations of assumed mode shapes to first exact mode shape; $K_t = 200 \text{ in-lb-rad}^{-1}$; vertical orientation; case 1; $(m_a/m) = 0.25$

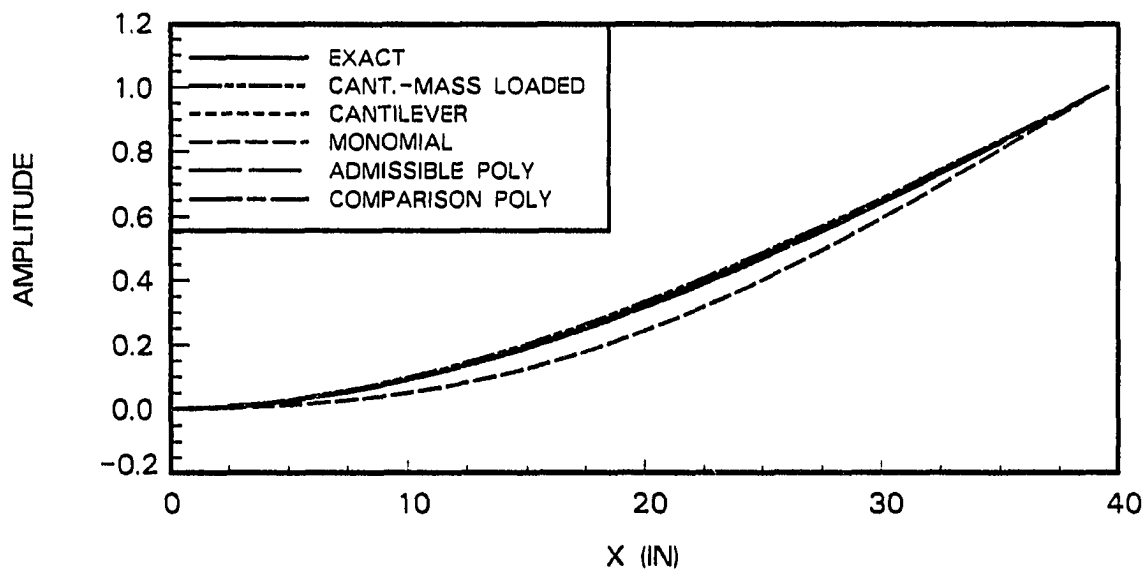


Figure 5.26: Comparison of linear combinations of assumed mode shapes to first exact mode shape; $K_t = 200 \text{ in-lb-rad}^{-1}$; vertical orientation; case 1; $(m_a/m) = 1.0$

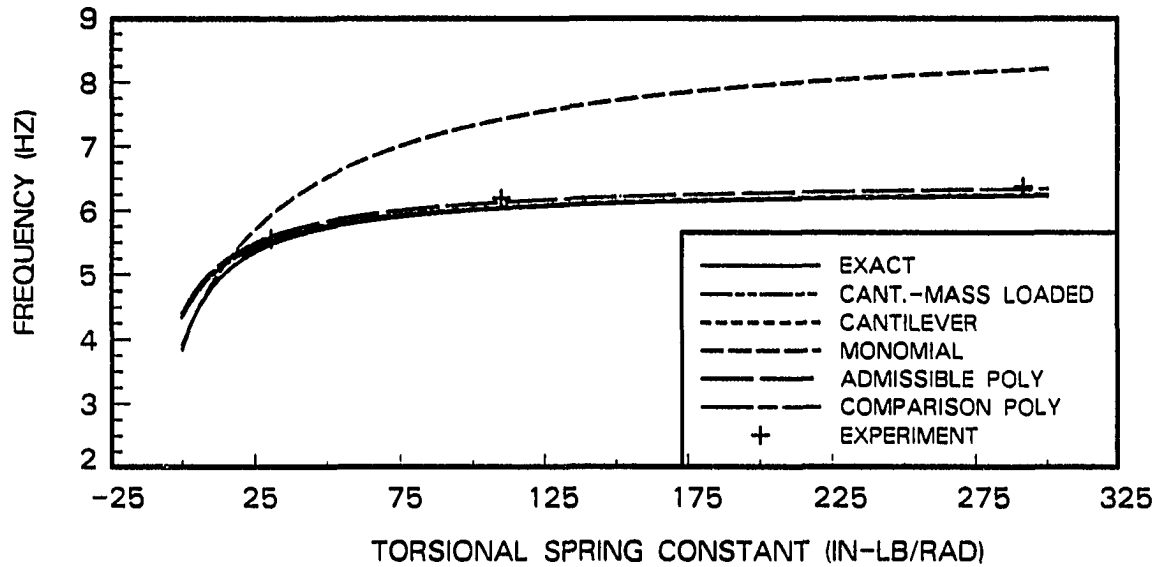


Figure 5.27: Comparison of second natural frequencies from alternative assumed mode shapes; vertical orientation; case 1; $(m_a/m) = 0.25$

coupled models. These plots are similar to the no gravity plots, Figures 5.7 and 5.8, except for the inaccuracy of the monomial model. A similar inaccuracy in the monomial model was observed in Chapter 4, for the arm without end mass. Beside the monomial model, all of the other models correlate with the experimental frequencies. However, it is difficult to conclude which one of the models is the most accurate, since the vertical displacement effect was not incorporated into the second mode of the model.

The linear combinations of the assumed mode shapes explain the poor performance of the monomial model. Figures 5.29 and 5.30 show the coupled system mode shapes for the monomial model differ significantly from the those of the other models. This difference is reflected in the large errors observed for the monomial model in the frequency plots.

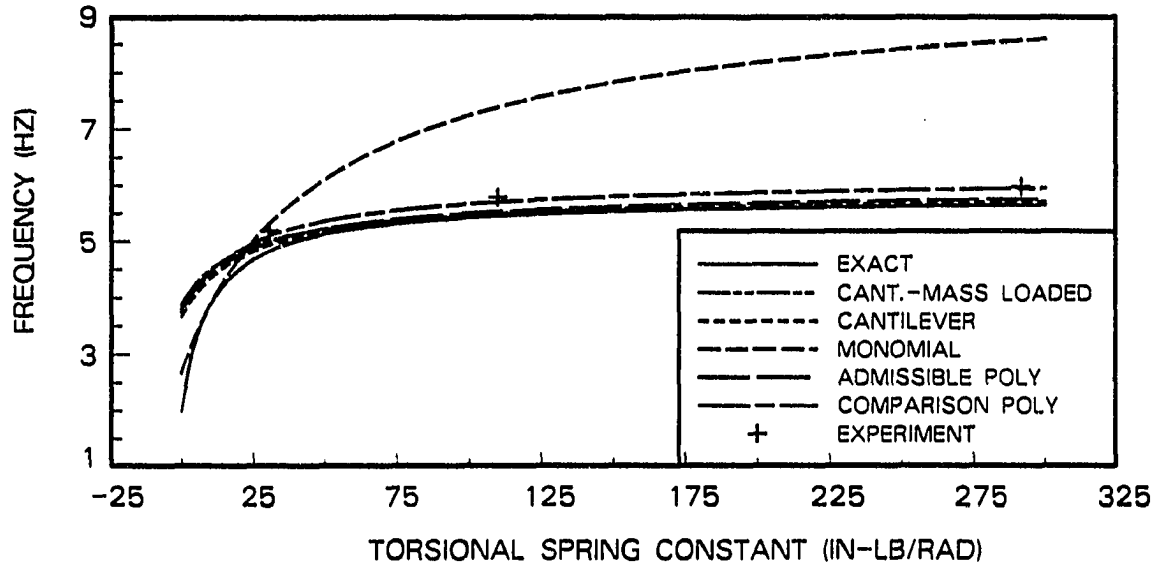


Figure 5.28: Comparison of second natural frequencies from alternative assumed mode shapes; vertical orientation; case 1; $(m_a/m) = 1.0$

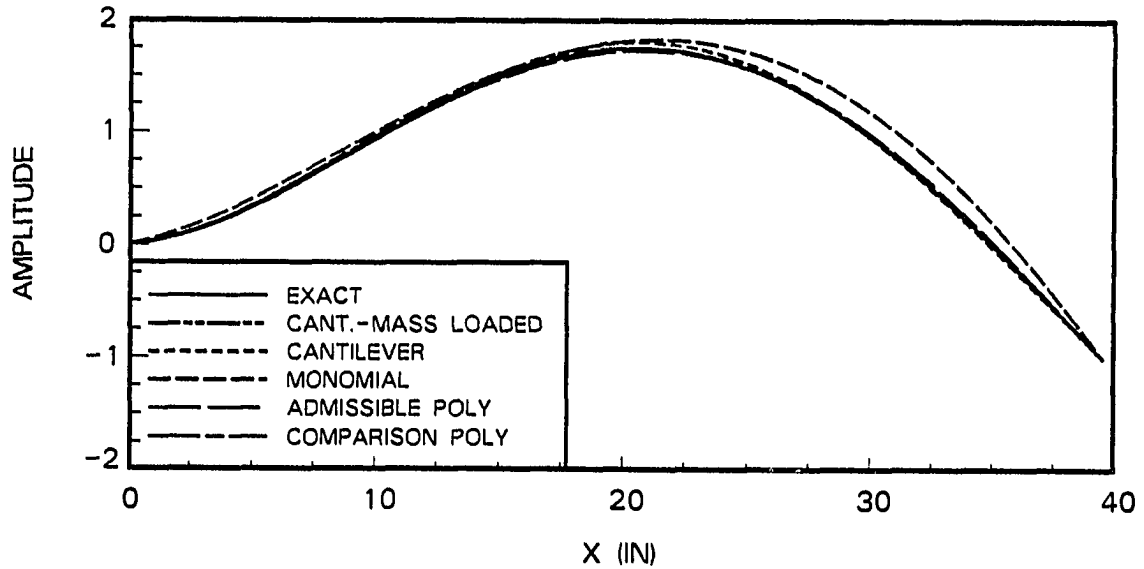


Figure 5.29: Comparison of linear combinations of assumed mode shapes to second exact mode shape; $K_t = 200 \text{ in-lb-rad}^{-1}$; vertical orientation; case 1; $(m_a/m) = 0.25$

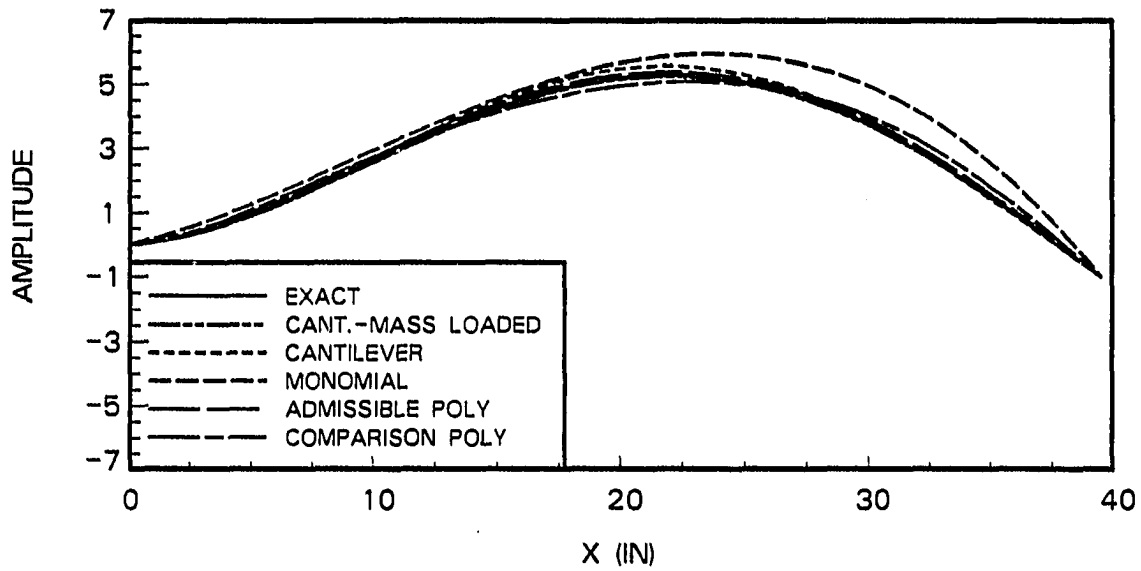


Figure 5.30: Comparison of linear combinations of assumed mode shapes to second exact mode shape; $K_t = 200 \text{ in-lb-rad}^{-1}$; vertical orientation; case 1; $(m_a/m) = 1.0$

5.7 Conclusions

Several conclusions concerning end mass may be drawn from this chapter. First, the selection of assumed mode shapes is not important for the first mode in the absence of gravity. All of the alternative mode shapes were equally accurate for the first mode. The accuracy of the second natural frequency is more sensitive to mode shape selection. The cantilever-mass loaded and cantilever models are the most accurate. However, the monomial model is as accurate and offers significant computational savings over the cantilever-mass loaded and cantilever mode shapes.

The selection of mode shapes is complicated by gravity. The monomial model is accurate in the presence of gravity for the first mode, but only for low mass ratios. The comparison polynomials are the best polynomial mode shapes. They

provide good frequency estimates in the presence of gravity, for both mass ratios. However, the cantilever-mass loaded and cantilever models are the best mode shapes for modeling the elastic arm with end mass. They provide accurate frequency predictions for all modes regardless of the end mass or gravity.

Second, a simple but effective plot has been developed to show the effect of elastic coupling upon the first natural frequency of robot arms with end mass. The frequency shift graph presented in Chapter 4 was extended to include the effect of an end mass. The magnitude of the frequency shifts is a function of both the frequency and mass ratios of the robot arm.

Three, gravity can significantly affect the natural frequencies of an elastic robot arm with end mass. The effect of gravity is magnified by the end mass, and affects both the first and second modes of the system. The first mode of the assumed modes model is accurate since it includes the gravity correction term developed in Chapter 4. The frequency error in the second mode can be corrected by a gravity correction term that is applied only to the end mass, but which is valid for all modes of the arm.

6 CONCLUSIONS

The purpose of this thesis was to develop guidelines for modeling of an single planar elastic robot arm. The following topics were addressed; selection of assumed mode shapes, coupling of elastic and rigid motions, gravity, and the effect of an end mass.

Based on a model using one rigid degree of freedom and three assumed mode shapes, the most accurate natural frequencies for the first two modes were obtained using the cantilever mode shapes for the elastic arm without end mass, and the cantilever-mass loaded mode shapes for the arm with end mass. A disadvantage of these mode shapes is that the modal integrals in the equations of motion cannot be evaluated analytically. Therefore, computationally intensive numerical integration is required to formulate the equations of motion.

Polynomial mode shapes offer a significant computational savings over the cantilever and cantilever-mass loaded mode shapes, since their modal integrals can be evaluated analytically. However, careful selection of the polynomials is necessary to obtain accurate models of the elastic arm. This selection is affected by gravity and the end mass. For the arm without end mass, the comparison polynomials are the best polynomial assumed mode shapes. They are as accurate as the cantilever mode shapes, both with and without gravity. For the elastic arm with end

mass, the selection of the polynomial assumed mode shapes is more critical. In the absence of gravity, the monomials are the best polynomial assumed mode shapes. With gravity, the comparison polynomials are the best polynomial assumed mode shapes.

A simple but effective graph has been developed to show the effect of elastic coupling upon the first natural frequency of a robot arm. Elasticity in robot arms can cause significant frequency shifts from a rigid model. These frequency shifts are due to the coupling between the elastic and gross motions and give an indication of the relative magnitudes of the two motions. The magnitude of these frequency shifts has been presented graphically, as a function of two easily calculated ratios: the ratio of the rigid frequency of the arm to the first cantilever frequency of the arm and the ratio of the end mass to the arm mass.

Gravity can significantly affect the first and second natural frequencies of the elastic arm. For an arm without end mass, only the first frequency is significantly affected by gravity. Addition of an end mass magnifies the effect of gravity, so that both the first and second natural frequencies are affected. To account for the gravity effect, the vertical displacement due to transverse deflections must be modeled.

A simple model based upon the first assumed mode shape was developed to allow prediction of the error caused by neglect of the vertical displacement due to transverse deflections. This simple model, incorporated into the coupled model as a gravity correction term, greatly reduced the error in the first natural frequency due to gravity. For an arm with end mass, the gravity correction term was extended to the higher modes of the arm to eliminate the error in the second natural frequency due to neglect of the vertical displacement.

7 BIBLIOGRAPHY

- [1] A. G. Erdman and G. N. Sandor. "Kineto-Elastodynamics, A Review of the State of the Art and Trends". *Mech. and Mach. Theory*, 7 (1972): 19-33.
- [2] G. G. Lowen and W. G. Jandrasits. "Survey of Investigations into the Dynamic Behavior of Mechanisms Containing Links with Distributed Mass and Elasticity". *Mech. and Mach. Theory*, 7 (1972): 3-17.
- [3] G. G. Lowen and C. Chassapis. "The Elastic Behavior of Linkages: An Update". *Mech. and Mach. Theory*, 21, No. 1 (1986): 33-42.
- [4] B. S. Thompson and C. K. Sung. "A Survey of Finite Element Techniques for Mechanism Design". *Mech. and Mach. Theory*, 21, No. 4 (1986): 351-359.
- [5] D. A. Turcic and A. Midha. "Dynamic Analysis of Elastic Mechanism Systems. Part I: Applications". *J. of Dynamic Syst., Measurement, and Control*, 106 (December, 1984): 249-254.
- [6] D. A. Turcic and A. Midha. "Generalized Equations of Motion for the Dynamic Analysis of Elastic Mechanism Systems". *J. of Dynamic Syst., Measurement, and Control*, 106 (December, 1984): 243-248.
- [7] W. L. Cleghorn, R. G. Fenton, and B. Tabarrok. "Finite Element Analysis of High-Speed Flexible Mechanisms". *Mech. and Mach. Theory*, 16, No. 4 (1981): 407-424.
- [8] J. O. Song and E. J. Haug. "Dynamic Analysis of Planar Flexible Mechanisms". *Com. Meth. in App. Mech. and Eng.*, 24 (1980): 359-381.
- [9] A. A. Shabana and R. A. Wehage. "Dynamic Analysis of Large-Scale Inertia-Variant Flexible Systems". U. of Iowa Center for Computer Aided Design, Iowa City, Iowa, Technical Report 82-7, 1982.
- [10] A. A. Shabana and R. A. Wehage. "A Coordinate Reduction Technique for Dynamic Analysis of Spatial Substructures with Large Angular Rotations". *J. of Struct. Mech.*, 11, No. 3 (1983): 401-431.

- [11] G. N. Sandor and X. Zhuang. "A Linearized Lumped Parameter Approach to Vibration and Stress Analysis of Elastic Linkages". *Mech. and Mach. Theory*, 20, No. 5 (1985): 427-436.
- [12] B. S. Thompson, D. Zuccaro, D. Gamache, and M. V. Gandhi. "An Experimental and Analytical Study of a Four-Bar Mechanism with Links Fabricated from a Fiber-Reinforced Composite Material". *Mech. and Mach. Theory*, 18, No. 2 (1983): 165-171.
- [13] B. S. Thompson and C. K. Sung. "A Variational Formulation for the Nonlinear Finite Element Analysis of Flexible Linkages: Theory, Implementation, and Experimental Results". *J. of Mech., Trans., and Auto. in Design*, 106 (December, 1984): 482-488.
- [14] B. S. Thompson and C. K. Sung. "An Analytical and Experimental Investigation of High-Speed Mechanisms Fabricated with Composite Laminates". *J. of Sound and Vibration*, 111, No. 3 (1986): 399-428.
- [15] W. H. Sunada and S. Dubowsky. "On the Dynamic Analysis and Behavior of Industrial Robotic Manipulators with Elastic Members". ASME Paper 82-DET-45, 1982.
- [16] M. Géradin, G. Robert, and C. Bernardin. "Dynamic Modeling of Manipulators with Flexible Members". In *Advanced Software in Robotics*, pp. 27-39. Edited by A. Danthine and M. Géradin. Elsevier Science Publishers, Holland, 1984.
- [17] B. V. Viscomi and R. S. Ayre. "Nonlinear Dynamic Response of Elastic Slider-Crank Mechanism". *J. of Eng. for Industry*, 93B (February, 1971): 251-262.
- [18] S. C. Chu and K. C. Pan. "Dynamic Response of a High-Speed Slider-Crank Mechanism with an Elastic Connecting Rod". *J. of Eng. for Industry*, 97, No. 1-2 (May, 1975): 542-550.
- [19] P. W. Jasinski, H. C. Lee, and G. N. Sandor. "Vibrations of Elastic Connecting Rod of a High-Speed Slider-Crank Mechanism". *J. of Eng. for Industry*, 93, No. 2 (May, 1971): 636-644.
- [20] G. H. Sutherland. "Analytical and Experimental Investigation of a High-Speed Elastic-Membered Linkage". *J. of Eng. for Industry*, 98B, No. 3 (August, 1976): 788-794.
- [21] W. G. Jandrasits and G. G. Lowen. "The Elastic-Dynamic Behavior of a Counterweighted Rocker Link with an Overhanging Endmass in a Four-Bar Linkage Part I: Theory". *J. of Mech. Design*, 101 (January, 1979): 77-88.

- [22] A. Garcia-Reynoso and W. P. Seering. "Vibration Characteristics of an Elastic Linkage with Elastic Input and Output Shafts". *J. of Mech., Trans., and Auto. in Design*, 106 (September, 1984): 272-277.
- [23] D. Kohli, D. Hunter, and G. N. Sandor. "Elastodynamic Analysis of a Completely Elastic System". *J. of Eng. for Industry*, 99B, No. 3 (August, 1977): 604-609.
- [24] M. Badlani and W. Kleinhenz. "Dynamic Stability of Elastic Mechanisms". *J. of Mech. Design*, 101 (January, 1979): 149-153.
- [25] M. Badlani and A. Midha. "Effect of Internal Material Damping on the Dynamics of a Slider-Crank Mechanism". *J. of Mech., Trans., and Auto. in Design*, 105 (September, 1983): 452-459.
- [26] T. J. Wielenga. "Simplifications in the Simulation of Mechanisms Containing Flexible Members". Ph.D. dissertation, U. of Michigan, Ann Arbor, Michigan, 1984.
- [27] R. R. Ryan. "Flexibility Modeling Methods in Multibody Dynamics". Ph.D. dissertation, Stanford University, Palo Alto, California, 1986.
- [28] R. C. Winfrey. "Elastic Link Mechanism Dynamics". *J. of Eng. for Industry*, 93B (February, 1971): 268-272.
- [29] I. Iman, G. N. Sandor, and S. N. Kramer. "Deflection and Stress Analysis in High Speed Planar Mechanisms with Elastic Links". *J. of Eng. for Industry*, 95, No. 2 (May, 1973): 541-548.
- [30] A. Midha, A. G. Erdman, and D. A. Frohrib. "A Closed-Form Numerical Algorithm for the Periodic Response of High-Speed Elastic Linkages". *J. of Mech. Design*, 101 (January, 1979): 154-162.
- [31] W. S. Yoo. "Dynamics of Flexible Mechanical Systems Using Finite Element Lumped Mass Approximation and Static Correction Modes". Ph.D. dissertation, U. of Iowa, Iowa City, Iowa, 1985.
- [32] A. A. Shabana. "Automated Analysis of Constrained Systems of Rigid and Flexible Bodies". ASME Paper 85-DET-29, 1985.
- [33] B. S. Thompson, D. Zuccaro, D. Gamache, and M. V. Gandhi. "An Experimental and Analytical Study of the Dynamic Response of a Linkage Fabricated from a Unidirectional Fiber-Reinforced Composite Laminate". *J. of Mech., Trans., and Auto. in Design*, 106 (September, 1983): 526-533.
- [34] R. M. Alexander and K. M. Lawrence. "An Experimental Investigation of the Dynamic Response of an Elastic Mechanism". *J. of Eng. for Industry*, 96, No. 1 (February, 1974): 268-274.

- [35] J. P. Sadler and G. N. Sandor. "A Lumped Parameter Approach to Vibration and Stress Analysis of Elastic Linkages". *J. of Eng. for Industry*, 95, No. 2 (May, 1973): 549-557.
- [36] T. Furuhashi, M. Saito, and N. Morita. "Vibration Analysis of Four-bar Linkage with Elastic Links". *Bulletin of the JSME*, 22, No. 174 (December, 1979): 1826-1833.
- [37] R. M. Alexander and K. L. Lawrence. "Experimentally Determined Dynamic Strains in an Elastic Mechanism". *J. of Eng. for Industry*, 97B, No. 3 (August, 1975): 791-794.
- [38] W. L. Cleghorn, R. G. Fenton, and B. Tabarrok. "Steady-State Vibrational Response of High-Speed Flexible Mechanisms". *Mech. and Mach. Theory*, 19, No. 4/5 (1984): 417-423.
- [39] D. A. Turcic, A. Midha, and J. R. Bosnik. "Dynamic Analysis of Elastic Mechanism Systems. Part II: Experimental Results". *J. of Dynamic Syst., Measurement, and Control*, 106 (December, 1984): 255-260.
- [40] W. G. Jandrasits and G. G. Lowen. "The Elastic-Dynamic Behavior of a Counterweighted Rocker Link with an Overhanging Endmass in a Four-Bar Linkage, Part II: Application and Experiment". *J. of Mech. Design*, 101 (January, 1979): 89-98.
- [41] C. K. Sung, B. S. Thompson, T. M. Xing, and C. H. Wang. "An Experimental Study on the Nonlinear Elastodynamic Response of Linkage Mechanisms". *Mech. and Mach. Theory*, 21, No. 2 (1986): 121-133.
- [42] D. X. Liao, C. K. Sung, B. S. Thompson, and K. Soong. "A Note on the Quasi-Static Responses, Dynamic Responses, and the Super-Harmonic Resonances of Flexible Linkages: Some Experimental Results". ASME Paper 86-DET-146, 1986.
- [43] A. Yigit, R. A. Scott, and A. Galip Ulsoy. "Flexural Motion of a Radially Rotating Beam Attached to a Rigid Body". *J. of Sound and Vibration*, 121, No. 2 (1988): 201-210.
- [44] S. V. Hoa. "Vibration of a Rotating Beam with Tip Mass". *J. of Sound and Vibration*, 67, No. 3 (1979): 369-381.
- [45] J. C. Simo and L. Vu-Quoc. "The Role of Non-Linear Theories in Transient Dynamic Analysis of Flexible Structures". *J. of Sound and Vibration*, 119, No. 3 (1987): 487-508.

- [46] R. H. Cannon, Jr. and E. Schmitz. "Initial Experiments on the End-Point Control of a Flexible One-Link Robot". *Int. J. of Robotics Research*, 3, No. 3 (1984): 62-75.
- [47] D. M. Rovner and R. H. Cannon, Jr. "Experiments Toward On-Line Identification and Control of a Very Flexible One-Link Manipulator". *Int. J. of Robotics Research*, 6, No. 4 (1987): 3-19.
- [48] Y. Sakawa, F. Matsuno, and S. Fukushima. "Modeling and Feedback Control of a Flexible Arm". *J. of Robotic Systems*, 2, No. 4 (1985): 453-472.
- [49] P. T. Kotnik, S. Yurkovich, and Ü. Özgüner. "Acceleration Feedback for Control of a Flexible Manipulator Arm". *J. of Robotic Systems*, 5, No. 3 (1988): 181-196.
- [50] W. J. Book, O. Maizza-Neto, and D. E. Whitney. "Feedback Control of Two Beam, Two Joint systems with Distributed Flexibility". *J. of Dynamic Syst., Measurement, and Control*, 97, No. 4 (December, 1975): 424-431.
- [51] J. N. Reddy. *Energy and Variational Methods in Applied Mechanics*. John Wiley and Sons, New York, 1984.
- [52] L. Meirovitch. *Analytical Methods in Vibrations*. Macmillan Co., New York, 1967.
- [53] K. G. McConnell, Engineering Science and Mechanics Department, Iowa State University, Personal communication, 1988.

8 APPENDIX A. EXPERIMENTAL PROCEDURE

The experimental apparatus and the basic experimental procedure are described in Chapter 4. This appendix describes the experimental procedures in greater detail.

8.1 Measurement of Torsional Spring Constant

As discussed in Section 4.1, the torsional spring constant is determined by applying a known torque to the shaft and measuring its resulting rotation. The torque is applied by attaching weights to the end of an arm clamped to the shaft. The rotation of the shaft is not measured directly, but is calculated from the vertical displacement of the end of the arm.

As shown in Figure 8.1, the arm is modeled as rigid beam of mass, m , and length, c . Assume the arm is horizontal when no weights are attached to it. A weight, W , is attached to the end of the arm, and the system allowed to reach equilibrium at an angular displacement, θ . The vertical displacement of the end of the beam, h , is then measured by the displacement transducer.

Sum moments about point O.

$$-K_t\theta + Wc \cos \theta + \frac{mgc}{2} \cos \theta = 0 \quad (8.1)$$

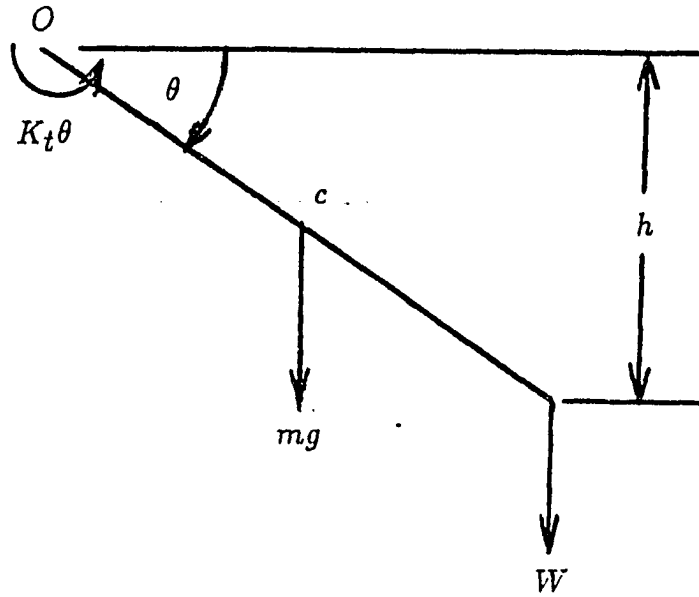


Figure 8.1: Free body diagram of arm

Since θ is small, the following approximations are made.

$$\cos \theta \approx 1 \quad (8.2)$$

$$\theta \approx \frac{h}{c} \quad (8.3)$$

With these approximations, equation 8.1 simplifies to equation 8.4

$$K_t = \frac{c^2 \left(W + \frac{mg}{2} \right)}{h} \quad (8.4)$$

The vertical displacement, h , is proportional to the output voltage of the LVDT;

$$h = S_d (V - V_o) \quad (8.5)$$

where S_d is the displacement sensitivity of the LVDT and V_o is its output voltage when $W = 0$. Eliminate h in equation 8.4 by using equation 8.5, and rearrange the resulting equation to the following form.

$$W = \left(\frac{K_t S_d}{c^2} \right) V - \left(\frac{K_t S_d V_o}{c^2} + \frac{mg}{2} \right) \quad (8.6)$$

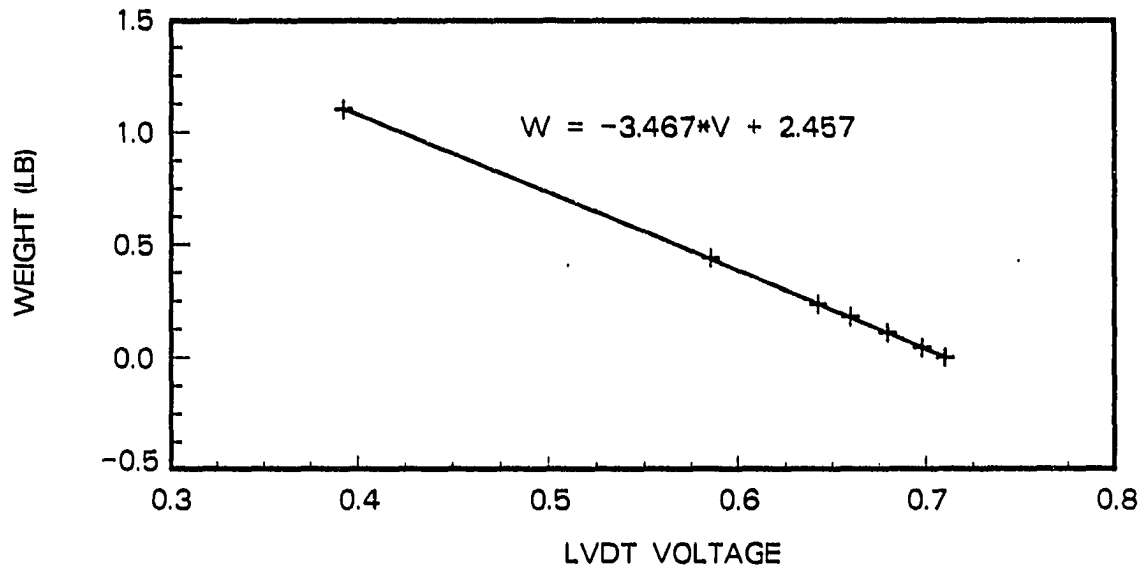


Figure 8.2: Calibration graph for K_t

A graph of the weight against the output voltage should be a straight line, from whose slope the torsional stiffness can be calculated.

In the experiment, a weight is attached to the arm and the resulting output voltage measured. This is repeated for a variety of weights. The weights are graphed against the voltages, and a line fitted to the data via the least squares method. Figure 8.2 shows a typical calibration graph. The torsional stiffness is calculated from the slope of the line, r .

$$K_t = \frac{rc^2}{S_d} = \frac{\left(-3.470 \frac{\text{in}}{\text{volt}}\right) (3.998 \text{ in})^2}{-0.1954 \frac{\text{in}}{\text{volt}}} = 283.9 \frac{\text{lb-in}}{\text{rad}} \quad (8.7)$$

8.2 Natural Frequency Measurement

The natural frequencies of the system are determined by a free vibration response method. As discussed in Section 4.1, the arm is struck or plucked. The

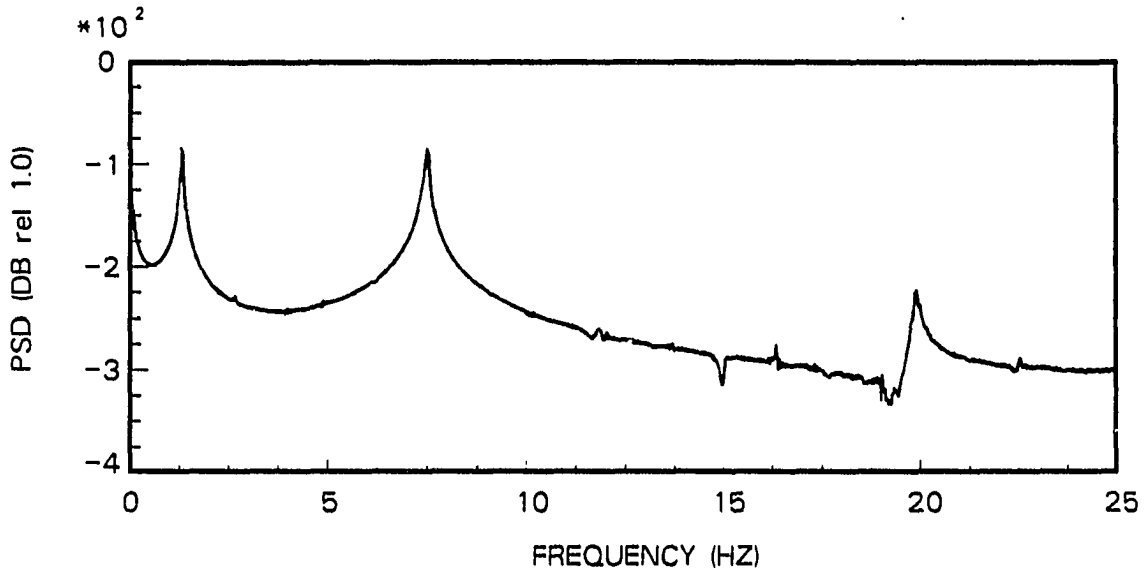


Figure 8.3: Typical displacement autospectrum

rotational displacement of the mounting shaft or the transverse acceleration of a point on the arm is measured as the system response. A signal analyzer acquires the system response signal and computes its autospectrum. The natural frequencies of the system appear as peaks in the autospectrum. A typical displacement autospectrum for this experiment is shown in Figure 8.3. Two natural frequencies are apparent, 1.313 and 7.500 hertz. The peak at zero hertz is not a natural frequency, but is due to the DC offset of the LVDT.

A schematic of the instrumentation is shown in Figure 4.3. The following equipment and parameters were used in the experiment. The LVDT is a Hewlett-Packard 7DCDT-1000. The accelerometer (Endevco 2222C) has a very low mass to minimize mass loading effects on the light beam. Wax is used to attach the accelerometer to the beam. A Kistler Model 504 charge amplifier is used to condition the output of the accelerometer. The sensitivity of the charge amplifier is 20 (g/volt)

and its time constant is 200 seconds. A Bruel & Kjaer Model 2032 Signal Analyzer is used to acquire the system response and compute its autospectrum. The following parameters are used in operation of the signal analyzer.

1. Baseband operation, 0.03125 or 0.0625 hertz frequency resolution
2. Rectangular data window
3. DC coupled operation
4. Two spectral averages
5. Power spectral density display

9 APPENDIX B. COMPARISON POLYNOMIAL DEVELOPMENT

9.1 Elastic Arm Without End Mass

The derivation of the comparison functions in Section 4.2.1 results in two sets of linear algebraic equations in the unknown polynomial coefficients. These equations are presented here. Equation 9.1 is the set of equations for the second mode shape, while equations 9.2 through 9.5 are the equations for the third mode shape. They are written in terms of rational numbers since the mode shapes are highly sensitive to round-off error. By retaining the rational number form, the round-off error in computer calculation of the coefficients is minimized.

$$\begin{bmatrix} 6l & 12l^2 & 20l^3 \\ 6 & 24l & 60l^2 \\ \frac{279l}{3024} & \frac{177l^2}{2268} & \frac{219l^3}{3240} \end{bmatrix} \begin{bmatrix} d_2 \\ e_2 \\ f_2 \end{bmatrix} = \begin{bmatrix} -2 \\ 0 \\ \frac{-213}{1890} \end{bmatrix} \quad (9.1)$$

$$6d_3l + 12e_3l^2 + 20f_3l^3 + 30g_3l^4 = -2 \quad (9.2)$$

$$6d_3 + 24e_3l + 60f_3l^2 + 120g_3l^3 = 0 \quad (9.3)$$

$$\begin{aligned} d_3 \left[l \left(\frac{1}{6} - \frac{2}{21} + \frac{1}{48} \right) \right] + e_3 \left[l^2 \left(\frac{1}{7} - \frac{1}{12} + \frac{1}{54} \right) \right] + f_3 \left[l^3 \left(\frac{1}{8} - \frac{2}{27} + \frac{1}{60} \right) \right] \\ + g_3 \left[l^4 \left(\frac{1}{9} - \frac{1}{15} + \frac{1}{66} \right) \right] = \left(-\frac{1}{5} + \frac{1}{9} - \frac{1}{42} \right) \end{aligned} \quad (9.4)$$

$$\begin{aligned}
& d_3 \left[l \left(\frac{1}{6} - \frac{d_2 l}{7} + \frac{e_2 l^2}{8} + \frac{f_2 l^3}{9} \right) \right] + e_3 \left[l^2 \left(\frac{1}{7} - \frac{d_2 l}{8} + \frac{e_2 l^2}{9} + \frac{f_2 l^3}{10} \right) \right] \\
& + f_3 \left[l^3 \left(\frac{1}{8} - \frac{d_2 l}{9} + \frac{e_2 l^2}{10} + \frac{f_2 l^3}{11} \right) \right] + g_3 \left[l^4 \left(\frac{1}{9} - \frac{d_2 l}{10} + \frac{e_2 l^2}{11} + \frac{f_2 l^3}{12} \right) \right] \\
& = \left(-\frac{1}{5} + \frac{d_2 l}{6} - \frac{e_2 l^2}{7} - \frac{f_2 l^3}{8} \right) \quad (9.5)
\end{aligned}$$

9.2 Elastic Arm With End Mass

The derivation of the comparison functions in Section 5.4.1 results in three sets of linear algebraic equations in the unknown polynomial coefficients. These equations are presented here. Equation 9.6 is the set of equations for the first mode shape, equations 9.7 through 9.9 are the equations for the second mode shape, and equations 9.10 through 9.13 are the equations for the third mode shape.

$$\begin{bmatrix} 6 + \frac{m_a \omega_1^2 l^3}{EI} & 24l + \frac{m_a \omega_1^2 l^4}{EI} \\ 6l - \frac{3J_a \omega_1^2 l^2}{EI} & 12l^2 - \frac{4J_a \omega_1^2 l^3}{EI} \end{bmatrix} \begin{Bmatrix} d_1 \\ e_1 \end{Bmatrix} = \begin{Bmatrix} -\frac{m_a l^2 \omega_1^2}{EI} \\ 2 \left(\frac{J_a l \omega_1^2}{EI} - 1 \right) \end{Bmatrix} \quad (9.6)$$

$$\begin{aligned}
& \left[6 + \frac{m_a \omega_2^2 l^3}{EI} \right] d_2 + \left[24l + \frac{m_a \omega_2^2 l^4}{EI} \right] e_2 \\
& + \left[60l^2 + \frac{m_a \omega_2^2 l^5}{EI} \right] f_2 = -\frac{m_a \omega_2^2 l^2}{EI} \quad (9.7)
\end{aligned}$$

$$\begin{aligned}
& \left[6l - \frac{3J_a \omega_2^2 l^2}{EI} \right] d_2 + \left[12l^2 - \frac{4J_a \omega_2^2 l^3}{EI} \right] e_2 \\
& + \left[20l^3 - \frac{5J_a \omega_2^2 l^4}{EI} \right] f_2 = 2 \left(\frac{J_a \omega_2^2 l}{EI} - 1 \right) \quad (9.8)
\end{aligned}$$

$$(9.12) \quad \begin{aligned} & \left[l \left(\frac{6}{1} d_1 l + \frac{7}{e_1 l^2} + \frac{8}{e_1 l^2} \right) \right] p_3 + \left[l^2 \left(\frac{7}{1} + \frac{8}{d_1 l} + \frac{9}{e_1 l^2} \right) \right] e_3 \\ & + \left[l^3 \left(\frac{8}{1} - \frac{9}{d_1 l} + \frac{10}{e_1 l^2} \right) \right] f_3 + \left[l^4 \left(\frac{9}{1} - \frac{10}{d_1 l} + \frac{11}{e_1 l^2} \right) \right] g_3 \\ & = - \left(\frac{5}{1} + \frac{6}{d_1 l} + \frac{7}{e_1 l^2} \right) \end{aligned}$$

$$(9.11) \quad \begin{aligned} & \left[6l - \frac{3J\omega^2 l^2}{EI} \right] p_3 + \left[12l^2 - \frac{4J\omega^2 l^3}{EI} \right] e_3 \\ & + \left[20l^3 - \frac{5J\omega^2 l^4}{EI} \right] f_3 + \left[30l^4 - \frac{6J\omega^2 l^5}{EI} \right] g_3 \\ & = 2 \left(\frac{J\omega^2 l}{EI} - 1 \right) \end{aligned}$$

$$(9.10) \quad \begin{aligned} & \left[6 + \frac{m\omega^2 l^3}{EI} \right] p_3 + \left[24l + \frac{m\omega^2 l^4}{EI} \right] e_3 \\ & + \left[60l^2 + \frac{m\omega^2 l^5}{EI} \right] f_3 + \left[120l^3 + \frac{m\omega^2 l^6}{EI} \right] g_3 \\ & = - \frac{EI}{m\omega^2 l^2} \end{aligned}$$

$$(9.9) \quad \begin{aligned} & \left[l \left(\frac{6}{1} d_1 l + \frac{7}{e_1 l^2} + \frac{8}{e_1 l^2} \right) \right] p_2 + \left[l^2 \left(\frac{7}{1} + \frac{8}{d_1 l} + \frac{9}{e_1 l^2} \right) \right] e_2 \\ & + \left[l^3 \left(\frac{8}{1} - \frac{9}{d_1 l} + \frac{10}{e_1 l^2} \right) \right] f_2 = - \left(\frac{5}{1} + \frac{6}{d_1 l} + \frac{7}{e_1 l^2} \right) \end{aligned}$$

$$\begin{aligned}
& d_3 \left[l \left(\frac{1}{6} + \frac{d_2 l}{7} + \frac{e_2 l^2}{8} + \frac{f_2 l^3}{9} \right) \right] + e_3 \left[l^2 \left(\frac{1}{7} + \frac{d_2 l}{8} + \frac{e_2 l^2}{9} + \frac{f_2 l^3}{10} \right) \right] \\
& + f_3 \left[l^3 \left(\frac{1}{8} + \frac{d_2 l}{9} + \frac{e_2 l^2}{10} + \frac{f_2 l^3}{11} \right) \right] + g_3 \left[l^4 \left(\frac{1}{9} + \frac{d_2 l}{10} + \frac{e_2 l^2}{11} + \frac{f_2 l^3}{12} \right) \right] \\
& = - \left(\frac{1}{5} + \frac{d_2 l}{6} + \frac{e_2 l^2}{7} + \frac{f_2 l^3}{8} \right) \quad (9.13)
\end{aligned}$$

10 APPENDIX C. CANTILEVER MODE SHAPE DEVELOPMENT

10.1 Cantilever Beam

The normal modes of a cantilever beam are used as approximations to the eigenfunctions of the elastic arm without an end mass. The normal modes used as the assumed mode shapes are defined by the following equation:

$$\Psi_i(x) = \frac{\cos(\lambda_i l) + \cosh(\lambda_i l)}{\sin(\lambda_i l) - \sinh(\lambda_i l)} [\cos(\lambda_i x) - \cosh(\lambda_i x)] + \sin(\lambda_i x) - \sinh(\lambda_i x) \quad (10.1)$$

where $\lambda_i l$ is the i th eigenvalue of the cantilever beam.

$$\lambda_i l = \left\{ \begin{array}{l} 1.875104 \\ 4.694091 \\ 7.854757 \end{array} \right\} \quad (10.2)$$

10.2 Cantilever-Mass Loaded Beam

The normal modes of a cantilever-mass loaded beam are used as approximations to the eigenfunctions of the elastic arm with an end mass. The characteristic equation of the cantilever-mass loaded beam is given by equation 10.3;

$$\begin{aligned}
& \left[\beta [\tan(\lambda_i l) - \tanh(\lambda_i l)] + \eta (\lambda_i l)^2 [\tanh(\lambda_i l) + \tan(\lambda_i l)] \right] \\
& \quad - \beta \eta \left[(\lambda_i l)^3 \left(\frac{1}{\cos(\lambda_i l) \cosh(\lambda_i l)} - 1 \right) \right] \\
& \quad - \beta \eta \left[\frac{1}{(\lambda_i l)} \left(\frac{1}{\cos(\lambda_i l) \cosh(\lambda_i l)} + 1 \right) \right] = 0 \quad (10.3)
\end{aligned}$$

where

$$\beta = \frac{m a}{\rho A l} \quad (10.4)$$

$$\eta = \frac{J a}{\rho A l^3} \quad (10.5)$$

The mode shape is represented by equation 10.6.

$$Y_i(x) = C_1^i \sin(\lambda_i x) + C_2^i \cos(\lambda_i x) + C_3^i \sinh(\lambda_i x) + C_4^i \cosh(\lambda_i x) \quad (10.6)$$

The C_j^i coefficients are obtained by substituting the i th eigenvalue, λ_i , into the following equations and solving the resulting linearly dependent set of equations.

$$C_2^i + C_4^i = 0 \quad (10.7)$$

$$C_1^i + C_3^i = 0 \quad (10.8)$$

$$\begin{aligned}
& C_1^i [\beta (\lambda_i l) \sin(\lambda_i l) - \cos(\lambda_i l)] + C_2^i [\beta (\lambda_i l) \cos(\lambda_i l) + \sin(\lambda_i l)] \\
& \quad + C_3^i [\beta (\lambda_i l) \sinh(\lambda_i l) + \cosh(\lambda_i l)] \\
& \quad + C_4^i [\beta (\lambda_i l) \cosh(\lambda_i l) + \sinh(\lambda_i l)] = 0 \quad (10.9)
\end{aligned}$$

$$\begin{aligned}
& C_1^i [\eta (\lambda_i l)^3 \cos(\lambda_i l) + \sin(\lambda_i l)] + C_2^i [-\eta (\lambda_i l)^3 \sin(\lambda_i l) - \cos(\lambda_i l)] \\
& \quad + C_3^i [\eta (\lambda_i l)^3 \cosh(\lambda_i l) - \sinh(\lambda_i l)] \\
& \quad + C_4^i [\eta (\lambda_i l)^3 \sinh(\lambda_i l) - \cosh(\lambda_i l)] = 0 \quad (10.10)
\end{aligned}$$